

In Situ Determination of  
Relative Permeability and Capillary Pressure Curves  
Using Multiphase Flow Rates and Pressures of  
Wireline Formation Testers

by  
Koksal Cig

Submitted for the degree of Doctor of Philosophy in  
Petroleum Engineering

Heriot-Watt University  
Institute of Petroleum Engineering  
August 2016

The copyright in this thesis is owned by the author. Any quotation from the thesis or use of any of the information contained in it must acknowledge this thesis as the source of the quotation or information.

## ABSTRACT

Relative permeability and capillary pressure curves are crucial inputs for reservoir modeling and simulation. Measuring these quantities on core samples in a laboratory is a necessary, but lengthy process. Wireline Formation Tester (WFT) logging is routinely applied in field operations for reservoir evaluation purposes. Since a historical record of WFT data often exists for a field, we propose in our study to estimate multiphase flow properties in situ from the acquired WFT data in a relatively short period of time.

The WFT tool records, among other measurements, bottomhole pressures, water-cuts and flow rates by pumping out fluids from a hydrocarbon bearing formation during the cleanup process in order to reduce the contamination level near the wellbore. The contamination, which is water based mud (WBM) filtrate in this study, invades from the openhole during drilling and changes the saturation of hydrocarbon and water in an invaded zone near the wellbore.

The proposed methodology estimates multiphase flow properties occurring near the wellbore, such as relative permeability, capillary pressure, damage skin and mud-filtrate invasion by inversion of water-cut and bottomhole pressure recorded during the WFT cleanup. Although the mud-filtrate invasion and the WFT cleanup replicate, respectively, secondary processes of imbibition and drainage in the reservoir, our study is designed under the assumption that a single set of multiphase flow curves represents both imbibition and drainage processes. The study shows that the most important parameters are the curvatures of relative permeability and capillary pressure curves during the processes. Although they can be optimized, prior knowledge of saturation endpoints and depth of mud-filtrate invasion improves the results. Noise levels of WFT logging, and heterogeneities of reservoir properties should be integrated correctly in the study.

The methodology uses a detailed numerical model of the invasion and cleanup processes, and WFT tool geometry coupled with an optimizer for the inversion. The model investigates reservoir and fluid properties, and represents the events accurately occurring during drilling, logging, invasion and cleanup. The results from synthetic and field examples demonstrate that relative permeability and capillary pressure, mud-filtrate invasion, damage skin can be estimated successfully in the inversion process.

## **DEDICATION**

I dedicate this dissertation to my wife, Tip and my daughters, Buse and Alize for their love and support. I will be eternally grateful for their patience during the long days, nights and weekends that I devoted to my study.

## **ACKNOWLEDGMENT**

There are numerous people without whom this dissertation would not have been successful, and to whom I am greatly indebted. I would like to extend my sincere gratitude to my supervisor Dr. Eric Mackay for accepting me to the Institute of Petroleum Engineering and encouraging me to pursue my dream. I am extremely grateful to my co-supervisor Dr. Cosan Ayan for his knowledge, vision, continuous technical guidance and support. The study would not have been possible without him. Sincere thanks as well to my co-supervisor Dr. Morten Kristensen. His technical contributions with respect to topics from statistics to reservoir simulation were invaluable to the many meetings and discussions throughout the process. I am also immensely thankful to Dr. Yildiray Cinar and Dr. Asghar Shams for their valuable time to review and contribute to this research.

Finally, the study would not be possible without the financial and technical support of Schlumberger Oilfield Services. I would like to thank Salih Merghani for trusting in my commitment to achieve the study along with my busy working schedule. I am also grateful to Hany Banna for providing the sponsorship and permission for the research and to Tolga Demir for supporting the study and allowing me to attend technical conferences and meetings related to the topic.



# DECLARATION STATEMENT

## ACADEMIC REGISTRY Research Thesis Submission



Name:	Koksai Cig		
School/PGI:	Institute of Petroleum Engineering		
Version: <i>(i.e. First, Resubmission, Final)</i>	Final	Degree Sought (Award and Subject area)	Doctor of Philosophy in Petroleum Engineering

### Declaration

In accordance with the appropriate regulations I hereby submit my thesis and I declare that:

- 1) the thesis embodies the results of my own work and has been composed by myself
- 2) where appropriate, I have made acknowledgement of the work of others and have made reference to work carried out in collaboration with other persons
- 3) the thesis is the correct version of the thesis for submission and is the same version as any electronic versions submitted\*.
- 4) my thesis for the award referred to, deposited in the Heriot-Watt University Library, should be made available for loan or photocopying and be available via the Institutional Repository, subject to such conditions as the Librarian may require
- 5) I understand that as a student of the University I am required to abide by the Regulations of the University and to conform to its discipline.

\* Please note that it is the responsibility of the candidate to ensure that the correct version of the thesis is submitted.

Signature of Candidate:		Date:	11-August -2016
-------------------------	---	-------	-----------------

### Submission

Submitted By <i>(name in capitals)</i> :	
Signature of Individual Submitting:	
Date Submitted:	

### For Completion in the Student Service Centre (SSC)

Received in the SSC by <i>(name in capitals)</i> :			
Method of Submission <i>(Handed in to SSC; posted through internal/external mail):</i>			
E-thesis Submitted <i>(mandatory for final theses)</i>			
Signature:		Date:	

Please note this form should bound into the submitted thesis.

Updated February 2008, November 2008, February 2009, January 2011

# TABLE OF CONTENTS

ABSTRACT

DEDICATION

ACKNOWLEDGMENT

DECLARATION STATEMENT

TABLE OF CONTENTS.....	i
LIST OF FIGURES .....	v
LIST OF TABLES .....	xvii
LIST OF PUBLICATIONS .....	xx

CHAPTER 1. INTRODUCTION .....	1
1.1 Problem Statement.....	1
1.2 Objectives .....	2
1.3 Methodology .....	2
1.4 Literature Review.....	4
1.5 Outline of Chapters .....	9

CHAPTER 2. THEORY AND ASSUMPTIONS .....	10
2.1 Invasion Profile.....	10
2.2 Cleanup and Sampling .....	12
2.3 Two-Phase Immiscible Flow .....	14
2.4 Multisegment Well Model .....	16
2.5 Skin Factor .....	19
2.6 Permeability .....	22
2.6.1 Laboratory Measurements of Relative Permeability .....	22
2.6.1.1 Unsteady State Method .....	23
2.6.1.2 Steady State Method .....	24
2.6.2 Relative Permeability Models.....	25
2.6.2.1 Modified Brooks and Corey Model .....	25
2.6.2.2 LET Model.....	26

2.7 Capillary Pressure .....	27
2.7.1 Capillary Pressure Models .....	28
2.7.1.1 Modified Brooks and Corey Model .....	28
2.7.1.2 Thomeer Model.....	28
2.8 Hysteresis.....	29
2.8.1 Hysteresis of Relative permeability Curves.....	30
2.8.2 Hysteresis of Capillary Pressure Curves.....	32
2.9 Optimization .....	34
2.9.1 Gradient Based Optimization.....	34
2.9.1.1 Solving Non-Linear Least Squares Problems .....	36
2.9.2 Stochastic Based Optimization .....	37
 CHAPTER 3. WIRELINE FORMATION TESTER LOGGING .....	41
3.1 Inlet Types .....	42
3.2 Pressure Sensors.....	43
3.3 Pressure Measurement .....	45
3.4 Fluid Analyzer Measurement.....	46
3.5 Cleanup and Sampling .....	47
 CHAPTER 4. NUMERICAL MODEL .....	50
4.1 Gridding.....	53
4.1.1 Dual-Packer Modeling.....	53
4.1.2 3D Radial Probe Modeling .....	56
4.1.3 Single Probe Modeling .....	57
4.2 Time Stepping.....	58
4.3 Multisegment Well Model .....	60
4.4 Mud-Filtrate Invasion .....	64
4.5 Cleanup .....	67
4.6 Events and Properties Affecting Invasion and Cleanup .....	74
4.6.1 Dynamic and Static Filtrations .....	74
4.6.2 Viscosity .....	78
4.6.3 Permeability Anisotropy .....	81
4.6.4 Porosity .....	85
4.6.5 Damage Skin.....	86
4.6.6 Capillary Pressure .....	88
4.6.7 Hysteresis.....	97

<b>CHAPTER 5. WORKFLOW FOR GENERATION OF RELATIVE PERMEABILITIES AND CAPILLARY PRESSURES.....</b>	<b>99</b>
5.1 Analysis of Openhole Logs.....	101
5.2 Preparation of Simulation Dataset .....	103
5.3 Design of Optimization.....	104
5.4 Analysis of Optimization Runs.....	105
5.4.1 Analysis of Gradient Based Optimization .....	106
5.4.2 Analysis of Stochastic Based Optimization.....	107
5.5 Synthetic Examples.....	109
5.5.1 Stochastic Based Optimization Synthetic Example.....	110
5.5.1.1 Analysis of Single Parameter Trends.....	113
5.5.1.2 Analysis of Objective Function Values .....	117
5.6 Field Examples.....	121
5.7 Summary of Stochastic Based Optimization Examples.....	122
 <b>CHAPTER 6. CONCLUSIONS AND RECOMMENDATIONS FOR FUTURE RESEARCH .....</b>	 <b>126</b>
6.1 Conclusions.....	126
6.2 Recommendations for Future Research .....	129
 <b>APPENDIX A. GRADIENT BASED OPTIMIZATION SYNTHETIC EXAMPLES.....</b>	 <b>131</b>
A.1 Estimation of Relative Permeabilities with Four Unknown Parameters .....	136
A.2 Estimation of Relative Permeabilities with Four Unknown Parameters and Noisy Observed Data .....	140
A.3 Summary of Gradient Based Optimization Examples.....	145
 <b>APPENDIX B. STOCHASTIC BASED OPTIMIZATION SYNTHETIC EXAMPLES .....</b>	 <b>146</b>
B.1 Estimation of Relative Permeabilities with Seven Unknown Parameters.....	149
B.1.1 Analysis of Single Parameter Trends.....	150
B.1.2 Analysis of Objective Function Values.....	155
B.1.3 Statistical Evaluations .....	157
B.2 Estimation of Relative Permeabilities with Nine Unknown Parameters.....	159
B.2.1 Analysis of Single Parameter Trends.....	160
B.2.2 Analysis of Objective Function Values.....	165
B.2.3 Analysis of Single parameter Trends with Relaxed Margins.....	169

B.3 Estimation of Relative Permeabilities with Nine Unknown Parameters and Noisy Observed Data .....	172
B.3.1 Analysis of Single Parameter Trends .....	172
B.3.2 Analysis of Objective Function Values .....	175
B.3.3 Statistical Evaluations .....	177
 APPENDIX C. STOCHASTIC BASED OPTIMIZATION FIELD EXAMPLES.....	181
C.1 3D Radial-Probe Field Example with Known Capillary Pressure .....	181
C.2 Dual-Packer Field Example without Capillary Pressure .....	186
C.3 Dual-Packer Field Example with Capillary Pressure .....	196
C.4 Large-Diameter Single-Probe Field Example with Capillary Pressure .....	203
 APPENDIX D. STATISTICAL EVALUATION METHODS .....	211
D.1 R-Squared, Root Mean Square Error and Root Mean Square Index .....	211
D.2 Chi-Square Test .....	212
D.3 Pearson Correlation Coefficient .....	212
D.4 Objective Function and Weight Function .....	212
D.5 Use of Statistical Evaluation Methods .....	213
 LIST OF REFERENCES .....	216
NOMENCLATURE .....	225
VITA .....	228

## LIST OF FIGURES

Figure 2.1:	Experimental fluid loss rates for DF before 12 hours and for SF subsequently on the left (Phelps <i>et al.</i> , 1984). The solid and dotted lines in the plot on the left are an experimentally observed invasion and a simplified approximation respectively. In our study the invasion rates follow DF rate as in solid line and SF rate as in dotted line from the experimental data and redrawn on the right .....	12
Figure 2.2:	Segment structure of the multisegment well model adapted from Holmes <i>et al.</i> (1998) .....	17
Figure 2.3:	Modified Brooks and Corey model with its parameters .....	26
Figure 2.4:	LET model with its parameters .....	27
Figure 2.5:	Killough hysteresis model for the non-wetting phase relative permeability behavior .....	30
Figure 2.6:	Killough hysteresis model for the wetting phase relative permeability behavior .....	31
Figure 2.7:	Killough hysteresis model for the water capillary pressure .....	33
Figure 2.8:	Evolution strategy in a stochastic optimization initiates a set of simulations, which are distributed over the entire parameter range (top image). It will converge gradually around several local optima (in this example maximums of an objective function) by using a fitness based process. It continues by eliminating the worst performing datasets and recombines the desirable ones as the progress is seen from top to bottom. It can search discontinuous and non-linear spaces (MEPO User Training Materials, 2015) .....	39
Figure 2.9:	Gradient based optimization in a multi-parameter field. The initial condition may lead a local maximum in this maximization example. Several colored optimization paths are depicted with different initial conditions and results .....	40
Figure 3.1:	A typical WFT string for the pressure measurement, cleanup and sampling.....	41
Figure 3.2:	DP inlet module with an interval length of 3.33 ft (left), 3DRP probe with a flow area of 79.44 in <sup>2</sup> (middle), XLD single probe with a flow area of 2.01 in <sup>2</sup> (right).....	43
Figure 3.3:	Capacitance pressure sensor (top), bonded wire strain pressure sensor (middle), crystal quartz gauge pressure sensor (bottom) (Fundamentals of Formation Testing, 2006) .....	44
Figure 3.4:	A single-probe pretest measurement (Wireline Formation Testing and Sampling, 1996).....	45
Figure 3.5:	A sketch of pump rates and pressures of a dual-packer (red) and a single-probe (green) inlets during an IPTT operation. The dual-packer is the pulsing module and the single-probe is the observing module .....	46

Figure 3.6:	Absorption spectra displaying signatures of water and different types of hydrocarbon (top). Absorption spectra focusing on the hydrocarbon peak for its components and CO <sub>2</sub> (bottom) .....	47
Figure 3.7:	WFT measurements during the periods of pretesting, cleanup and IPTT test .....	49
Figure 4.1:	Mud-filtrate Invasion design illustrating dynamic (before 0.5 day) and static (after 0.5 day) filtration periods of the synthetic numerical model .....	51
Figure 4.2:	Relative permeability and capillary pressure curves of the synthetic numerical model assumed for both mud-filtrate invasion and WFT cleanup measurements .....	51
Figure 4.3:	Radial gridding of the model is displayed in several sections. The top left and the top right graphs depict the top and the cross-sectional views of the entire model respectively. The bottom left and the bottom right graphs show the near wellbore region from the top and the cross-sectional zone where the DP inlet is set respectively. The red lines on the left show the absolute locations of the cross sections displayed on the right.....	54
Figure 4.4:	Base case runs with different innermost radial grid sizes having an impact on the pressure drawdown and the water-cut measurements during the cleanup process. The vertical grid size across the DP inlet is 0.5 cm. The multisegment well model is applied to the DP inlet .....	55
Figure 4.5:	Base case runs with the innermost radial grid size of 0.25 cm. The vertical grid size across the DP inlet is modified. When the vertical grid height is less than 5 cm, the similar results are obtained. The multisegment well model is not applied to the DP inlet in this case .....	56
Figure 4.6:	Numerical model results of 3DRP inlet at the sandface. The image of the unfolded wellbore is shown where 3DRP inlet performs the mud-filtrate cleanup. Colors in the grids represent the fluid saturations. Red color shows oil and blue color depicts WBM filtrate at the end of the cleanup period.....	57
Figure 4.7:	Cross-section ( $\theta$ -Z) of a numerical grid for a large-diameter (LD) single-probe. Green cells represent the flow area (0.85 in <sup>2</sup> ), red cells represent the sealing packer around the SP inlet, and blue cells are a part of the sandface .....	58
Figure 4.8:	Responses of the bottomhole pressures (above) and the water-cuts (below) are shown for the runs having various maximum allowed timesteps. The insets focus on the oil breakthrough and the early cleanup periods where larger changes occur .....	59
Figure 4.9:	Completion schematic of the multisegment well model representing the DP interval with its dimensions .....	61
Figure 4.10:	Water-cut (top) and bottomhole pressure (bottom) behaviors are displayed during the DP cleanup at the sandface and at the fluid analyzer.....	62

Figure 4.11: Comparisons of the DP inlet multiphase and homogenous flow options. The multiphase flow generates a segregated flow while the homogenous flow uses an average density of the phases in the inlet storage. H, F, A are hydrostatic, friction, and acceleration terms, respectively and their combinations can be used in the multisegment flow runs .....	63
Figure 4.12: Water saturation progress during the WBM filtrate invasion in the near-wellbore region at the center of the DP interval in the presence of capillary pressure.....	65
Figure 4.13: Oil pressure progress during the WBM filtrate invasion in the near-wellbore region at the center of the DP interval in the presence of capillary pressure .....	65
Figure 4.14: Water and oil block pressures during the progress of the WBM filtrate invasion in the near-wellbore region at the center of the DP interval in the presence of capillary pressure.....	66
Figure 4.15: Capillary pressures during the progress of the WBM filtrate invasion in the near-wellbore region at the center of the DP interval.....	66
Figure 4.16: Water saturation profiles including the invasion, cleanup and pressure buildup events depicted in the near-wellbore region at the center of the DP interval in the presence of capillary pressure .....	68
Figure 4.17: Pressure profiles including the invasion, cleanup and pressure buildup events illustrated in the near-wellbore region at the center of the DP interval in the presence of capillary pressure .....	68
Figure 4.18: Water and oil block pressures during the progress of the cleanup in the near-wellbore region at the center of the DP interval in the presence of capillary pressure.....	69
Figure 4.19: Capillary pressures during the progress of the DF, cleanup, and at the end of the pressure buildup in the near-wellbore region at the center of the DP interval.....	69
Figure 4.20: A radial-vertical (R-Z) cross-sectional view of the near wellbore region at the end of the DP cleanup. The DP is located at the center left (displayed as a black vertical line). The grid is zoomed to a height of 10.76 ft from the top, and to a distance of 32.73 ft into the reservoir from the wellbore. The arrows represent the cleanup direction .....	70
Figure 4.21: Cleanup event detailing the changes of pressures, rates and relative permeabilities at the center of the DP interval. The periods are marked as A, B, C, D, which are before, at, early after and late after the oil breakthrough, respectively.....	72
Figure 4.22: Cleanup event detailing the oil breakthrough period of Figure 4.21 .....	73
Figure 4.23: Cleanup event showing the pressure drawdown, water-cut, and rate across the DP interval before (A), at (B), early after (C), late after (D) the oil breakthrough.....	73
Figure 4.24: Cleanup event showing the water saturation, oil and water relative permeabilities across the DP interval before (A), at (B), early after (C), late after (D) the oil breakthrough .....	74



Figure 4.25: History match comparison of the 0.1-Day DF vs. the base case. DF influx rate is increased. SF influx rate and cumulative invasion volume are kept equal to the base case. The matches of bottomhole pressures and water-cuts are acceptable as seen on the left.....	76
Figure 4.26: History match comparison of the 0.2-Day DF vs. the base case. DF influx rate is reduced. Static filtration influx rate is increased to match the cumulative invasion of the base case before the cleanup. The matches of bottomhole pressures and water-cuts are not acceptable. This is due to an increased water saturation profile (red curve in the middle plot) near the wellbore just before the cleanup starts .....	76
Figure 4.27: History match comparison of the 1-Day DF vs. the base case. The SF influx rate and the total volume of invasion are kept equal to the base case. The matches of bottomhole pressures and water-cuts are acceptable as seen on the left.....	77
Figure 4.28: Comparison of continuous SF vs. no SF, while both cases share the same DF profile .....	77
Figure 4.29: DF saturation profiles with different oil and water viscosities in the near wellbore area.....	79
Figure 4.30: SF saturation profiles with different oil and water viscosities in the near wellbore area.....	79
Figure 4.31: Water saturation profiles at the end of the cleanup with different oil and water viscosities in the near wellbore area .....	80
Figure 4.32: Viscosity contrasts influencing the oil breakthrough and the bottomhole pressure during the cleanup period.....	80
Figure 4.33: Water saturation profiles at the end of the DF, at the beginning and the end of the cleanup at the center of the DP interval in the anisotropy cases.....	82
Figure 4.34: Water saturation profiles at the end of the DF, at the beginning and the end of the cleanup at the top of the DP interval in the anisotropy cases.....	82
Figure 4.35: Water saturations are presented across the DP interval at the sandface (A), at 8 in (B), 15 in (C) and 22 in (D). The center of the DP interval is at 5.5 ft and the height of the DP interval is 3.3 ft residing between 3.8 ft and 7.1 ft from the top of the reservoir. The horizontal permeability is kept unchanged, but the vertical permeability is altered in the anisotropy cases .....	83
Figure 4.36: $k_h$ is 20 md and $k_v/k_h$ is 0.6 in the base case. $k_h$ is not changed, but $k_v/k_h$ ratio is altered to 0.3, 1, and 2 .....	84
Figure 4.37: Cleanups are conducted with the three different porosities. The porosity is equal to 0.3 in the base case.....	85
Figure 4.38: Saturation profiles at the end of the DF period, at the beginning and the end of the cleanup for the porosity cases of 0.3, 0.2 and 0.1. The invasion volumes and durations are kept the same as in the base case ...	86
Figure 4.39: Damage skin values are compared during the cleanup. The base case has the damage skin of 2.....	87

Figure 4.40: Water saturation profiles for the skin factors of 0, 2, and 4 at the end of the DF period, at the beginning and the end of the cleanup .....	87
Figure 4.41: Capillary pressure curves used for the sensitivity analyses. The curve with the black markers represents the capillary pressure in the base case. The capillary pressures are generated with the modified Brooks and Corey capillary pressure correlation .....	89
Figure 4.42: Water saturation profiles with the capillary pressure curves at the end of the DF period displayed from the wellbore to 36 in into the reservoir .....	89
Figure 4.43: Water saturation profiles with the capillary pressure curves at the beginning of the cleanup displayed from the wellbore to 36 in into the reservoir .....	90
Figure 4.44: Water saturation profiles with the capillary pressure curves at the end of the cleanup displayed from the wellbore to 36 in into the reservoir ...	90
Figure 4.45: WFT bottomhole pressures and water-cuts are displayed with the capillary pressure sensitivities. The black curves represent the base case. Higher $P_d$ and lower $\lambda$ values create a higher capillary pressure at $S_{wi}$ and generate relatively an earlier oil breakthrough .....	91
Figure 4.46: WFT bottomhole pressures and the water-cuts during the cleanup when the capillary pressure is applied and later ignored for the two sets of equal fluid viscosities .....	92
Figure 4.47: Water saturation profiles at the end of DF (top), before the cleanup (middle), and after the cleanup (bottom) when the capillary pressure is applied and later ignored for the two sets of equal fluid viscosities ....	93
Figure 4.48: WFT bottomhole pressures and water-cuts during the cleanup. All of the cases have identical DF periods and matching SF rates with various SF durations .....	95
Figure 4.49: Water saturation profiles for each case before the cleanup in the vicinity of the wellbore. All of the cases have identical DF periods as in the blue curve and the matching SF rates with various SF durations .....	96
Figure 4.50: Water saturation profiles for each case at the end of the cleanup in the vicinity of the wellbore. All of the cases have identical DF periods and the matching SF rates with various SF durations .....	96
Figure 4.51: Progress of relative permeabilities and capillary pressures in a hysteretic process at the shallower to deeper locations in the reservoir. Orange arrows show the direction of the imbibition process while purple arrows display the direction of the drainage process .....	98
Figure 5.1: Diagram of the stochastic based optimization process .....	100
Figure 5.2: Radial gridding of the synthetic SBO example is displayed in an R-Z cross-sectional view .....	112
Figure 5.3: Water saturation progress of the mud-filtrate invasion and the cleanup in the near-wellbore region at the center of the DP interval for the model used in the synthetic SBO example .....	112

Figure 5.4:	Partial objective functions are plotted against the individual parameters. Table 5.5 summarizes the first cycle results from the single parameter trends .....	115
Figure 5.5:	Partial objective functions are plotted against the individual parameters. Table 5.6 summarizes the second cycle results from the single parameter trends. The second cycle is conducted with the narrower ranges of the parameters obtained from the first cycle analysis .....	116
Figure 5.6:	Relative permeability curves and capillary pressures are estimated with their optimal ranges from the single parameter trends in the second iteration cycle .....	117
Figure 5.7:	Relative permeability and capillary pressure curves from the LHS forward runs having the lowest five GOF values are plotted. The runs are listed in Table 5.7 .....	118
Figure 5.8:	History match results from the LHS forward runs having the lowest five GOF values as listed in Table 5.7.....	118
Figure 5.9:	Relative permeability and capillary pressure curves from the LHS forward runs having the lowest five GOF values obtained from the calculation of $1*WBHP + 0.01*WCUT$ are plotted. The runs are listed in Table 5.8 .....	119
Figure 5.10:	History matches from the runs having the lowest five GOF values obtained from the calculation of $1*WBHP + 0.01*WCUT$ as listed in Table 5.8 .....	120
Figure A.1:	Definitions of EPS parameters for the oil-water relative permeabilities.....	133
Figure A.2:	Radial gridding of the GBO synthetic examples is displayed in an R-Z cross-sectional view .....	135
Figure A.3:	Water saturation progress during the events of invasion, cleanup and buildup is displayed in the near-wellbore region at the center of the DP interval in the GBO synthetic examples .....	135
Figure A.4:	Final match of the bottomhole pressures (top) and water-cuts (bottom) during the optimization of four parameters in the example A.1 .....	137
Figure A.5:	Improvement of four modifiers and RMS index values during the progress of the optimization in the example A.1 .....	138
Figure A.6:	Relative permeability curves of the parameter optimization from the initial estimate, observed and final match with non-noisy observed datasets in the example A.1 .....	139
Figure A.7:	Pressure buildup transient analyses of the observed and matched bottomhole pressures. The pressure derivatives confirm a very similar skin factor created by altering the transmissibility values at the innermost radial grid column in the example A.1 .....	139

Figure A.8: Observed bottomhole pressures (top) and water-cuts (bottom) are displayed with their noise levels. The Gaussian noises are implemented for the observed water-cuts and bottomhole pressures in the example A.2. The water-cut has no noise during the flow of mud filtrate and the pressure buildup. The bottomhole pressure has no noise during the pressure buildup.....	141
Figure A.9: Improvement of four modifiers and RMS index values during the progress of the optimization in the example A.2. The observed bottomhole pressures and water-cuts are altered with the Gaussian noises .....	142
Figure A.10: Final match of the bottomhole pressures (top) and water-cuts (bottom) with the noisy observed datasets during the optimization of four parameters in the example A.2 .....	143
Figure A.11: Relative permeability curves from the initial estimate, observed and final match of the four parameter optimization in the example A.2. The observed bottomhole pressures and water-cuts are altered with the Gaussian noises.....	144
Figure A.12: Pressure buildup transient analyses of the observed and matched bottomhole pressures. The pressure derivatives confirm a very similar skin factor created by altering the transmissibility values at the innermost radial grid column in the example A.2 .....	144
Figure B.1: Radial gridding of the synthetic example is displayed in an R-Z cross-sectional view .....	148
Figure B.2: Water saturation progress of the mud-filtrate invasion and the cleanup in the near-wellbore region at the center of the DP interval in the synthetic example .....	149
Figure B.3: First iteration estimate of <i>korw</i> is between 0.54 and 0.71 from WBHP.....	151
Figure B.4: First iteration estimate of <i>TIME1</i> is between 16 and 18 from WCUT ..	151
Figure B.5: First iteration estimate of <i>SKIN</i> is between 0.64 and 1.76 from WBHP.....	151
Figure B.6: First iteration estimate of <i>LW</i> is between 1.47 and 4.74 from WBHP ..	151
Figure B.7: First iteration estimate of <i>EW</i> is between 0.99 and 4.15 from WBHP and between 2.38 and 2.63 from WCUT.....	151
Figure B.8: First iteration estimate of <i>LO</i> is 0.54 and 2.53 from WBHP .....	152
Figure B.9: First iteration estimate of <i>EO</i> is between 2.04 and 4.47 from WBHP and between 1.71 and 3.54 from WCUT.....	152
Figure B.10: Second iteration estimate of <i>korw</i> is between 0.57 and 0.61 from WBHP. The best value of <i>korw</i> is 0.59 .....	153
Figure B.11: Second iteration estimate of <i>TIME1</i> is 16 from WBHP and GLOBAL, and 17 from WCUT .....	153
Figure B.12: Second iteration estimate of <i>SKIN</i> is between 0.76 and 1.07 from WBHP. The best value of <i>SKIN</i> is 0.94.....	153

Figure B.13: Second iteration estimate of $LW$ parameter is between 2.19 and 3.08 from GLOBAL. The best value of $LW$ is 2.77 .....	153
Figure B.14: Second iteration estimate of $EW$ is between 2.28 and 3.28 from WCUT. Most likely $EW$ range is between 2.53 and 3.28. The best value is 2.53 if 3.28 is an outlier.....	154
Figure B.15: Second iteration estimate of $LO$ is between 0.88 and 1.14 from GLOBAL. The best value of $LO$ is 1.14.....	154
Figure B.16: Second iteration estimate of $EO$ parameter is between 2.33 and 3.23 from GLOBAL. The best value of $EO$ is 3.08.....	154
Figure B.17: Relative permeability curves are estimated with their optimal ranges from the single parameter trends in the second iteration cycle .....	155
Figure B.18: Relative permeabilities are estimated from the runs having the lowest five global objective values in Table B.7 .....	156
Figure B.19: Bottomhole pressure and water-cut history matches from the runs having the lowest five global objective values in Table B.7 .....	157
Figure B.20: Results of the evaluation methods suggest that the two best history matches are IT:17_DS:392 and IT:17_DS:1015 .....	158
Figure B.21: Relative permeability curves of the two best history matches from the results of the statistical evaluation analyses are displayed. The best match is IT:17_DS:392 from the statistical evaluation analyses.....	158
Figure B.22: Bottomhole pressure and water-cut of the two best history matches obtained from the statistical evaluation analyses are presented. The best match is IT:17_DS:392 from the statistical evaluation analyses ...	159
Figure B.23: First iteration estimate of $swi$ is between 0.14 and 0.18 from WBHP ..	160
Figure B.24: First iteration estimate of $sor$ is around 0.13, but the range can also be between 0.11 and 0.22 from WCUT.....	160
Figure B.25: First iteration estimate of $korw$ is around 0.61 from WCUT and between 0.59 and 0.77 from WBHP .....	161
Figure B.26: First iteration estimate of $TIMEI$ is between 15 and 19 from WCUT ..	161
Figure B.27: First iteration estimate of $SKIN$ is between 0 and 1.69 from WBHP ....	161
Figure B.28: First iteration estimate of $LW$ is between 2.1 and 3.7 from WBHP .....	161
Figure B.29: First iteration estimate of $EW$ is between 1.7 and 4.2 from WCUT.....	161
Figure B.30: First iteration estimate of $LO$ is between 0.7 and 1.8 from WBHP.....	162
Figure B.31: First iteration estimate of $EO$ is between 1.8 and 4.0 from WBHP and between 3.0 and 3.2 from WCUT when outliers are excluded.....	162
Figure B.32: Second iteration estimate of $swi$ is between 0.161 and 0.168 from GLOBAL .....	163
Figure B.33: Second iteration estimate of $sor$ is between 0.132 and 0.158 from GLOBAL .....	163
Figure B.34: Second iteration estimate of $korw$ is between 0.566 and 0.722 from WBHP.....	163

Figure B.35: Second iteration estimate of <i>TIME1</i> is between 15 and 18 from GLOBAL .....	164
Figure B.36: Second iteration estimate of <i>SKIN</i> is between 1.053 and 1.378 from GLOBAL .....	164
Figure B.37: Second iteration estimate of <i>LW</i> is between 1.620 and 2.827 from WCUT .....	164
Figure B.38: Second iteration estimate of <i>EW</i> does not show a single range and it represents non-uniqueness. The values range between 1.644 and 3.915 from WBHP, which are at the bounding limits of the iteration...	164
Figure B.39: Second iteration estimate of <i>LO</i> is between 0.937 and 1.714 from WBHP.....	164
Figure B.40: Second iteration estimate of <i>EO</i> is between 1.593 and 3.237 from WBHP.....	165
Figure B.41: Relative permeability curves are estimated by using the LET method from the single parameter trends achieved from the second iteration cycle.....	165
Figure B.42: Relative permeabilities are generated by the LET method for the runs having the nine lowest global objective values. The grouped curves show the expected range of the solution.....	167
Figure B.43: History matches of the runs having the lowest nine global objective values .....	167
Figure B.44: Results of the evaluation methods of the runs having the lowest nine global objective values .....	168
Figure B.45: Relative permeabilities are generated for the run having the best history match confirmed by the statistical evaluations and the lowest global objective value .....	168
Figure B.46: History match of the best run with the lowest global objective value, which is also confirmed by the statistical evaluations.....	169
Figure B.47: Box shows the relaxed margins of <i>LO</i> as (0.609, 2.314) and the POF values are limited to 3e+5 for the forward run selection.....	170
Figure B.48: Relative permeability curves are generated by applying 35% relaxed margins for <i>sor</i> , <i>swi</i> , <i>korw</i> , <i>EO</i> , <i>LO</i> , <i>EW</i> , <i>LW</i> and the POF cutoff of 3e+5 .....	170
Figure B.49: History matches of the bottomhole pressures and water-cuts of the runs with the relaxed margins and the POF cutoff .....	171
Figure B.50: Estimate of <i>TIME1</i> is 16. <i>TIME1</i> ranges between 15 and 17 from WCUT .....	173
Figure B.51: Estimate of <i>SKIN</i> is 0.888. <i>SKIN</i> ranges between 0.888 and 1.165 from WBHP .....	173
Figure B.52: Estimate of <i>swi</i> is 0.147. <i>swi</i> ranges between 0.144 and 1.172 from WBHP.....	173
Figure B.53: Estimate of <i>sor</i> is 0.192. <i>sor</i> ranges between 0.153 and 0.192 from WBHP.....	173

Figure B.54: Estimate of $korw$ is 0.608. $korw$ ranges between 0.597 and 0.632 from WCUT and WBHP .....	173
Figure B.55: Estimate of $LW$ is 2.668. $LW$ ranges between 2.484 and 2.981 from WCUT and WBHP .....	174
Figure B.56: Estimate of $EW$ is 2.267. $EW$ ranges between 2.267 and 2.897 from WCUT .....	174
Figure B.57: Estimate of $LO$ is 1.387. $LO$ ranges between 0.762 and 1.387 from WCUT and WBHP .....	174
Figure B.58: Estimate of $EO$ is 2.758. $EO$ ranges between 2.758 and 3.628 from WCUT and WBHP .....	174
Figure B.59: Relative permeability curves are estimated by using the LET method from the single parameter trends .....	175
Figure B.60: Relative permeability curves are from the runs having the lowest five global objective values as listed in Table B.13 .....	176
Figure B.61: History matched datasets are from the runs having the lowest five global objective values as listed in Table B.13 .....	177
Figure B.62: Observed bottomhole pressures (top) and water-cuts (bottom) are displayed with their noise levels. Gaussian noises are implemented for the observed water-cuts and bottomhole pressures in the example B.3. The water-cut has no noise during the flow of mud filtrate.....	178
Figure B.63: Results of the statistical evaluations are shown from the runs having the lowest five global objective values in Table B.13.....	179
Figure B.64: Relative permeability curves from the best match suggested by the results of the statistical evaluations in Figure B.63 .....	179
Figure B.65: History match of the best run suggested by the results of the statistical evaluations in Figure B.63.....	180
Figure C.1: Depth view of the openhole logs in the field example C.1.....	183
Figure C.2: WFT pressure transient analyses during the pretest and the pressure buildup. Blue and green plots on the left represent the analyses of the 3DRP pretest and the post cleanup pressure buildup, respectively. PAQP refers to as the quartz pressure gauge in the DP inlet .....	184
Figure C.3: Capillary pressures are generated by the Thomeer model honoring the reservoir height, saturation and FWL .....	184
Figure C.4: The best history match, along with the relative permeabilities is highlighted for the 3DRP field example in Appendix C.1. The WFT cleanup has a constant rate of 9.4 bbl/day .....	185
Figure C.5: Depth view of the openhole logs in the field example C.2. Simulation Invasion track (second on the right) shows the laterolog invasion in line with the actual invasion profile .....	187
Figure C.6: Results from the well test analysis used for the initialization of the model prior to the relative permeability estimation in the example C.2.....	188

Figure C.7: Oil saturation is generated as a function of depth and radial distance from the wellbore using the numerical model. Three snapshots in time are presented: before the cleanup (left), at the oil breakthrough (center), and the final stage of the cleanup (right). Horizontal lines indicate the DP interval. The wellbore is located on the left of each image .....	190
Figure C.8: Final match between measured and simulated pressures and water-cuts for the DP field example in Appendix C.2.....	191
Figure C.9: Final relative permeability curves for the DP field example in Appendix C.2.....	191
Figure C.10: Sensitivity of matched DP cleanup history to changes in irreducible water saturation ( $swi$ ).....	193
Figure C.11: Sensitivity of matched DP cleanup history to changes in residual oil saturation ( $sor$ ).....	193
Figure C.12: Sensitivity of matched DP cleanup history to changes in oil relative permeability endpoint ( $koro$ ).....	194
Figure C.13: Sensitivity of matched DP cleanup history to changes in water relative permeability endpoint ( $korw$ ) .....	194
Figure C.14: Sensitivity of matched DP cleanup history to changes in invasion depth (left) and skin (right). (No effect on relative permeabilities) .....	194
Figure C.15: Sensitivity of matched DP cleanup history to changes in Corey water exponent ( $nw$ ) .....	195
Figure C.16: Sensitivity of matched DP cleanup history to changes in Corey oil exponent ( $no$ ).....	195
Figure C.17: Depth view of the openhole logs in the field example C.3.....	197
Figure C.18: Results from the pressure buildup analysis recorded at the sampling station. The horizontal permeability is 10.3 md. The geometrical and damage skin factors for the partial completion thickness are 9.5 and 8.5, respectively in the example C.3.....	198
Figure C.19: DF and SF influx volumes and rates for the field example in Appendix C.3.....	200
Figure C.20: Water saturation progress at the center of the DP interval from the drilling until the end of the WFT logging in the example C.3. The openhole logging and the WFT cleanup are conducted 1.467 days and 5.092 days after the drilling, consecutively .....	200
Figure C.21: Final match between measured and simulated pressures and water-cuts for the DP field example in Appendix C.3. Pressure drawdown response before 0.5 hr does not match well due to more viscous fluid (mud) flow instead of mud-filtrate flow .....	201
Figure C.22: Final relative permeability and capillary pressure curves for the DP field example in Appendix C.3.....	201



Figure C.23: Cross-sections of the reservoir properties in the near-wellbore region during the WFT cleanup corresponding to the pumpout time of 1.33 hrs. Flowing pressures, oil saturations, and horizontal and vertical oil velocities are presented from top to bottom respectively. The DP interval is located between XX86.03 and XX89.36 ft.....	202
Figure C.24: Depth view of porosity, permeability, and pressure distribution in the reservoir for the field example C.3. The center of the DP inlet is at 20.6 ft measured from the top of the reservoir. The plot represents the pressure behaviors throughout the reservoir during the periods of pre-drilling, invasion, logging, WFT sampling and pressure buildup .....	203
Figure C.25: Depth view of the openhole logs in the example C.4 (Ramaswami <i>et al.</i> , 2010). The boundaries of the flow unit tested with the WFT large-diameter single probe are highlighted with black lines .....	206
Figure C.26: Pressure transient analysis match from the WFT pressure gauge (left) and the pressure history match (right) in the example C.4.....	206
Figure C.27: Near-wellbore cross-sectional saturation images of the flow unit passing through the center of the probe are displayed at different time events. Oil saturation is from 0.1 (blue) to 0.8 (red). The flow unit thickness is 0.8 m. The large-diameter single probe is located at 0.3 m from the top (displayed as an arrow). The horizontal image axes represent the radial distance from the sandface into the formation. The images are: the end of DF at 0.5 day (left), the laterolog time for comparison and the invasion profile from the laterolog as a black curve at 2.0 days (second left), the beginning of WFT cleanup at 6.592 days (middle), the end of WFT cleanup at 6.724 days (second right), the end of WFT pressure buildup at 6.737 days (right).....	207
Figure C.28: DF and SF influx volumes and rates for the field example in Appendix C.4.....	207
Figure C.29: Invasion progress at the cleanup depth from the drilling until the end of the WFT logging at the large-diameter single-probe setting depth in the example C.4. The openhole logging is conducted 2 days after drilling. The WFT cleanup is started 6.724 days after drilling and takes less than 4 hours .....	208
Figure C.30: Final match between measured and simulated pressures (top) and water-cuts (bottom) for the large-diameter single-probe field example in Appendix C.4.....	209
Figure C.31: Final relative permeability (left) and capillary pressure (right) curves for the large-diameter single-probe field example in Appendix C.4.....	209
Figure C.32: Global objective function values versus individual parameters in the example C.4. Lower values suggest a better history match for a particular parameter .....	210
Figure D.1: Weight function distribution on the observed water-cut dataset .....	213
Figure D.2: A synthetic example of the statistical evaluation methods of goodness-of-fit in comparison of models and data.....	214
Figure D.3: Results of the statistical evaluation methods are displayed such that the lower values from all the methods present a better match.....	215

## LIST OF TABLES

Table 1.1:	Summary of the literature review for generation of relative permeability and capillary pressure curves .....	8
Table 4.1:	Invasion, cleanup and buildup parameters. The cleanup rate is for the circular grid and the radius of invasion is an average value at the end of the dynamic filtration .....	52
Table 4.2:	Reservoir properties of the synthetic numerical model .....	52
Table 4.3:	Fluid properties of the synthetic numerical model. The fluid viscosities and densities are at downhole and surface conditions respectively .....	52
Table 4.4:	Grid properties of the synthetic numerical model .....	52
Table 5.1:	Parameters of invasion, cleanup and pressure buildup are listed in the synthetic SBO example. The cleanup rate is for the circular radial grid.....	111
Table 5.2:	Reservoir properties of the synthetic model in the synthetic SBO example.....	111
Table 5.3:	Fluid properties of the synthetic model in the synthetic SBO example. The fluid viscosities and densities are at downhole and surface conditions respectively .....	111
Table 5.4:	Grid properties in the synthetic SBO example .....	111
Table 5.5:	Ranges of the parameters are obtained from the analysis of single parameter trends in the first cycle of the SBO example. The parameters are not fixed for the next cycle. The results are finalized from Figure 5.4 .....	114
Table 5.6:	Ranges of the parameters are obtained from the analysis of single parameter trends in the second cycle of the SBO example. The results are finalized from Figure 5.5 .....	114
Table 5.7:	LHS forward runs having the lowest five GOF values are listed. WBHP and WCUT are not weighted in this section; $a$ and $b$ are both equal to one.....	117
Table 5.8:	POF values of bottomhole pressures (WBHP) and water-cuts (WCUT) are weighted with $a$ and $b$ , which are set to 1.0 and 0.01 respectively. The resulting GOF values are listed from the lowest to the highest values.....	119
Table A.1:	EPS parameters and their designed (observed) values are listed in the GBO synthetic examples. Unused or lacking parameter modifiers are marked with '-' .....	133
Table A.2:	Invasion, cleanup and buildup properties in the GBO synthetic examples .....	133
Table A.3:	Reservoir properties in the GBO synthetic examples.....	134
Table A.4:	Fluid properties in the GBO synthetic examples. The fluid viscosities and densities are at downhole and surface conditions respectively.....	134

Table A.5:	Grid properties in the GBO synthetic examples .....	134
Table A.6:	EPS parameter modifiers for the optimization of four parameters with the non-noisy water-cuts and bottomhole pressures in the example A.1 .....	136
Table A.7:	Final EPS parameters calculated from the modifiers for the optimization of four parameters with the non-noisy water-cuts and bottomhole pressures in the example A.1 .....	137
Table A.8:	EPS parameter modifiers for the optimization of four parameters with the noisy water-cuts and bottomhole pressures in the example A.2.....	140
Table A.9:	Final EPS parameters calculated from the modifiers for the optimization of four parameters with the noisy water-cuts and bottomhole pressures in the example A.2.....	141
Table B.1:	Invasion, cleanup and buildup parameters of the synthetic example are tabulated. The cleanup rate is for the full circular grid and the radius of invasion is an average distance at the end of the mud-filtrate invasion.....	147
Table B.2:	Fluid properties of the synthetic example are listed. Fluid viscosities and densities are at downhole and surface conditions respectively.....	147
Table B.3:	Reservoir properties of the SBO synthetic example.....	148
Table B.4:	Grid properties of the SBO synthetic example.....	148
Table B.5:	LHS strategy results in the first cycle of the example B1 .....	150
Table B.6:	LHS strategy results in the second cycle of the example B1.....	152
Table B.7:	LHS forward runs are sorted by their global objective values from the lowest to the highest in the synthetic example B1.....	156
Table B.8:	LHS strategy results in the first cycle in the example B.2 .....	160
Table B.9:	ES results in the second cycle in the example B.2 .....	163
Table B.10:	List of the partial and global objective values from the forward runs are tabulated in the order from the lowest to the highest in the example B.2.....	166
Table B.11:	Parameter ranges are obtained from a relaxed margin search of 35% for <i>sor</i> , <i>swi</i> , <i>korw</i> , <i>EO</i> , <i>LO</i> , <i>EW</i> , <i>LW</i> and the POF values are limited to $3e+5$ .....	171
Table B.12:	LHS strategy results from the forward runs in the example B.3 .....	172
Table B.13:	List of the partial and global objective values from the forwards runs are tabulated in the order from the lowest to the highest in the example B.3.....	176
Table C.1:	Reservoir and fluid properties in the field example C.1 .....	183
Table C.2:	Parameter results in the optimization cycle for the 3DRP field example in Appendix C.1. The LET model is used for the relative permeability parameterization .....	184
Table C.3:	Reservoir and fluid properties of the field example in Appendix C.2...	189

Table C.4:	Parameter estimates in the optimization cycle for the DP field example in Appendix C.2. The MBC model is used for the relative permeability parameterization .....	189
Table C.5:	Optimum parameter results and single parameter sensitivities for the DP field example in Appendix C.2.....	193
Table C.6:	Reservoir and fluid properties of the field example in Appendix C.3...	197
Table C.7:	Optimizer input ranges and final results are listed for the DP field example in Appendix C.3. The MBC model is used for the relative permeability and capillary pressure parameterization. The known parameters are: <i>totalt</i> = 5.092, <i>khmult</i> = 1, <i>swi</i> = 0.1, <i>sor</i> = 0.168, <i>koro</i> = 1.....	200
Table C.8:	Reservoir and fluid properties of the field example in Appendix C.4...	205
Table C.9:	Optimizer input ranges and final results in the example C.4. The MBC model is used for the relative permeability and capillary pressure parameterization. The known parameters from assumptions or interpretations are: <i>totalt</i> = 6.5882, <i>dynq</i> = 0.02, <i>dynt</i> = 0.5, <i>swi</i> = 0.206, <i>sor</i> = 0.134, <i>koro</i> = 1, <i>khmult</i> = 1.....	208
Table D.1:	Results of the statistical evaluation methods from Figure D.2 are tabulated. The R-squared and Pearson coefficient values are recalculated so that the lower values from all the methods present a better match .....	215

## **LIST OF PUBLICATIONS**

The following papers are published on the subject of this dissertation:

Cig K., Ayan C., Kristensen M., Mackay E. and Elbekshi A.: ‘A Novel Methodology for Estimation of Multiphase Flow Properties from Sampling Data of Wireline Formation Tester’, SPE-170648, SPE ATCE, Amsterdam, the Netherlands, 27-29 October, 2014

Cig K., Ayan C., Kristensen M., Mackay E., Elbekshi A., Naial R.: ‘A Novel Methodology for Estimation of In-Situ Relative Permeabilities from Wireline Formation Tester Data in an Abu Dhabi Carbonate Reservoir’, SPE-171884, ADIPEC, Abu Dhabi, UAE, 10-13 November, 2014

Cig K., Ayan C., Kristensen M., Mackay E.: ‘Numerical Modeling of In-Situ Relative Permeability and Capillary Pressure from Inversion of Wireline Formation Tester Data’, SPE-174381, EUROPEC, Madrid, Spain, 1-4 June, 2015

Cig K., Ayan C., Kristensen M., Mackay E., Liang L., El Battawy A., Ramaswami S., Elshahawi H.: ‘Inversion of Wireline Formation Tester Data to Estimate In-Situ Relative Permeability and Capillary Pressure’, SPE-177451, ADIPEC, Abu Dhabi, U.A.E., 9-12 November, 2015

# **CHAPTER 1. INTRODUCTION**

The last three decades have seen significant developments of wireline formation tester (WFT) technologies contributing to formation evaluation, which has become an essential part of reservoir management. Although WFT had originally been intended for pressure profiling and fluid sampling; with technological advancements and its relatively low cost and minimal environmental impact, its role has expanded significantly in the petroleum industry.

WFT is currently used for pressure measurements and gradients, formation fluid sampling, pressure transient analyses, and micro fracturing applications. Interpretation methodologies originally developed for well testing, drill stem testing (DST), and surface measurements are also incorporated into WFT downhole measurements. The increase of WFT use is not only due to its range of measurements, but also due to its relatively shorter operational duration and its ability to selectively target desired formation units versus depth. The developments of WFT inlets, such as a dual-packer (DP), a 3D radial probe (3DRP), and optical spectroscopy and auxiliary measurements, for example density, and viscosity measurements, have also contributed to novel applications.

## **1.1 Problem Statement**

During drilling of a well, the formation is exposed to mud-filtrate invasion. In the case of water based mud (WBM), the invasion displaces the hydrocarbon in the vicinity of the wellbore, much like a small waterflooding experiment; a case of immiscible displacement of the native formation fluid. A WFT sampling operation follows openhole logs and reduces the contamination levels near the wellbore. The initial mud-filtrate invasion and the following WFT cleanup provide an opportunity for determining in situ relative permeabilities and capillary pressures in an inversion workflow by utilizing data recorded downhole conditions.

This dissertation outlines a full interpretation methodology to obtain multiphase flow properties with an inversion workflow using openhole and WFT logging data. The methodology has an assumption that a single set of relative permeability and capillary pressure curves describes both imbibition and drainage processes. Although, the model uses one set of curves, it still estimates the mud-filtrate invasion volume and its

distribution in the reservoir as in imbibition. The model introduces time dependent components of the mud-filtrate invasion starting from drilling to logging and matches the invasion profile and the saturation distribution interpreted from openhole logs as an initial condition before WFT cleanup starts. The model later replicates WFT cleanup as in drainage. In order to improve the inversion results, WFT tool geometry, drilling, circulation, and logging events are implemented as accurately as possible. The numerical model, which honors openhole logs and WFT cleanup measurements, then generates relative permeability and capillary pressure curves, which in fact is a mix process covering both imbibition and drainage, but constructing a single set of multiphase flow curves.

## **1.2 Objectives**

The focus of the study is to obtain relative permeability and capillary pressure curves from wireline formation tester and openhole logging data. Measuring relative permeabilities and capillary pressures on core samples in a laboratory is an essential, but lengthy process. WFT tools are routinely used in hydrocarbon fields to measure pressures and collect fluid samples. Commonly available data from WFT operations carry information about the multiphase flow properties of the formation. By utilizing in situ WFT measurements and openhole logs, together with a flow model and an optimization engine, we aim to establish a new methodology for estimation of relative permeability and capillary pressure.

## **1.3 Methodology**

The methodology presented here for the estimation of multiphase flow properties is applicable to both oil and gas wells drilled with a water based mud. The model uses accurate WFT tool volume and inlet geometry, which are important for capturing the hydrocarbon breakthrough in an inversion process. In earlier studies, multiphase homogenous flow models are used by neglecting the relative motion between the fluid phases from the sandface to the DP interval (Zeybek *et al.*, 2001; Malik *et al.*, 2006). The homogenous flow model assumes that fluid properties can be represented by mixture properties and single-phase flow techniques can be applied to the mixture. Damage skin and WFT tool storage are not explicitly included in the modeling (Angeles *et al.*, 2008).

In this study we introduce a multisegment well model for the DP inlet due to its large interval volume. The DP design in the numerical model is such that it allows for fluid segregation in its internal storage volume, which captures correctly the arrival time of hydrocarbon at the fluid analyzer. We consider several different WFT inlets. For a single probe (SP) and a 3D radial probe (3DRP) inlets, internal storage volumes are small and can be ignored and the homogenous flow model is suitable to use in their numerical modeling. The SP and DP inlets are studied earlier in the literature with the homogenous flow model, while the 3DRP inlet is introduced for the first time in the literature in this study.

The proposed methodology consists of a numerical forward model describing the mud-filtrate invasion and fluid sampling processes while accurately accounting for the effects of WFT tool geometry, internal tool storage and fluid segregation. The forward model is embedded in an optimization workflow where relative permeability, capillary pressure, damage skin and depth of mud-filtrate invasion are estimated by minimizing a misfit function between measured and modeled pressures and water-cuts. The relative permeability and capillary pressure curves are parameterized using the industry accepted models, such as Modified Brooks and Corey (Lake, 1989), and LET (Lomeland *et al.*, 2005) methods. The optimization workflow uses a distribution function of response parameters, water-cut and bottomhole pressure datasets, where the entire parameter range is included in the numerical runs, thus ensuring that a global optimum is found. The parameters are related to damage skin, mud-filtrate invasion, saturation endpoints, relative permeability endpoints, pore-size distribution index. Initial estimates of some parameters are determined from openhole logs, such as resistivity, dielectric, nuclear magnetic resonance, as well as from pressure transient analyses.

In this study, modeling of the near-wellbore invasion and cleanup processes are investigated. The methodology developed is initially applied to synthetic datasets with known solutions, and it is subsequently established on actual field datasets from WFT sampling jobs. The results demonstrate that it is possible to estimate multiphase flow properties with defined confidence intervals from WFT sampling data. The key contributions of this study are to show the capability of estimating a variety of multiphase flow properties from routine WFT cleanup data and to establish an automated approach in a novel inversion methodology.



## 1.4 Literature Review

When the first WFT tool was introduced by Schlumberger in 1955, its objective was to collect a fluid sample in a cased hole (Lebourg *et al.*, 1956). The first version was only capable of collecting one fluid sample per trip. Since then, the WFT tool has experienced several advancement cycles; the sampling tool was extended to operate in an uncased hole in order to achieve multiple formation pressures and samples in 1975 (Schultz *et al.*, 1975).

A modular WFT tool emerged later to improve pressure measurements and sample qualities in 1990 (Zimmerman *et al.*, 1990). This evolution has allowed new applications, such as low drawdown samples, accurate pressure buildup analyses for permeabilities, and skin factors per unit zone. Multiple inlets were used to identify barriers or obtain vertical and horizontal permeabilities (Ayan *et al.*, 1996). A straddle-packer (dual-packer) module was introduced enabling the isolation of a 1-m interval to target fractures and low permeability formations for pressure transient analyses and sampling (Badry *et al.*, 1993; Pop *et al.*, 1993; Kuchuk *et al.*, 1994).

Spectrometric measurements in WFT fluid analyzers have gone through a significant development process; originally they were used only for oil and water identifications; later improved for hydrocarbon types and compositions with accurate gas-oil ratio (GOR) and condensate-gas ratio (CGR) measurements (Badry *et al.*, 1994; Crombie *et al.*, 1998). WFT stress testing applications were introduced in 1999 (Desroches and Kurkjian, 1999). Auxiliary measurements, such as resistivity, pH, coloration, florescence, salinity, density, and viscosity measurements were introduced throughout the years (Ayan *et al.*, 2006; Dong *et al.*, 2007). Mobilities calculated from pressure measurements became an important indicator of permeabilities although they use a single phase approach and do not account for relative permeabilities or capillary pressures. Pressure transient analyses have provided zonal permeabilities and productivity index (PI) values (Kin *et al.*, 2010).

Openhole logs, meanwhile, such as gamma ray, density, porosity and resistivity, have improved their reliability and accuracy since their inception (Galford *et al.*, 1986; Flaum *et al.*, 1989; Eyl *et al.*, 1994; Barber *et al.*, 1995). Nuclear magnetic resonance logs have provided rock properties and pore-size distributions as well as capillary pressure estimations (Kenyon *et al.*, 1989; Baldwin and Yamanashi, 1991). Dielectric logging

was introduced to deliver fluid, matrix and geological structural analyses; especially useful when Archie exponents of  $m$  and  $n$  are not readily available from core analyses (Hizem *et al.*, 2008). Routine and special core analyses, although these take relatively longer time to perform, continue to be the industry standard for measuring the rock and fluid properties, such as fluid saturation, wettability, capillary pressure, absolute and relative permeabilities, porosity and pore-size distribution (Unalmiser and Funk, 1998).

Single-phase well test interpretations have been widely used in the industry and multiphase pressure transient analyses were also presented for complex reservoir systems (Perrine, 1956; Al-Khalifah *et al.*, 1987; Ayan *et al.*, 1988; Raghavan, 1989; Ramakrishnan *et al.*, 1994; Kuchuk *et al.*, 2010). Goode and Thambynayagam (1996) looked into invaded zone effects on WFT pressure transient analyses. Gok *et al.* (2003) investigated invaded zone parameters and estimated them from WFT DP and SP inlets in an inversion model.

Effects of mud-filtrate invasion and mud-cake growth have been studied extensively and forward models have been developed (Dewan and Chenevert, 1993; Carlson *et al.*, 1996; Proett *et al.*, 2001; Wu *et al.*, 2005; Zinati *et al.*, 2007). Studies examined the modeling of the mud-filtrate invasion by integrating both resistivity and WFT data. Semmelbeck and Holditch (1988) used a two-phase fluid flow model to generate the mud-filtrate invasion integrating mud-cake permeability. Their approach included induction logging, which is sensitive to salt concentration in the porous medium. Semmelbeck *et al.* (1995) improved their previous study by integrating the fluid flow model with Dewan and Chenevert's mud-cake model, which was an experimental model defining mud-cake growth and filtration mechanisms.

Near-wellbore saturation distributions due to mud-filtrate invasion are interpreted with novel petrophysical interpretations of openhole logs. Estimation of relative permeability and capillary pressure are related to mud-filtrate invasion and the calculation of the saturation distribution in the multiphase flow environment of the near-wellbore region. Ramakrishnan and Wilkinson (1997 and 1999) used array induction logging and multiphase fluid flow physics to generate fractional flow and relative permeability curves. Their model ignored capillary and gravity effects. However, their model calculated the invasion fluid loss in the reservoir as well as obtained saturation-dependent

properties for the first time. Zeybek *et al.* (2004) numerically integrated the model of Ramakrishnan and Wilkinson and history matched the WFT water-cuts and bottomhole pressures from the DP inlet. In the study of Zeybek *et al.*, capillary pressures were ignored; however, pressure transient analyses provided permeabilities and the history match of water-cuts and flowing pressures yielded relative permeability curves. This study also ignored phase segregation effects within the isolated DP interval.

Alpak (2006) and Salazar (2009) conducted a study to analyze invasion profiles in an oil based mud environment. Alpak *et al.* (2004a, 2004b, 2006 and 2008) showed throughout several papers that porosity, relative and effective permeabilities could be inverted from array induction logs and WFT water-cuts and bottomhole pressures. Their study investigated WBM invasion profiles as well as their petrophysical parameter dependencies. Salazar *et al.* (2005 and 2006) extended Alpak's model to gas reservoirs. Salazar's model incorporated the University of Texas at Austin numerical mud invasion simulator developed from the studies of Dewan and Chenevert (1993), and later Wu *et al.* (2003 and 2005). Angeles *et al.* (2008) enhanced Salazar's work with accurately defined rates from the mud-filtrate invasion. Malik *et al.* (2007) quantified the effect of oil based mud (OBM) filtrate invasion on WFT measurements and estimated in situ petrophysical properties. Angeles *et al.* (2009) improved their model later to include deviated wells in oil based mud systems. Liang *et al.* (2011) estimated multiphase flow petrophysical parameters and mud-filtrate volumes by jointly inverting the induction logs with the WFT pressure transient data incorporating capillary pressure and gravitational effects. Liang's work directly inverted the mud-filtrate invasion rates for each flow unit instead of using a complex mud-cake buildup model and this approach simplified the workflow by eliminating the mud-cake growth modeling.

A literature survey on previous studies shows that WFT tool geometry, including the internal tool storage and fluid segregation within the storage volume, has not been accurately captured in the modeling. Different inlet types, such as single probes of varying size, 3DRP inlets, and dual packers, are not fully covered in the literature. Also, inclusion of WFT pressure buildup analyses for vertical and horizontal permeabilities, and damage skin in an inversion workflow is rarely accounted for. Mud-filtrate invasion dynamics and their effects are included in previous studies. However, we have extended this with DF and SF, and investigated invasion profile effects, especially when both

gravity and capillary terms are included. Finally, our study examines both gradient and stochastic based optimization methodologies so as to obtain the parameterized relative permeability and capillary pressure curves with relatively low computational cost. Table 1.1 summarizes the previous studies presented in the literature and compares with our study.

Table 1.1: Summary of the literature review for generation of relative permeability and capillary pressure curves

<i>Case</i>	<i>Mud Cake Growth Model</i>	<i>Invasion Model</i>	<i>Timeline for logging / WFT</i>	<i>Relative Permeability</i>	<i>Capillary Pressure</i>	<i>Hysteresis</i>	<i>Numerical Model</i>	<i>Property handling</i>	<i>WFT Design</i>
Current study	No	Empirical model of dynamic and static filtrations from Phelps <i>et al.</i> Invasion volume and radius are honored.	Yes. Time gaps between drilling, openhole and WFT logs affect capillary pressures.	Modified Brooks Corey and LET	Modified Brooks Corey and Thomeer	No, but invasion saturation profiles are matched from openhole logs and followed by WFT cleanup.	Numerical model is stochastic and gradient based. Inversion is automated including gravity and capillarity in stochastic model.	Damage skin, $k_h$ , $k_v$ , $S_{wis}$ , $S_{ors}$ , $k_{oro}$ , $k_{orw}$ , heterogeneity, capillarity, invasion	Various WFT inlets and their tool storage, multisegment well model for the DP inlet
Alpak <i>et al.</i>	No	Time-dependent function, a priori information from U. of Texas at Austin model	Yes	Modified Brooks Corey	Modified Brooks Corey	No	Numerical inversion of array induction measurements	Brine conductivity, resistivity inversion for invasion in an oil reservoir	Single probe or DP inlet without its tool storage or segregation
Angeles <i>et al.</i>	No	Time-dependent function, a priori information from U. of Texas at Austin model	Yes	Modified Brooks Corey	Leverett J-function, Modified Brooks Corey	No	Forward numerical model. Parameters are assumed or manually adjusted.	Resistivity and initial water saturation inversion for invasion. No damage skin is included.	Guard and sampling probes, DP inlet for deviated wells. No WFT tool storage
Liang <i>et al.</i>	No	Constant volume invasion, honoring resistivity inverted invasion profile	Yes	Modified Brooks Corey	Modified Brooks Corey	No	Numerical model uses gradient based inversion with gravity and capillarity.	Reservoir properties, heterogeneity, resistivity inversion for invasion	Single probe or DP inlet without its tool storage or segregation
Malik <i>et al.</i>	No	Oil based mud invasion with known depth of invasion	No	Modified Brooks Corey and curves are kept at $S_{wi}$ .	Leverett J-function modifies $P_c$ with permeability and porosity.	No	Compositional simulator sensitivities	Oil based mud and compositional hydrocarbon mixing model to obtain GOR	Single probe
Proett <i>et al.</i>	Yes, time and mud property dependent	Modeled from mud properties, overbalance, U. of Texas at Austin model	Yes	Modified Brooks Corey	Modified Brooks Corey	No	Forward numerical model	Mud properties and overbalance are used. Saturation profiling is done but no damage skin is included.	No WFT tool storage
Ramakrishnan and Wilkinson	No	Fractional flow curve is generated from array induction logs.	No	Modified Brooks Corey	Buckley Leverett model, no capillarity and no gravity	No	Forward model for water based mud invasion with oil, water and salt transport	Residual and movable saturations, water-cut in the cleanup, the fractional flow curve as a function of saturation are generated.	No WFT tool design
Salazar <i>et al.</i>	No	Time-dependent function, a priori information from U. of Texas at Austin model	Yes	Modified Brooks Corey	Leverett J-function, Modified Brooks Corey	No, only invasion	Numerical inversion of array induction measurements	Brine conductivity, resistivity inversion for invasion in a gas reservoir	No WFT involvement, array induction tool measurements
Wu <i>et al.</i>	Yes, time and mud property dependent	Modeled from mud properties, overbalance, U. of Texas at Austin model	Yes	Modified Brooks Corey	Leverett J-function, Modified Brooks Corey	No	Neural network for history matching	$k_h$ , $k_v$ , porosity and mud properties are used, but no damage skin is included.	No WFT tool storage
Zeybek <i>et al.</i>	No	Manual inputs from Ramakrishnan and Wilkinson calculations	No	Manual modification	No	No	Manual forward model runs	Manual relative permeability modifications and history match, no damage skin	DP inlet without its tool storage or segregation

## **1.5 Outline of Chapters**

Chapter 1 presents the study and its objectives. The methodology of achieving relative permeabilities and capillary pressures is introduced. The literature review investigates the previous studies and the developments of the logging tools and the models throughout the years.

Chapter 2 describes the theory and assumptions, and their mathematical backgrounds. The mud-filtrate invasion is explained. The model for the WFT cleanup process is introduced. Two-phase immiscible flow equations in black-oil fluid models are briefly revisited. The multisegment well model for the flow segregation and tool storage in WFT tool inlets is introduced. Skin factor and its pseudo components are explained. The relative permeability and capillary pressure models used are illustrated. The hysteresis effects of the relative permeability and capillary pressure are demonstrated. Finally, gradient and stochastic based optimization methods are explained.

Chapter 3 explains the WFT tool and its operational details including cleanup, sampling and pressure data acquisition, and inlet types. The WFT tool pressure and fluid analyzer measurements are briefly explained. The operational aspect of interval pressure transient test (IPTT) for vertical and horizontal permeabilities is described.

Chapter 4 presents a synthetic numerical model in detail. Extensive sensitivity analyses are conducted to quantify the model behavior with fluid and rock properties, inlet geometries, and invasion and cleanup processes. The sensitivities have assisted in improving the model before implementing it in field examples.

Chapter 5 focuses on the workflow including the interpretation of openhole and WFT logs, the preparation of the numerical model and the process of attaining the relative permeability and capillary pressure curves. Detailed analyses of optimization methods are included with the synthetic and field examples.

Chapter 6 provides the conclusions of our study that relative permeabilities and capillary pressures can be obtained with a novel methodology from WFT cleanup datasets, and recommendations for the future research.

## CHAPTER 2. THEORY AND ASSUMPTIONS

In this chapter the theory and assumptions and the preferred methods of the model design are introduced with their reasons and limitations.

Mud-filtrate (MF) invasion to and sampling from near-wellbore regions are nonlinear multiphase flow processes with salt and particle transportation. In this study, particle and salt transportation of the mud filtrate is ignored. The study covers two-phase flow of water based mud (WBM) filtrate and a single-phase (under-saturated) hydrocarbon, which may be oil or gas, and does not implement the mud cake development process. Properties of the invading fluid and the reservoir connate water are assumed identical. Their mixing provides a single water phase. Permeability impairment during the invasion is controlled by the components of skin factor.

Capillary, gravitational and viscous forces are included in our study. Low mud-filtrate invasion rates and relatively short depth of invasion, the capillary driven flow plays a crucial role in determining the near wellbore saturation distribution. Gravitational forces are effective and able to create mud-filtrate slumping depending on the invasion volume and time, permeability and its heterogeneity, and the density contrast between mud filtrate and hydrocarbon. Viscous forces are proportional to the velocities of the fluids and naturally incorporated in the modeling.

### 2.1 Invasion Profile

The invasion of a mud filtrate during drilling is described with spurt loss, dynamic and static filtrations in the literature (Allen *et al.*, 1991). It is assumed that mud-filtrate loss is controlled by a filter cake on the sandface of the wellbore. With this approach, the invasion can be introduced explicitly as a parameterized function. This decouples the mud cake buildup event and the invasion. In our model, filtration occurs in three consequent periods as modeled by Phelps *et al.* (1984a, 1984b):

**Spurt loss** occurs when the drill bit cuts the fresh rock and the whole mud flows internally. Its maximum rate may be calculated with an overbalance pressure and a rock permeability from a pressure drawdown equation for an infinite acting reservoir or a pressure drawdown analysis with variable rates (Odeh and Jones, 1965).

**Dynamic filtration** (DF) follows the spurt loss when the mud circulates in the wellbore. DF reduces significantly while the mud cake builds up internally in a short time period. DF rate reduction may be presented with a power law decline curve:

$$q_{DF} = C_1 * t^{-0.5} + C_2 \quad (2.1)$$

where  $q_{DF}$  is dynamic filtration rate,  $t$  is time,  $C_1$  and  $C_2$  are constants related to environmental effects, such as overbalance, initial invasion rate and mud cake buildup.

**Static filtration** (SF) starts after the mud cake sets up and restricts the initial filtration. SF occurs typically when a drill pipe is out of the hole and mud solids are deposited on the cake's outer surface creating an external mud cake. The mud cake development and its quality affect the SF rates. SF does not stop even after the mud cake is well established, although it is much smaller, it continues throughout openhole logging and WFT cleanup. WFT sampling requires that the mud cake is developed and SF rates are lower than WFT cleanup rates. Since WFT sampling is common, this condition is mostly established. When the mud cake is not established with severe mud losses in a wellbore, WFT sampling is not conducted.

SF is presented with a constant rate due to the relatively short time from drilling to logging. During cleanup and sampling, the WFT tool prevents SF across the area covered by the sealing packer element of the inlet, while SF continues elsewhere in the openhole section. The continuing SF does not affect the WFT sampling since the SF rate is relatively low in comparison to the WFT cleanup rate as explained earlier.

Openhole log interpretations can provide invasion fluid volumes and the depth of invasion (DOI) at the time of logging. It has been demonstrated that array resistivity measurements, either induction or laterolog, can be used to establish the radial advance of the invasion profile (Ramakrishnan and Wilkinson, 1997). The method, which uses the radial Buckley-Leverett equation for one-dimensional linear immiscible displacement, can provide an estimate of the invasion profile around the wellbore. The method inverts simultaneously for the total filtrate loss, saturation endpoints and fractional flow. This allows for relative permeabilities to be estimated initially, ignoring effects of gravity and capillarity (Ramamoorthy *et al.*, 2008).



We model the entire mud-filtrate invasion with its dynamic and static components and the WFT cleanup process to be able to generate multiphase invasion and production data as accurately as possible. We investigate the invasion volume during DF and SF and estimate their respective flow rates. The invasion rates and their profiles for DF and SF are based on the experimental data presented in Figure 2.1. Although DF and SF profiles follow their described trends, their magnitudes and durations are parameterized and matched to the invasion volumes obtained from openhole logs, which are recorded during the mud-filtrate invasion in the imbibition process. The invasion process implemented includes gravity and capillarity and allows the invasion front to be affected by any time-lag between the logs. Therefore, accurate schedules of logging runs and well operations, such as drilling, wiper trips can be accounted for in the model.

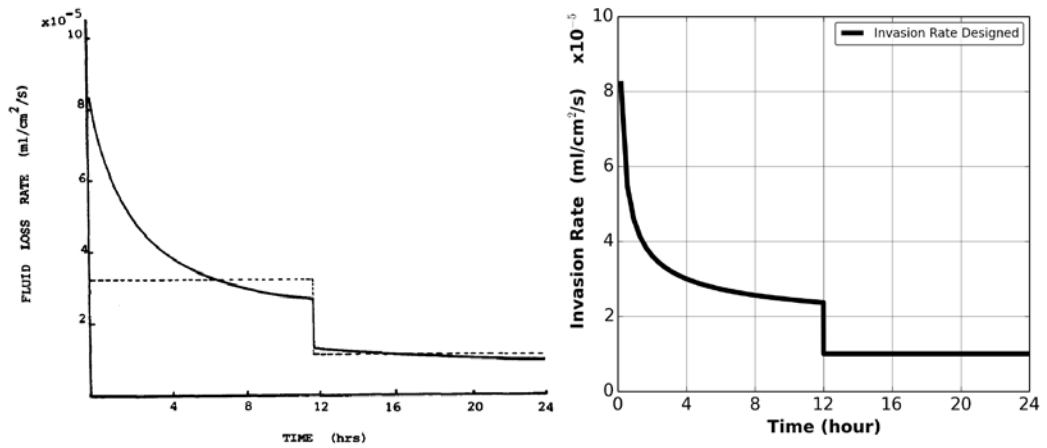


Figure 2.1: Experimental fluid loss rates for DF before 12 hours and for SF subsequently on the left (Phelps *et al.*, 1984). The solid and dotted lines in the plot on the left are an experimentally observed invasion and a simplified approximation respectively. In our study the invasion rates follow DF rate as in solid line and SF rate as in dotted line from the experimental data and redrawn on the right.

## 2.2 Cleanup and Sampling

The WFT cleanup operation represents a secondary drainage process in which hydrocarbon re-saturates the near-wellbore inlet region. As the invasion of the mud filtrate is a water based, the cleanup process is the displacement of the contaminant by hydrocarbon in the near-wellbore area. Although water wet rock examples are mainly presented, there is no wettability assumption in the present study for the cleanup modeling. If a dataset from a field history or coring or openhole logs suggests that the reservoir is oil wet, the methodology remains unchanged and is applicable. The resulting

curves after the inversion may suggest an oil or a water wet system without any limitation in the process.

Primary drainage curves initially govern the reservoir before drilling in our numerical model. The initial stage represents oil ( $1-S_{or}$ ) in the reservoir with irreducible water content ( $S_{wi}$ ) if no transition zone exists. In the case of a transition zone, the primary drainage curves distribute the saturations with an increasing water saturation downward. The initialization assumes the vertical equilibrium and includes capillary and gravity terms. During drilling of the reservoir, mud-filtrate invasion occurs due to mud pressure overbalance, gravitational, viscous and capillary forces. As mentioned earlier, the invasion acts much like a waterflood and the invasion rates are changed according to the mud cake development and overbalance pressure. The invasion can be observed on the saturation distribution in the near-wellbore region during logging and WFT cleanup processes.

The gravitational, viscous and capillary forces, when included in 2D (R-Z) or 3D (R- $\theta$ -Z) models, create a saturation smearing before or during cleanup. The reservoir dynamics introduced with the capillary and gravitational forces should be included during the history matching of the water-cut and bottomhole pressure since the saturation profile changes even after openhole logs and during the cleanup period in the near-wellbore region.

The dominance of the gravitational, viscous and capillary forces will depend on the case controlled by factors, some of which are listed below:

- The mud-cake quality and the duration of mud-filtrate invasion, which affect filtration rates and volumes, DOI
- The formation properties, such as formation thickness, vertical and horizontal permeabilities, porosity and pore size distribution, which influence DOI and invasion fluid slumping, and capillary pressure
- The WFT cleanup rate, which acts against the SF rate
- The oil-water density difference, which changes the invasion fluid slumping and the cleanup profile along with the WFT cleanup rate
- The oil-water interfacial tension and wettability, which guide relative permeability and capillary pressure behaviors

Chapter 4.6 presents synthetic examples how the three forces affect the mud-filtrate invasion and the cleanup behaviors.

### 2.3 Two-Phase Immiscible Flow

The flow of fluids in the model is governed by the principle of mass conversation together with the Darcy's law. The model accounts for the physical properties of the rock and fluids, including porosity, permeability, density, compressibility, and fluid viscosity. The flow of immiscible oil and water phases in a porous medium is governed by a set of partial differential equations. The mass balance equations are formulated for the fluid phases as below (Aziz and Settari, 1979):

$$\frac{\partial(\rho_l \phi S_l)}{\partial t} + \nabla \cdot (\rho_l u_l) = -q_l, \quad l = o, w \quad (2.2)$$

where the subscript  $l$  is the index of a phase, which is water or oil, and  $\nabla$  indicates the differentiation with respect to spatial position ( $R, \theta, Z$ ).

The velocity vector,  $u_l$  is written from the Darcy's law:

$$u_l = -k \cdot \frac{k_{rl}}{\mu_l} (\nabla p_l - \gamma_l \nabla z) \quad (2.3)$$

where  $k$  is the rock permeability,  $k_{rl}$  is the saturation-dependent relative permeability and  $\mu_l$  is the viscosity of phase  $l$ ,  $\gamma_l$  is expressed as  $\rho_l \frac{g}{g_c}$ ,  $g$  is the gravity acceleration, and  $g_c$  is a unit conversion factor. The mobility of phase  $l$  is defined as  $\lambda_l = \frac{k_{rl}}{\mu_l}$ .

Saturation relation is given in the case of water and oil:

$$S_w + S_o = 1 \quad (2.4)$$

Saturation-dependent capillary pressures are:

$$P_c(S_w) = p_{non-wetting} - p_{wetting} = p_o - p_w \quad (2.5)$$

Two-phase flow for a phase can be written:

$$\nabla \cdot [\lambda_l(\nabla p_l - \gamma_l \nabla z)] = \frac{\partial}{\partial t} \left[ \phi \frac{S_l}{B_l} \right] + q_l \quad (2.6)$$

The total source term and the total Darcy velocity are  $q_T = q_w + q_o$  and  $u_T = u_w + u_o$  respectively. The following is obtained from Equation 2.2 in the negligible compressibility case:

$$\nabla \cdot u_T = -q_T \quad (2.7)$$

Darcy's velocities are:

$$u_w = f_w(S_w)u_T + k\lambda_o(S_w)f_w(S_w)[\nabla P_c - \Delta_\gamma \nabla z] \quad (2.8)$$

$$u_o = (1 - f_w(S_w))u_T - k\lambda_o(S_w)f_w(S_w)[\nabla P_c - \Delta_\gamma \nabla z] \quad (2.9)$$

where  $\Delta_\gamma = \gamma_o - \gamma_w$  and  $f_w(S_w) = \frac{\lambda_w}{\lambda_w + \lambda_o}$

Below relations can be written:

$$\nabla P_c = \frac{dP_c}{dS_w}(S_w)\nabla S_w \quad (2.10)$$

$$\nabla \cdot [f_w(S_w)u_T] = \frac{df_w}{dS_w}(S_w)\nabla(S_w) \cdot u_T - f_w(S_w)q_T \quad (2.11)$$

Then the black-oil saturation equation can be obtained as:

$$\begin{aligned} & \frac{\partial S_w}{\partial t} + \left[ \frac{1}{\phi} \frac{df_w}{dS_w}(S_w)u_T \right] \cdot \nabla(S_w) - \nabla \cdot \left[ \frac{\Delta_\gamma k}{\phi} \lambda_o(S_w)f_w(S_w)\nabla z \right] + \\ & \nabla \cdot \left[ \frac{k}{\phi} \lambda_o(S_w)f_w(S_w) \frac{dP_c}{dS_w}(S_w)\nabla S_w \right] + \frac{1}{\phi} [(q_w - f_w(S_w)q_T)] = 0 \end{aligned} \quad (2.12)$$

The first term in Equation 2.12 refers to accumulation, the second to material convection, the third to gravity, the fourth to capillarity and the last to the source terms. For analytical solutions, the latter can either be included in the differential equations or excluded and considered as a boundary condition. If gravity term and capillary pressure gradients are assumed negligible, and  $u_T(x, t) = \frac{Q_T(t)}{A} = u_T(0, t)$  where  $A$  is the reservoir cross-section and  $Q_T(t)$  is the invasion or sampling flow rate through the cross-section  $A$ , then Buckley-Leverett equation can be obtained as:

$$\frac{\partial S_w}{\partial t} + \left[ \frac{Q_T(t)}{A\phi} \frac{df_w}{dS_w}(S_w) \right] \frac{\partial S_w}{\partial x} = 0 \quad (2.13)$$

Equation 2.12 is solved numerically with a fully implicit finite-difference based reservoir simulator (ECLIPSE Reservoir Simulator Technical Description, 2015). The standard method in the simulator is the fully implicit method in which pressures and saturations are solved together. Our study is conducted in a single well penetrating layered hydrocarbon-bearing formations. The well is partially completed and a radial axisymmetric model is used only for the DP inlet, but not for the SP and 3DRP inlets.

## 2.4 Multisegment Well Model

The black-oil simulation is implemented with a multisegment well model in order to describe the fluid flow from sandface to the WFT DP inlet. The model accounts for fluid accumulation and segregation due to the inlet position and geometry and flowline volume within the WFT tool. The fluid flow from the sandface of the wellbore to the fluid analyzer in the WFT tool has a path in which there are flowlines, and volumes for the tool storage. When a DP inlet is used for cleanup, the DP interval accumulates and segregates the fluid phases due to its volume and the inlet position, which is located at one-third from the bottom of its flowing interval. The pressure drop can be calculated from a homogeneous flow model where all the phases are assumed to flow with the same velocity, or alternatively with a drift-flux model that permits a slip velocity between the phases (Shi *et al.*, 2003 and 2004). A homogenous model is not suitable for an accurate definition of segregation of the phases since fluid velocities are assumed same for all phases, even though their flow properties are different.

The multisegment well model implemented in the black-oil simulator is described in detail by Holmes *et al.* (1998). The multisegment well model divides the DP interval into a number of segments as shown in Figure 2.2. The model can also be applicable to a single probe inlet if it has a large storage volume. The number of segments is set up depending on the accuracy required and the count of the surrounding grid blocks designed. Each segment has a node and a flow path to its parent segment node. Each segment also includes outlet and inlet junctions. The former represents a connection in the direction of the wellhead and the latter is a connection away from the wellhead. Each segment has physical properties: length, diameter, roughness, area, and volume. The volume is used in wellbore storage calculations and the other properties are used in the pressure loss calculations.

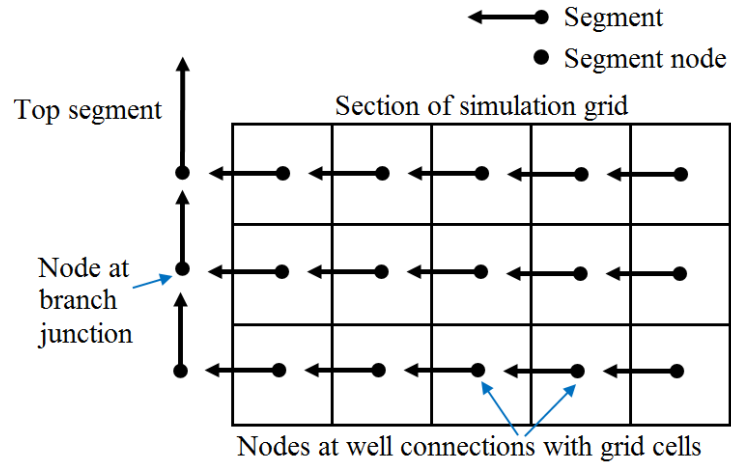


Figure 2.2: Segment structure of the multisegment well model adapted from Holmes *et al.* (1998).

Four variables describe the fluid conditions in each segment:

$$G_T = g_o Q_o + g_w Q_w + g_g Q_g \quad (2.14)$$

$$F_w = g_w Q_w / G_T \quad (2.15)$$

$$F_g = g_g Q_g / G_T \quad (2.16)$$

where  $G_T$  is total fluid flow rate through the segment and is a weighted sum of the oil, water and gas flow rates at surface conditions,  $F_w$  and  $F_g$  are the weighted fractional flows of water and gas at the node,  $P$  is the pressure in the segment as the fourth variable.

The variables are solved for all phases in each segment with material balance equations:

$$R_{pn} = \frac{\Delta m_{pn}}{\Delta t} - \sum_{i \in n} Q_{pi} \sum_{j \in n} q_{pj} + Q_{pn} = 0 \quad (2.17)$$

where  $\Delta m_{pn}$  is the accumulation in the amount of the component  $p$  in the segment  $n$  over the timestep  $\Delta t$ ,  $Q_{pi}$  is the flow rate through each inlet junction  $i$  to segment  $n$ ,  $Q_{pn}$  is the flow rate through the outlet junction of the segment  $n$ ,  $q_{pj}$  is the inflow rate from any reservoir grid block  $j$ , connecting with segment  $n$ , which is obtained from an inflow performance relationship:

$$q_{pj} = J_j \lambda_{pj} (P_j + H_{cj} - P_n - H_{nc}) \quad (2.18)$$

where  $J$  is the connection transmissibility factor of the well's connection to the grid block  $j$ ,  $\lambda_{pj}$  is the mobility of the fluids within the grid block,  $P_j$  is the pressure in the grid block connecting with the segment,  $H_{cj}$  is a hydrostatic head correction between the center of the grid block and the depth of the completion, which is calculated from an average of the mobile fluid densities in the grid block,  $P_n$  is the pressure at the node of segment  $n$ ,  $H_{nc}$  is the hydrostatic head between the segment's node depth and the depth of the completion, which depends on the density of the fluid mixture within the segment.

The pressure drop is calculated from the flow rate through its outlet junction with a steady state pressure loss equation:

$$R_4 = P_n - P_{n-1} - \Delta P_H - \Delta P_F - \Delta P_A = 0 \quad (2.19)$$

where  $P_{n-1}$  is the pressure in the neighboring segment in the direction of the wellhead.  $\Delta P$  terms represent the pressure drops across the segment. Subscripts  $H$ ,  $F$ ,  $A$  denote hydrostatic, friction and acceleration terms respectively.

The acceleration pressure loss across a segment is the difference between the velocity head of the mixture flowing across the segment's outlet junction and the velocity heads of the mixture flowing through all its inlet junctions. The friction pressure loss is

calculated from the formation derived from the correlation of Hagedorn and Brown (1965).

The multisegment well model has three methods for calculating the pressure drop across each segment:

1. A homogeneous flow model, which assumes same flow velocities for all phases.
2. A drift flux vertical flow model, which allows different flow velocities for all phases. The drift flux model allows a countercurrent flow regime, where the heavy and light phases flow in opposite directions at low velocities. Hence it can be used to model the segregation of phases in the WFT SP flowlines and DP intervals for cleanup and pressure buildup events. This will allow an accurate oil breakthrough time and a progression of a cleanup.
3. A pre-calculated pressure drop table. The inputs are outlet pressure, flow rate, water fraction and gas fraction in the form of a vertical flow performance table.

## 2.5 Skin Factor

The skin factor is defined as an additional pressure drop due to a flow restriction in the near wellbore-region, which may be related to formation damage, partial penetration, wellbore deviation, multiphase flow, rock compaction around perforation tunnels, and more (Cinco-Ley *et al.*, 1975; Yildiz, 2006).

The total skin factor in a multiphase environment was shown by Raghavan in 1989 and it was adapted to a partial-entry well by Roadifer and Reynolds in 1993:

$$s_T = 1.151 \left[ \frac{\Delta p_{ws}(1hr)}{m} - \log \left( \frac{\bar{\lambda}_t}{\phi \bar{c}_t r_w^2} \right) + 3.23 \right] \quad (2.20)$$

where  $m$  is the slope of the semilog straight line of the pseudo radial flow and is equal to  $dp_{ws}/d\log t_e$ ,  $\Delta p_{ws}(1 hr)$  is the difference between the initial pressure and the wellbore shut-in pressure at 1 hr,  $\bar{\lambda}_t$  is a multiphase thickness-averaged total mobility,  $\bar{c}_t$  is thickness-averaged total compressibility. In order to obtain the damage skin factor, an independent estimate of the pseudo skin factor as a result of limited entry is required (Roadifer and Reynolds, 1993).



Gok *et al.* (2003) presented a multiphase skin factor in the presence of a mud-filtrate invaded zone in a hydrocarbon reservoir (Equation 2.21). Their equation is similar to Hawkins' skin factor, which has the radial flow assumption. In the case of a piston-like displacement by ignoring relative permeabilities, the mobilities represent the endpoint mobilities in the invaded and uninvaded zones. The equation is calculated under the assumption that the invasion occurs in a fully penetrating well in the radial direction under transient conditions:

$$s_{mult} = \left( \frac{1}{M} - 1 \right) \ln \left( \frac{r_i}{r_w} \right) \quad (2.21)$$

where  $M = \lambda_{h,i} / \lambda_{h,u}$ ,  $\lambda_{h,i}$  and  $\lambda_{h,u}$  are horizontal invaded and horizontal uninvaded zone mobilities ( $k/\mu$ ) respectively,  $r_i$  is the invaded zone radius.

The total skin for the full penetration can be written by adding the multiphase skin and the damage skin components:

$$s'_T = \frac{1}{M} s_d + \left( \frac{1}{M} - 1 \right) \ln \left( \frac{r_i}{r_w} \right) \quad (2.22)$$

where  $s_d$  is the damage skin. When  $M = 1$ ,  $s'_T = s_d$

The total skin for a partially completed well is written with the additional skin term for the geometry,  $s_p$ :

$$s_T = s'_T \frac{h}{h_w} + s_p \quad (2.23)$$

The partial penetration skin,  $s_p$  can be obtained from several authors (Odeh, 1980; Papatzacos, 1985; Vrbik, 1991). The partial penetration skin from Odeh is given:

$$s_p = 1.35 \left( \left( \frac{h}{h_w} - 1 \right)^{0.825} \left\{ \ln \left( h \sqrt{\frac{k_h}{k_v}} + 7 \right) - \left[ 0.49 + 0.1 \ln \left( h \sqrt{\frac{k_h}{k_v}} \right) \right] \cdot \ln r_{wc} - 1.95 \right\} \right) \quad (2.24)$$

where  $r_{wc} = r_w e^{0.2126(z_m/h+2.753)}$ ,  $z_m = y + h_w/2$ ,  $y$  is the distance between the top of the sand and the top of the open interval,  $z_m$  is the distance between the top of the sand and the middle of the open interval.

The total skin for a partially completed well can be written with the pseudo components:

$$s_T = \left( \frac{1}{M} s_d + s_{mult} \right) \frac{h}{h_w} + s_p \quad (2.25)$$

The black-oil simulator uses an individual skin factor to encounter all the pseudo effects mentioned including the grid block discretization error. The skin factor in the simulator is defined in the connection factor equation of the inner-most grid block. The radial form of the connection factor equation is presented due to the gridding preference (ECLIPSE Reservoir Simulator Technical Description, 2015):

$$T_{wj} = \frac{c\theta Kh}{\frac{r_2^2}{r_2^2 - r_w^2} \ln(r_2/r_w) - 0.5 + s} \quad (2.26)$$

where  $\theta$  is the angle of the grid block in radians,  $K$  is permeability,  $h$  is thickness,  $s$  is skin,  $r_2$  is the block's outer radius and  $c$  is the unit conversion factor.

We keep the skin factor as a constant throughout the invasion and cleanup events in our numerical model although it could be altered if required. We may obtain the total skin factor from the pressure transient analyses as an initial input; however, the total skin factor from the semilog analysis will not be sufficient to resolve the complexity of all skin components during the numerical simulation. To be specific, the numerical simulation will handle the multiphase skin factor naturally due to its capacity to handle multiphase flow. In addition, the partial penetration skin for various flow inlets will be handled, provided that a fine enough grid is constructed for numerical modeling. The skin factor obtained from a pressure transient analysis is used as a guide during the inversion workflow, after considering the partial penetration skin. For the cited reasons, we choose to always invert for the damage skin factor in our model.

## 2.6 Permeability

Permeability, being a rock property, is constant, irrespective of the fluid flowing through the medium. This is correct when rock is saturated 100% with the same fluid. This is the definition of the absolute permeability. When two different types of fluids, such as oil and water, flow through a porous medium, each fluid has its own permeability, then named as the effective permeability. These permeabilities are dependent on the saturations of the individual fluids. The effective permeability curves are generally normalized by dividing with the absolute permeability to generate the relative permeabilities (Dake, 1995).

$$k_{ro}(S_w) = \frac{k_o(S_w)}{k} \quad (2.27)$$

$$k_{rw}(S_w) = \frac{k_w(S_w)}{k} \quad (2.28)$$

where  $S_{wi} \leq S_w \leq 1 - S_{or}$

The effective permeability curves can also be normalized with the maximum effective permeability to oil,  $k_o(S_w = S_{wi})$ . Then the normalized relative permeabilities are expressed as:

$$k_{ro}(S_w) = \frac{k_o(S_w)}{k_o(S_w = S_{wi})} \quad (2.29)$$

$$k_{rw}(S_w) = \frac{k_w(S_w)}{k_o(S_w = S_{wi})} \quad (2.30)$$

The latter normalization method is adopted throughout this study. One reason is our ability to obtain  $k_o(S_w = S_{wi})$  from the analysis of pressure transients induced by the WFT. Note that contemporary numerical models can handle both definitions.

### 2.6.1 Laboratory Measurements of Relative Permeability

Unsteady-state and steady-state relative permeability methods are commonly used on core samples to measure relative permeabilities under laboratory conditions. Below summarizes the methodologies for oil-water systems.

### 2.6.1.1 Unsteady State Method

In a standard unsteady state method, first  $S_{wi}$  is established on a cleaned core. Then, the core is aged for its wettability restoration for a lengthy period and  $k_o(S_{wi})$  is determined. Later, water is injected into the core from one end, and oil production is observed from the other end. The differential pressure across the core is also recorded throughout the waterflood. The water breakthrough occurs subsequently at the outlet end and effective oil and water permeabilities are calculated based on the oil production and the differential pressure. Progressively water injection rate is increased, and eventually only water is produced by reaching  $S_{or}$  and  $k_w(S_{or})$  is obtained. (Jones and Roszelle, 1978). The following equation is considered satisfactory for the horizontal flow at the negligible capillary pressure for saturation determination (Welge, 1952):

$$S_{w,av} - S_{w2} = f_{o2} Q_w \quad (2.31)$$

where  $Q_w$  is pore volumes of water injected relative to the entire core,  $f_{o2}$  is the fractional flow of oil at the outlet end,  $S_{w2}$  is the water saturation at the outlet end,  $S_{w,av}$  is the average water saturation, equals to  $S_{w,av} = S_{wi} + N_p / V_p$ ,  $N_p$  is the volume of oil produced,  $V_p$  is the pore volume of the core.

$f_{o2}$  is obtained from the slope of the curve defined between  $Q_w$  and  $S_{w,av}$ , and is expressed as:

$$f_{o2} = \frac{q_o}{q_w + q_o} \quad (2.32)$$

With the negligible capillary pressure and the horizontal flow, the unsteady-state method uses the fractional flow of water:

$$f_{w2} = \frac{1}{1 + \frac{k_{ro}}{\mu_o} \frac{\mu_w}{k_{rw}}} \quad (2.33)$$

The fractional flow of water at the outlet,  $f_{w2}$  can also be written as  $f_{w2} = 1 - f_{o2}$ .

The following assumptions are applicable: the core sample is homogenous, capillary equilibrium in the vertical cross-section is held, fluid viscosities are known, relative permeabilities are determined from Equations 2.31 - 2.33, laboratory conditions should meet so that the pressure gradient through the core must be sufficiently high to minimize the capillary end effects and the pressure difference through the core must be sufficiently low in comparison to the total working pressure to make the compressibility effects negligible.

#### 2.6.1.2 Steady State Method

Although there are several steady-state methods available, in the case of a two-phase oil and water experiment, the main approach is to inject a fixed relative rate of oil and water simultaneously into the core until the equilibrium is reached so that pressure drop and fluid saturations across the core do not change. The rates are assumed sufficiently high to minimize the capillary end effects on the flow behavior. After equilibrium is established, two-phase flow rates ( $q_o, q_w$ ) and pressure drop ( $dp/dx$ ) are measured (Richardson *et al.*, 1952). Then, the relative permeabilities of each phase are calculated from the Darcy's law with the known absolute permeability ( $k$ ), cross-sectional flow area ( $A$ ), two-phase viscosities ( $\mu_o, \mu_w$ ) and effective permeabilities ( $kk_{ro}, kk_{rw}$ ):

$$q_o = -\frac{kk_{ro}}{\mu_o} A \frac{dP_o}{dx} \quad (2.34)$$

$$q_w = -\frac{kk_{rw}}{\mu_w} A \frac{dP_w}{dx} \quad (2.35)$$

The procedure is repeated after increasing the water-oil ratio and reaching the equilibrium again until the entire relative permeability-saturation relationship is established.

## 2.6.2 Relative Permeability Models

There are more than 30 models available for the prediction of two-phase relative permeabilities (Siddiqui *et al.*, 1993). The modified Brooks and Corey model is used when a water-wet or oil-wet system is assumed. The LET model can be used when a mixed-wet or weakly water-wet system is present. The following sections describes the relative permeability models used in this study.

### 2.6.2.1 Modified Brooks and Corey Model

Modified Brooks and Corey (MBC) model, also called as power law model, is a function of endpoint relative permeabilities at their respective saturations (Lake, 1989; Semmelbeck *et al.*, 1995) and is given by:

$$S = \frac{(S_w - S_{wi})}{(1 - S_{or} - S_{wi})} \quad (2.36)$$

$$k_{rw}(S) = k_{rw}^o S^{nw} \quad (2.37)$$

$$k_{row}(S) = k_{ro}^o (1 - S)^{no} \quad (2.38)$$

where  $S$  is the normalized saturation, and  $S_{wi}$  and  $S_{or}$  are irreducible water and oil phase saturations, respectively. Relative permeabilities of oil and water phases,  $k_{rw}(S)$  and  $k_{row}(S)$  are calculated by their respective endpoint relative permeabilities of  $k_{rw}^o$  and  $k_{ro}^o$  and their curvature parameters of  $nw$  and  $no$ . The curvature parameters are also named as Corey exponents. Equations 2.37 and 2.38 are derived for drainage conditions. However, throughout our study, the MBC model is also used for imbibition curves, assuming the model is applicable for both imbibition and drainage processes, ignoring the saturation-dependent behavior of the curves. Figure 2.3 depicts the curves generated by the MBC model parameters.

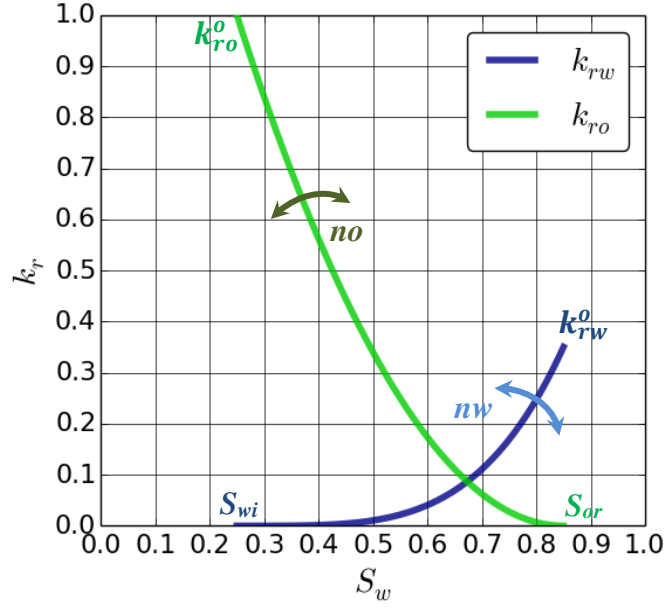


Figure 2.3: Modified Brooks and Corey model with its parameters.

#### 2.6.2.2 LET Model

LET model is a three-parameter correlation method to provide wider curvature flexibilities. The correlation is described by three parameters of  $L$ ,  $E$ ,  $T$  and normalized saturation. Only saturations and relative permeabilities have physical meaning, while  $L$ ,  $E$ , and  $T$  are empirical parameters.  $L$  and  $T$  describe the lower and the upper parts of the curves.  $E$  describes the position of the slope (or the elevation) of the curves (Figure 2.4). The model is flexible to match the shapes of the curves and is applicable for both imbibition and drainage processes (Lomeland *et al.*, 2005):

$$k_{rw}(S) = k_{rw}^o \frac{S^{L_w}}{S^{L_w} + E_w(1 - S)^{T_w}} \quad (2.39)$$

$$k_{ro}(S) = k_{ro}^o \frac{(1 - S)^{L_o}}{(1 - S)^{L_o} + E_o S^{T_o}} \quad (2.40)$$





processes and a drainage capillary pressure curve interpreted from openhole logs can only be a starting point for our optimization.

### **2.7.1 Capillary Pressure Models**

Two drainage capillary pressure models, which are the modified Brooks and Corey model and the Thomeer model, are explained below. The modified Brooks and Corey model is mostly used due to its simple parametric representation. The Thomeer model is exercised when the reservoir showed a water-oil transitional zone.

#### **2.7.1.1 Modified Brooks and Corey Model**

Brooks and Corey (1964) suggested from a large number of experimental data that capillary pressures in a drainage process can be established as a function of normalized saturation, pore-size distribution index,  $\lambda$  and displacement pressure,  $P_d$ :

$$P_c = P_d S^{-1/\lambda} \quad \text{for } P_c \geq P_d \quad (2.41)$$

where  $S$  is the normalized saturation and is obtained from Equation 2.36.

#### **2.7.1.2 Thomeer Model**

Thomeer (1960) presented a curve fit model generated from a relationship of analyzed core samples:

$$\frac{S_b}{S_{b\infty}} = e^{-F_g/(\log P_c/P_d)} \quad (2.42)$$

where  $S_b$  is fractional bulk volume filled with mercury at pressure  $P_c$ .  $S_{b\infty}$  is the fractional bulk volume filled at infinite pressure assuming total porosity.  $S_b/S_{b\infty}$  is equal to the non-wetting phase saturation assuming  $S_{b\infty} = \emptyset$ .  $F_g$  is pore geometrical factor. Equation 2.42 is then written (Wu, 2004):

$$\log P_c = -F_g/\ln(1 - S_w) + \log P_d \quad (2.43)$$

Equation 2.42 is further iterated with the irreducible water saturation by substituting  $S_{b\infty} = \emptyset(1 - S_{wi})$  (Wu and Berg, 2003):

$$\log P_c = -F_g/\ln((1 - S_w)/(1 - S_{wi})) + \log P_d \quad (2.44)$$

## 2.8 Hysteresis

Hysteresis develops when the direction of the saturation change occurs in different cycles during a multiphase flow in a porous medium. An imbibition cycle is defined as a process in which the saturation of the wetting phase increases, and a drainage cycle is defined as a process where the saturation of the non-wetting phase increases during a multiphase flow (Braun *et al.*, 1995). Hysteresis can be explained by interfacial properties of solid and liquid, such as wetting, surface tension, contact angle, solid surface roughness and pore geometry, in which fluid flow may create a bypass, or a snap-off, or an ink-bottle effect (Holm, 1986; Melrose, 1965; Roof, 1970).

If an imbibition or a drainage process is reversed, relative permeability and capillary pressure curves do not trace their previous values; instead scanning curves are created according to hysteresis methods chosen. The hysteresis methods, such as Killough (1976), Carlson (1981) and Jargon (an unpublished study) are available in the black-oil simulator (ECLIPSE Reservoir Simulator Technical Description, 2015). Core analyses are conducted to establish the hysteretic behaviors on the rock samples although they are more laborious. In the literature, measurements of hysteresis are investigated with rock types, rock consolidations, wettability changes, trapping of a phase and methods chosen for the core analyses (Eleri *et al.*, 1995; Dixit *et al.*, 1998; Masalmeh, 2001; Dernaika *et al.*, 2012).

Throughout our study, when the hysteresis method is described -instead of a single set of relative permeability and capillary pressure curves-, the Killough hysteresis model (Killough, 1976) is assumed appropriate and its behavior is explained later. When the hysteresis method is implemented in the study, the aim should be to estimate bounding imbibition and drainage curves although scanning curves are generated according to the Killough hysteresis model. Since reaching saturation endpoints in the near-wellbore region is difficult due to a limited cleanup time with relatively low multiphase flow rates,

the bounding curves are only used for the initialization of the reservoir (primary drainage curves), and during the invasion of the mud filtrate (imbibition curves). The cleanup requires scanning drainage curves depending on the particular block saturation at the end of the imbibition cycle as detailed in Chapters 2.8.1 and 2.8.2.

### 2.8.1 Hysteresis of Relative permeability Curves

When a WBM filtrate invasion occurs in a water wet rock, the imbibition relative permeability and capillary pressure curves are used for the increasing water saturation. When the cleanup is conducted, the drainage scanning curves are followed according to Killough hysteresis model (Killough, 1976).

If the wetting phase saturation decreases down to  $S_{wmin}$  (the green asterisk point in Figures 2.5 and 2.6), the bounding drainage curve is traced. If the imbibition process starts from  $S_{wmin}$ , then the bounding imbibition curve is used. The green arrows depict the bounding drainage and imbibition paths in Figures 2.5 and 2.6. If the drainage process is reversed at a certain saturation (the red asterisk point in Figures 2.5 and 2.6), the relative permeability curve does not follow its previous values, but traces a scanning curve as depicted with red arrows in Figures 2.5 and 2.6. However if the drainage scanning curve is reversed, the same scanning curve is retraced until the bounding curve is reached and then the bounding curve is used again.

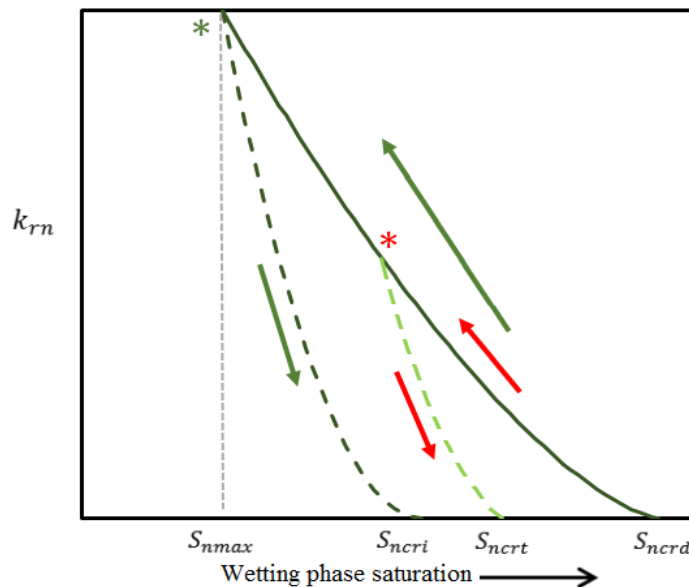


Figure 2.5: Killough hysteresis model for the non-wetting phase relative permeability behavior.

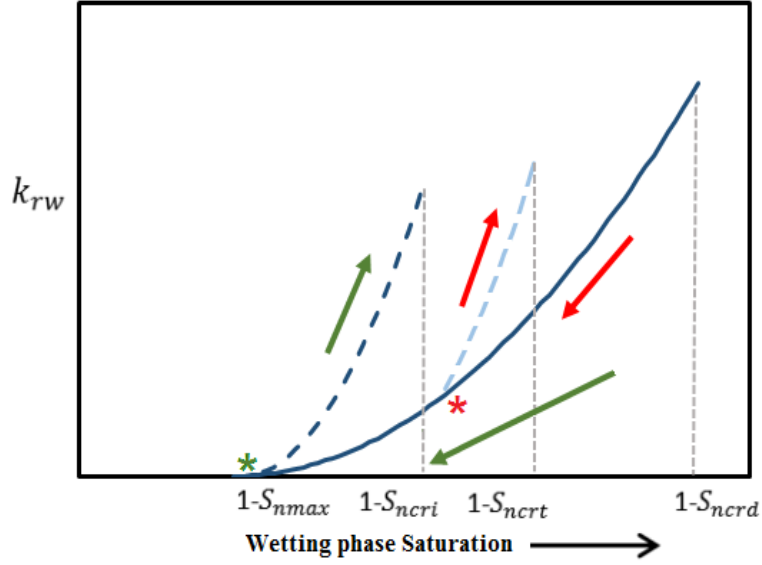


Figure 2.6: Killough hysteresis model for the wetting phase relative permeability behavior.

The bounding drainage (solid dark green) and imbibition (dashed dark green) curves are provided for a numerical run in Figure 2.5. The trapped critical saturation,  $S_{ncrt}$ , of the Killough method is given:

$$S_{ncrt} = S_{ncrd} + \frac{S_{hy} - S_{ncrd}}{1 + C(S_{hy} - S_{ncrd})} \quad (2.45)$$

where

$$C = \frac{1}{S_{ncri} - S_{ncrd}} - \frac{1}{S_{nmax} - S_{ncrd}} \quad (2.46)$$

$S_{ncri}$  and  $S_{ncrd}$  are the critical saturations of the imbibition and drainage curves respectively,  $S_{nmax}$  is the maximum non-wetting phase saturation,  $S_{hy}$  is the maximum non-wetting phase saturation reached in a run, which is presented with a red asterisk point in Figure 2.5.

The relative permeability for  $S_n$  on the scanning curve is obtained:

$$k_{rn}(S_n) = \frac{k_{rni}(S_{norm})k_{rnd}(S_{hy})}{k_{rnd}(S_{nmax})} \quad (2.47)$$

where  $k_{rni}$  and  $k_{rnd}$  are the non-wetting phase relative permeabilities on the bounding imbibition and drainage curves respectively and  $S_{norm}$  is defined:

$$S_{norm} = S_{ncri} + \frac{(S_n - S_{ncrt})(S_{nmax} - S_{ncri})}{S_{hy} - S_{ncrt}} \quad (2.48)$$

The wetting phase relative permeability at the end of scanning curve is calculated:

$$k_{rw}(1 - S_{ncrt}) = k_{rwd}(1 - S_{ncrt}) + (k_{rwi}(1 - S_{ncri}) - k_{rwd}(1 - S_{ncri})) \left( \frac{S_{ncrt} - S_{ncrd}}{S_{ncri} - S_{ncrd}} \right)^A \quad (2.49)$$

where  $k_{rwd}$  and  $k_{rwi}$  are the wetting phase relative permeabilities on the bounding imbibition and drainage curves respectively.  $A$  is the curvature parameter.

The relative permeability on the scanning curve for a specific saturation,  $S_w$  is calculated:

$$k_{rw}(S_w) = k_{rwd}(1 - S_{hy}) + \frac{(k_{rw}(1 - S_{ncrt}) - k_{rwd}(1 - S_{hy})) k_{rwi}(1 - S_{norm})}{k_{rwi}(1 - S_{ncri})} \quad (2.50)$$

### 2.8.2 Hysteresis of Capillary Pressure Curves

Figure 2.7 describes a similar capillary pressure hysteresis process as explained for the relative permeabilities. If wetting phase decreases to  $S_{wmin}$  (the green asterisk point in Figure 2.7), the bounding capillary drainage curve is traced. If the imbibition process starts from  $S_{wmin}$ , then the bounding capillary imbibition curve is used until the wetting saturation  $S_{why}$ . If the drainage process is reversed at a certain saturation (the red asterisk point in Figure 2.7), the capillary pressure curve does not follow its previous values, but traces a new scanning curve (as depicted with red arrows following dashed brown curve in Figure 2.7). When the scanning curve reverses second time (at the blue asterisk point), unlike relative permeability scanning curves, it does not necessarily re-trace the scanning curve and may follow a new scanning curve generated from the previous scanning curve and the drainage curve (as depicted with the blue arrow following solid brown curve in Figure 2.7).

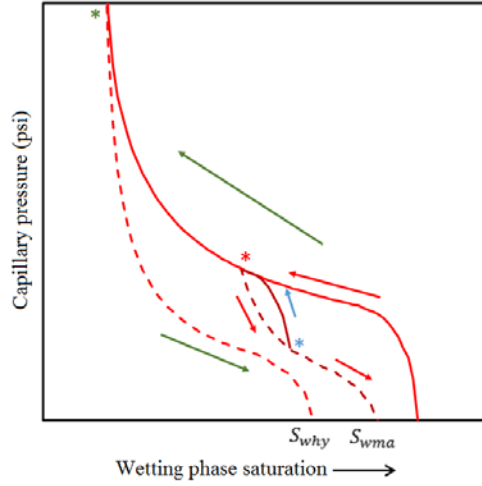


Figure 2.7: Killough hysteresis model for the water capillary pressure.

Killough capillary pressure hysteresis is given:

$$P_c = P_{cd} + F(P_{ci} - P_{cd}) \quad (2.51)$$

$$F = \left( \frac{1}{S_w - S_{why} + E} - \frac{1}{E} \right) / \left( \frac{1}{S_{wma} - S_{why} + E} - \frac{1}{E} \right) \quad (2.52)$$

where  $E$  is curvature parameter,  $S_{why}$  is the water saturation at the hysteresis reversal point (red asterisk),  $S_{wma}$  is the maximum water saturation achievable for the trapped non-wetting saturation,  $P_{cd}$  is the drainage capillary pressure,  $P_{ci}$  is the imbibition capillary pressure obtained by the capillary pressure on the imbibition curve after scaling between the endpoints  $S_{wcri}$  and  $S_{wma}$ ,  $S_{wcri}$  is the critical water saturation on the imbibition capillary pressure curve.

When the second reversal starts from the blue asterisk point until the drainage curve is reached to the red asterisk point as depicted in Figure 2.7, the capillary pressure equation is written:

$$P_c = P_{ci} + G(P_{cd} - P_{ci}) \quad (2.53)$$

$$G = \left( \frac{1}{S_{dep} - S_w + E} - \frac{1}{E} \right) / \left( \frac{1}{S_{dep} - S_{why} + E} - \frac{1}{E} \right) \quad (2.54)$$

where  $S_{dep}$  is the departure saturation.

## 2.9 Optimization

A number of techniques are available to improve the history matching in a numerical simulation. The optimization used for the history matching is a problem of minimization of an objective function. Both gradient and stochastic based optimization techniques are used in our study. The study first investigates the gradient based optimization (GBO) with two examples in Appendix A. The GBO results show that the black-oil simulator chosen does not have necessary parameters for relative permeability and capillary pressure curvatures. Then, the stochastic based optimization (SBO) is explored for the realistic results in Appendix B. The SBO methodology with the help of additional software programming scripts provides the required parameterization flexibility in relative permeability and capillary pressure curvatures, and additional benefits (see Chapter 5.4 for details).

### 2.9.1 Gradient Based Optimization

The mismatch of simulated vs. observed data is quantified by an objective function. The goal of optimization is to find the solution that minimizes this function. In the gradient based optimization, the optimizer searches for a minimum using a gradient of the objective function with respect to the parameters being optimized. A necessary condition for optimality is that the first derivative (gradient) of the objective function is equal to zero. A sufficient condition for optimality is that the Hessian matrix (i.e. matrix of second derivatives) is positive definite.

The optimization algorithm works as follows: First, it updates input parameters. Secondly, it runs the updated dataset in a numerical simulator and generates newly simulated variables. The gradients of the solution variables, which are required to construct the objective function gradient, are also calculated during the model run. In order to solve for the minimum objective function value, both the gradient and the Hessian matrix are required. Hessian matrix calculations are computationally intensive and an approximation method, such as the Levenberg-Marquardt (Levenberg 1944; Marquardt, 1963) method can be implemented in the optimizer. Thirdly, the non-linear regression algorithm in the optimizer reads the newly calculated gradient values and variables, and then calculates the objective function. Using the gradient information, the changes required in the history matching parameters to reduce the objective function are

computed. The process is repeated until an acceptable history match is achieved or further progress is unattainable. The “best” history match is obtained with the smallest possible objective function and provides the parameters required for generating the final relative permeabilities and capillary pressures from the WFT bottomhole pressures and water-cut values.

Optimization parameters used in our study:

$$dynq, dynt, statq, k_h, k_v, k_{ro}, k_{rw}, no, nw, P_d, SKIN, S_{or}, S_{wi}, \lambda$$

$$\underline{x} = [dynq, dynt, statq, k_h, k_v, k_{ro}, k_{rw}, no, nw, P_d, SKIN, S_{or}, S_{wi}, \lambda]^T \quad (2.55)$$

Observed variables:

$$P_i, \quad i = 1, \dots, n_T \quad (2.56)$$

$$WCUT_j, \quad j = 1, \dots, n_T \quad (2.57)$$

Objective function:

$$Q(\underline{x}) = \frac{1}{2} \sum_i^{n_T} w_i (P_i(\underline{x}) - P_i^o)^2 + \frac{1}{2} \sum_j^{n_T} w_j (WCUT_j(\underline{x}) - WCUT_j^o)^2 \quad (2.58)$$

$$Q(\underline{x}) = \frac{1}{2} \sum_k^{2n_T} f_k(\underline{x})^2 = \frac{1}{2} \underline{f}^T(\underline{x}) \underline{f}(\underline{x}) \quad (2.59)$$

Taylor expansion for  $Q(\underline{x})$  yields:

$$Q(\underline{x} + \underline{h}) = Q(\underline{x}) + \underline{h}^T \frac{\partial Q}{\partial \underline{x}} + \frac{1}{2} \underline{h}^T \frac{\partial^2 Q}{\partial \underline{x}^2} \underline{h} + o(\|\underline{h}\|^3) \quad (2.60)$$

where  $\|\underline{h}\|$  is very small.

Necessary condition for optimality:

$\frac{\partial Q}{\partial \underline{x}} = 0$ , which is the gradient and finds a local minimum (or maximum) of the objective function.



Sufficient condition for optimality:

$\frac{\partial^2 Q}{\partial x^2}$  is positive definite.

### 2.9.1.1 Solving Non-Linear Least Squares Problems

When Newton's method is applied to  $\frac{\partial Q}{\partial x} = 0$ , we have:

$$0 = \frac{\partial Q}{\partial \underline{x}}(\underline{x} + \underline{h}) = \frac{\partial Q}{\partial \underline{x}}(\underline{x}) + \frac{\partial^2 Q}{\partial \underline{x}^2} \underline{h} + o(\|\underline{h}\|^2) \quad (2.61)$$

when  $\underline{h}$  is sufficiently small:

$$0 \simeq \frac{\partial Q}{\partial \underline{x}}(\underline{x}) + \frac{\partial^2 Q}{\partial \underline{x}^2} \underline{h} \quad (2.62)$$

$$\frac{\partial^2 Q}{\partial \underline{x}^2} \underline{h} = -\frac{\partial Q}{\partial \underline{x}}(\underline{x}) \quad (2.63)$$

Equation 2.63 is solved to obtain  $\underline{h}$  in an iteration by initially setting  $\underline{x} = \underline{x}_o$ . Then,  $\underline{x}$  is updated with  $\underline{x} = \underline{x}_o + \underline{h}$  and a new value of  $\underline{h}$  is calculated. The iteration continues until the finishing criterion is satisfied (Frandsen *et al.*, 1999). Equation 2.63 requires both the gradient and Hessian matrix of the objective function to solve. The Hessian matrix is particularly difficult to obtain since it requires second derivatives.

The Levenberg-Marquardt method is characterized by a particular way of approximating Hessian matrix, which avoids calculating the second derivatives. Madsen *et al.* (2004) gives the Levenberg-Marquardt equation as:

$$(\mathbf{J}(x)^T \mathbf{J}(x) + \mu \mathbf{I})h = -\mathbf{J}(x)^T f(x) \quad , \mu \geq 0 \quad (2.64)$$

where  $\mathbf{I}$  is identity matrix and  $\mu$  is Lagrange parameter.

When  $\mu$  is large,  $h$  approximates to:

$$h \simeq -\frac{\mathbf{J}(x)^T f(x)}{\mu} \quad (2.65)$$

Equation 2.65 represents a short step in the steepest-descent direction. If  $\mu$  is very small, it means that the iteration is nearly at final stages and quadratic final convergence can be obtained.

$\mu$  is updated during the optimization and the initial  $\mu$  value links with the size of the elements in the Jacobian matrix:

$$\mu_0 = \tau \cdot \max_i \{ \mathbf{J}(x_0)^T \mathbf{J}(x_0) \} \quad (2.66)$$

### 2.9.2 Stochastic Based Optimization

Stochastic based optimization (SBO) uses the objective function to compare the model quality among different simulations. A partial objective value is calculated for each response parameter. The global objective value of a simulation is the sum of the partial objective values for all response parameters that are active. Tuning the objective function is typically performed by applying weight on response parameters. The optimizer applies a sampling strategy to the parameter ranges while attempting the history matching. The parameters are either the model inputs or the functions that calculate the model inputs. The parameters typically are damage skin, depth of mud-filtrate invasion, curvature exponents and endpoint saturations of relative permeabilities as similarly defined in GBO (see Equation 2.55). The match is obtained when the global objective function value is at a minimum.

A common initial parameter sampling strategy is Latin hypercube sampling (LHS), which screens the entire parameter ranges in defined compartments and assembles a sample of plausible collections of parameter values for the simulation runs (McKay *et al.*, 1979). The simulation results are analyzed to observe the global optimum in a minimization process. In some cases, the history matching may contain a number of local optima due to a large number of unknown parameters. In this case, a second cycle of optimization can be performed with either Latin hypercube or evolution strategy. The latter is a direct search method and focuses on reducing objective function values to determine a new search step, and does not require any gradient information from the optimization problem. The advantage of the evolution strategy is that it can be used in cases where no gradient information is available and a gradient based algorithm fails because of nonlinearities or discontinuities in the search space (Schulze-Riegert *et al.*, 2002). The Latin hypercube

and evolutionary strategies are suitable to use in parallel computing runs in order to speed up the numerical optimization processes.

Relative permeability and capillary pressure curves are the product of the “best” history match obtained by the minimization of the objective function defined by a strategy. Ideally, the best match should come from an optimization run, which provides comparably the lowest global objective value, and generates relative permeabilities and capillary pressures from its collective set of parameters. In our study, both Latin hypercube and evolution strategy are used. A Latin hypercube strategy may require a larger number of model runs. The match quality can be checked with model evaluation methods, such as R-Squared, Root Mean Square Error (RMSE), Chi-Square Test, and Pearson Correlation Coefficient (see Appendix D). Alternatively, an evolutionary strategy uses fewer parallel model runs in generating parent-to-child sequences since it updates the search direction with the model results.

Gradient based optimization is generally sensitive to the initial values chosen for the optimization parameters, and the minimization process may result in a local minimum of the objective function instead of a global minimum. When the relationships of the parameters are more complex, a stochastic optimization method, although it may be more expensive in computation, can assist in finding the global minimum with different strategies. A maximization example shows the difference between the stochastic and gradient based optimizations in Figures 2.8 and 2.9.

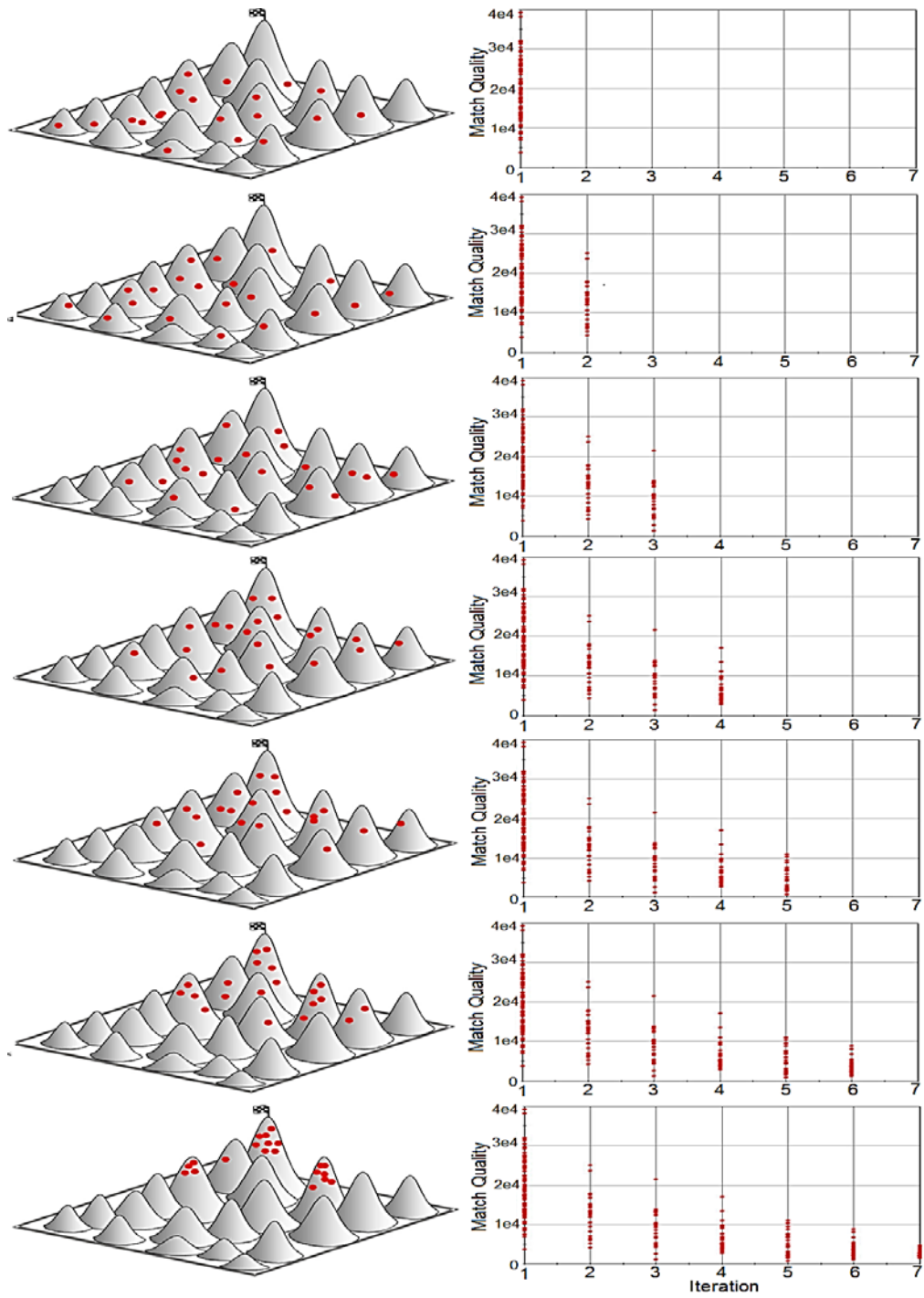


Figure 2.8: Evolution strategy in a stochastic optimization initiates a set of simulations, which are distributed over the entire parameter range (top image). It will converge gradually around several local optima (in this example maximums of an objective function) by using a fitness based process. It continues by eliminating the worst performing datasets and recombines the desirable ones as the progress is seen from top to bottom. It can search discontinuous and non-linear spaces (MEPO User Training Materials, 2015).

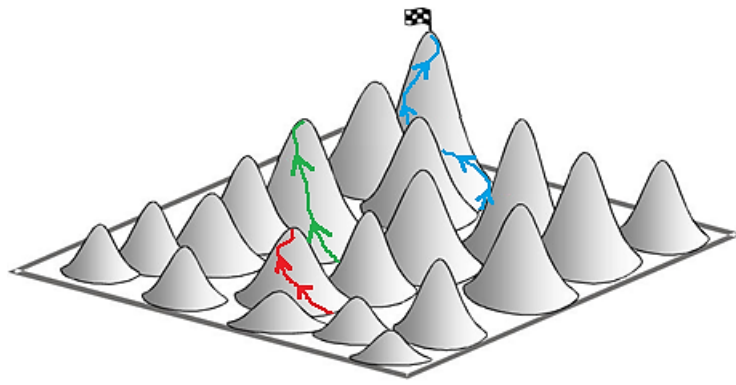


Figure 2.9: Gradient based optimization in a multi-parameter field. The initial condition may lead a local maximum in this maximization example. Several colored optimization paths are depicted with different initial conditions and results.

### CHAPTER 3. WIRELINE FORMATION TESTER LOGGING

A wireline formation tester (WFT), a modular logging tool, measures pressures, collects samples, conducts well tests, and performs stress tests in openhole conditions as depicted in Figure 3.1 (Zimmerman *et al.*, 1990). Logging objectives determine the operational modules in the WFT string. A pressure measurement (pretest) in general requires a single-probe inlet with its hydraulic unit. A cleanup procedure consists of a pump for creating a pressure drawdown and flowing fluids from the formation through the WFT tool into the wellbore and overcoming the downstream pressure difference; an inlet for establishing a hydraulic communication with the formation by isolating the wellbore; and a fluid analyzer for differentiating the fluid types passing through the WFT flowline (Mullins, 2008). A sampling objective further demands PVT-quality bottles to fill. A variety of inlet types, such as a single probe (SP), a dual-packer (DP) module, a 3D radial probe (3DRP) is available (Dios *et al.*, 2012, Cantini *et al.*, 2013). A combination of operational objectives, reservoir and fluid properties determines the inlet types and sizes. A larger flow area of an inlet provides a lower pressure drawdown with a given pump rate. The inlet types are chosen depending on the operational objectives, such as formation pressure measurements, pressure drawdown limits during sampling, interference testing, or stress testing.

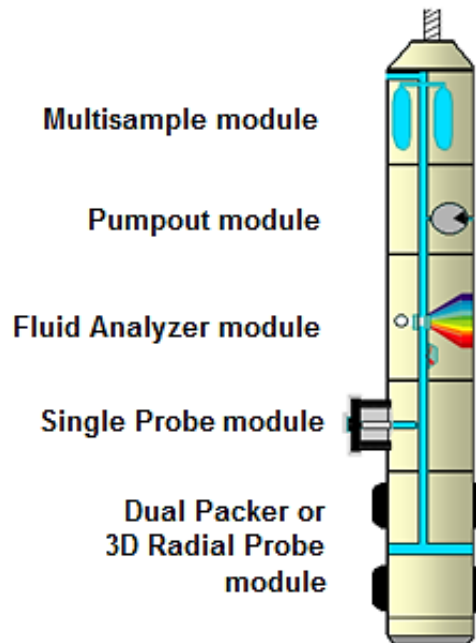


Figure 3.1: A typical WFT string for the pressure measurement, cleanup and sampling.

### 3.1 Inlet Types

The dual-packer (DP), 3D radial probe (3DRP), and single probe (SP) inlets are used in this study (Figure 3.2). The DP inlet has an interval length of 3.33 ft with an inlet port located 13 in from the top of the lower rubber element. The storage volume of the DP interval residing in between upper and lower rubbers is approximately 17 L in 8.5 in openhole. The fluid flow from the reservoir enters into the DP interval and segregates as hydrocarbon accumulates above water. This represents a cleanup event in a hydrocarbon reservoir with a WBM filtrate invasion. A sufficient volume of hydrocarbon has to accumulate in the DP interval before entering into the flowline from its inlet port. The black-oil numerical simulation using a multisegment well model includes this segregation in the DP interval for an accurate cleanup design (see Chapter 2.4).

The 3DRP inlet comprises four elliptically-shaped suction probes, distributed at 90 degree intervals around the circumference of the WFT tool. The total flowing surface area of the 3DRP inlet is 79.44 in<sup>2</sup> (Cig *et al.*, 2014). The advantage of the 3DRP inlet is to have a larger flow area in comparison to a regular single probe and to contain a negligible storage volume unlike the DP inlet.

The extra-large diameter (XLD) single probe is a circular-type probe with a flow area of 2.01 in<sup>2</sup>. It is generally used for pressure measurements and for sampling of high permeability zones (Cig *et al.*, 2014).

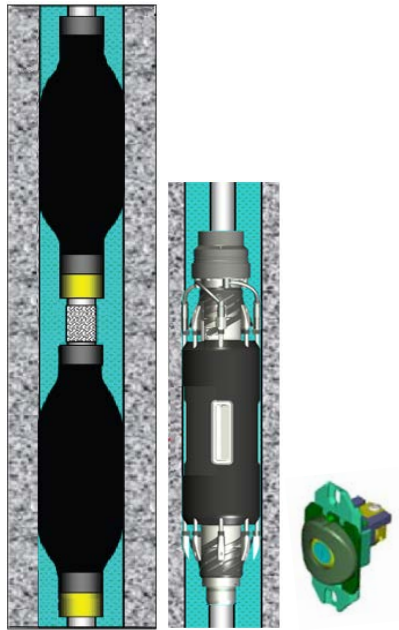


Figure 3.2: DP inlet module with an interval length of 3.33 ft (left), 3DRP probe with a flow area of 79.44 in<sup>2</sup> (middle), XLD single probe with a flow area of 2.01 in<sup>2</sup> (right).

### 3.2 Pressure Sensors

A pressure transducer converts a pressure change into a mechanical deformation that is transformed later into an electrical signal by a sensing element. The mechanical deformation of the transducer caused by pressure can be detected in several ways: capacitive detection (capacitance sensors), piezoresistive detection (strain pressure sensors), piezoelectric detection (quartz pressure sensors) (Figure 3.3) (Fundamentals of Formation Testing, 2006).

A capacitance sensor contains a variable gap capacitor where the sensing element is formed by two metallic or quartz plates. When external pressure increases, the deflection of the sensing plate creates a change in the capacitance related to the pressure applied. A strain pressure sensor consists of a tube with a strain wire wrapped around it. The exerted pressure on the tube initiates the strain wire to stretch and induces a change in electrical resistance. A quartz pressure sensor has a natural frequency of vibration like a tuning fork. When the quartz crystal vibrates in relation to a pressure-induced stress, a precise, and detectable sine wave frequency is created. The strain and quartz pressure gauges from Schlumberger Oilfield Services have gauge resolutions of 0.1 psi and 0.01 psi within



10000 psi range, respectively (MDT Modular Formation Dynamics Tester, 2005). Gauge resolution is defined as the minimum significant pressure change that a gauge can detect.

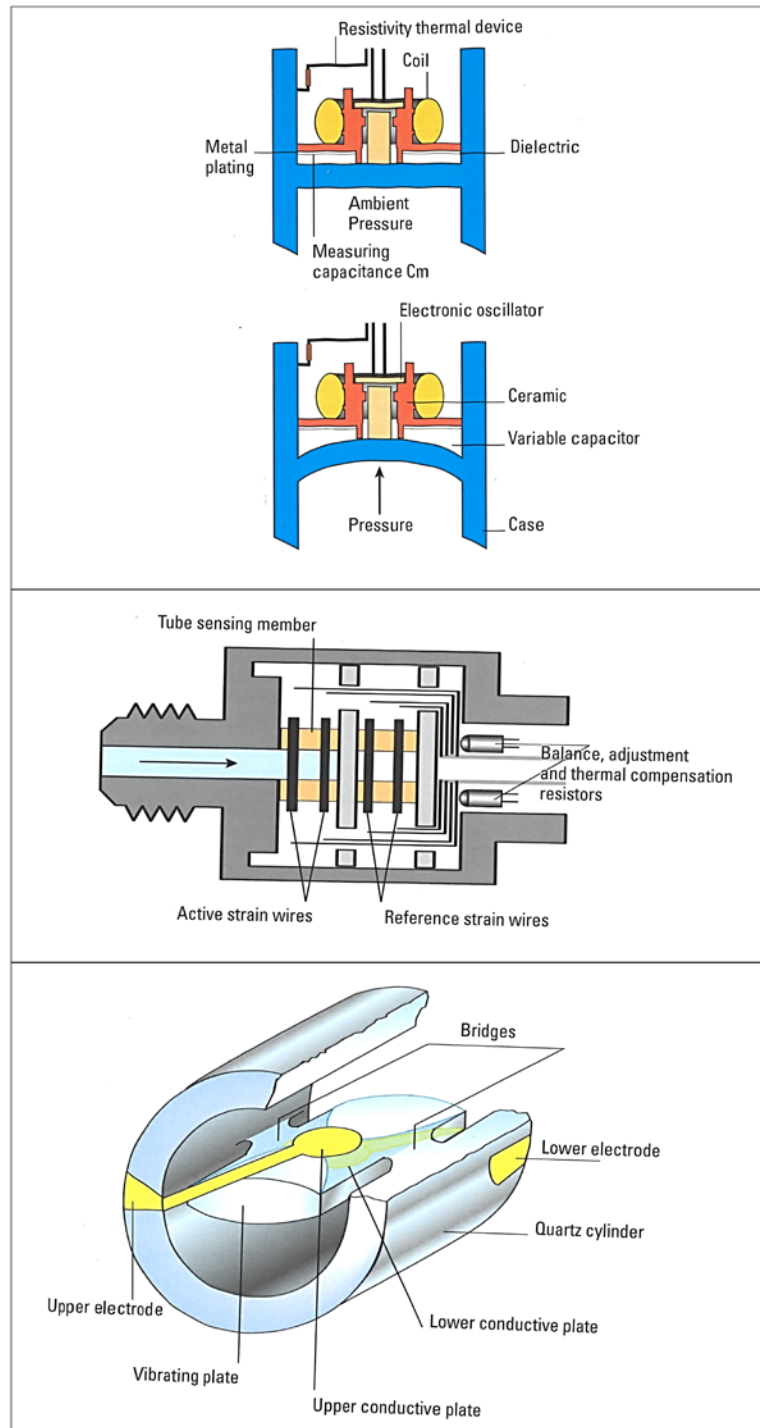


Figure 3.3: Capacitance pressure sensor (top), bonded wire strain pressure sensor (middle), crystal quartz gauge pressure sensor (bottom) (Fundamentals of Formation Testing, 2006).

### 3.3 Pressure Measurement

When an inlet is set on the sandface, it isolates the wellbore and creates a communication with the reservoir. A formation pressure measurement, called a pretest, is conducted by drawing a small amount of fluid to create a pressure drawdown, which is followed by a pressure buildup to obtain the formation pressure (Figure 3.4). A pretest does not require a volume of more than 20-cc with a single probe and a couple of liters with a 3DRP or a DP inlet. A pretest also provides a mobility ( $k/\mu$ ) value, which is an indication of permeability expected in the formation. The mobility may not be converted directly to the permeability due to its small depth of investigation, effects of relative permeabilities and capillary pressures, fluid viscosities and the skin factor introduced by the invasion and the inlet geometry.

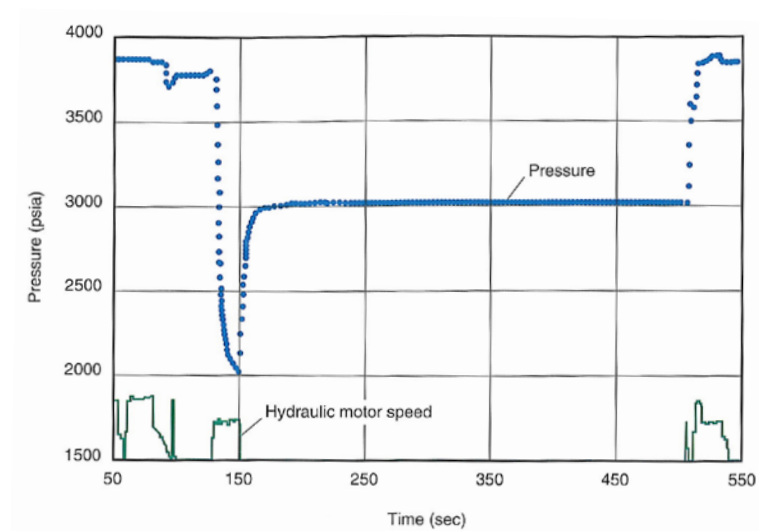


Figure 3.4: A single-probe pretest measurement (Wireline Formation Testing and Sampling, 1996).

A pressure transient data can be recorded with a preferred inlet for a longer duration. Generally a period of cleanup for sampling is used for a pressure drawdown and followed by sampling and a pressure buildup. This operation is referred to as Mini-DST. The pressure transient data is analyzed for the horizontal and vertical permeabilities, and the skin factor. In some occasions two inlets can be set during the entire WFT logging. The advantage of this is to observe the pressure interference between the zones where the inlets are set. The analysis of the interference can yield the barriers between the zones, or acquire the vertical and horizontal permeabilities due to the pressure transient between the zones if no barriers are observed. This operation is called as interval pressure

transient test (IPTT) or vertical interference test (VIT) as shown in Figure 3.5 (Jackson *et al.*, 2003).

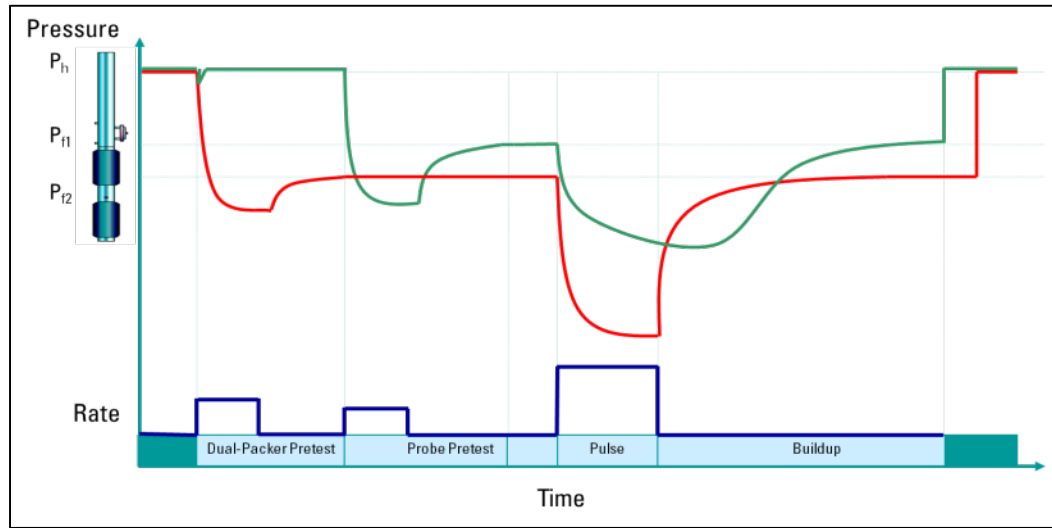


Figure 3.5: A sketch of pump rates and pressures of a dual-packer (red) and a single-probe (green) inlets during an IPTT operation. The dual-packer is the pulsing module and the single-probe is the observing module.

### 3.4 Fluid Analyzer Measurement

A fluid analyzer measurement is based mainly on the near-infrared (NIR) spectroscopy and differentiates between water and hydrocarbon with the absorption spectra (optical density vs. wavelength). Figure 3.6 shows the absorption spectra highlighting water and hydrocarbon peaks (top) and focusing on the hydrocarbon peak for its components and  $\text{CO}_2$  (bottom). Figure 3.6 shows that a sufficiently distinctive hydrocarbon characteristic is available to conduct an analysis for the quantitative hydrocarbon composition in terms of lumped components of  $\text{C}_1$ ,  $\text{C}_2$ ,  $\text{C}_3\text{-C}_5$ ,  $\text{C}_6+$ , water fraction, and  $\text{CO}_2$  in an OBM or WBM environment. GOR, CGR, and water-cut are also calculated from the spectrometric analyses during the cleanup (Mullins *et al.*, 2001; Dong *et al.*, 2007). The spectrometric measurement is calibrated for the detection and analysis of hydrocarbon, color for relative asphaltene content, and  $\text{CO}_2$  in crude oil and natural gas, as well as determination of water content and its pH. The fluid analyzer integrates auxiliary sensors including fluorescent measurements for a retrograde dew detection, a pressure and temperature gauge, a resistivity sensor, and a density and viscosity sensor.

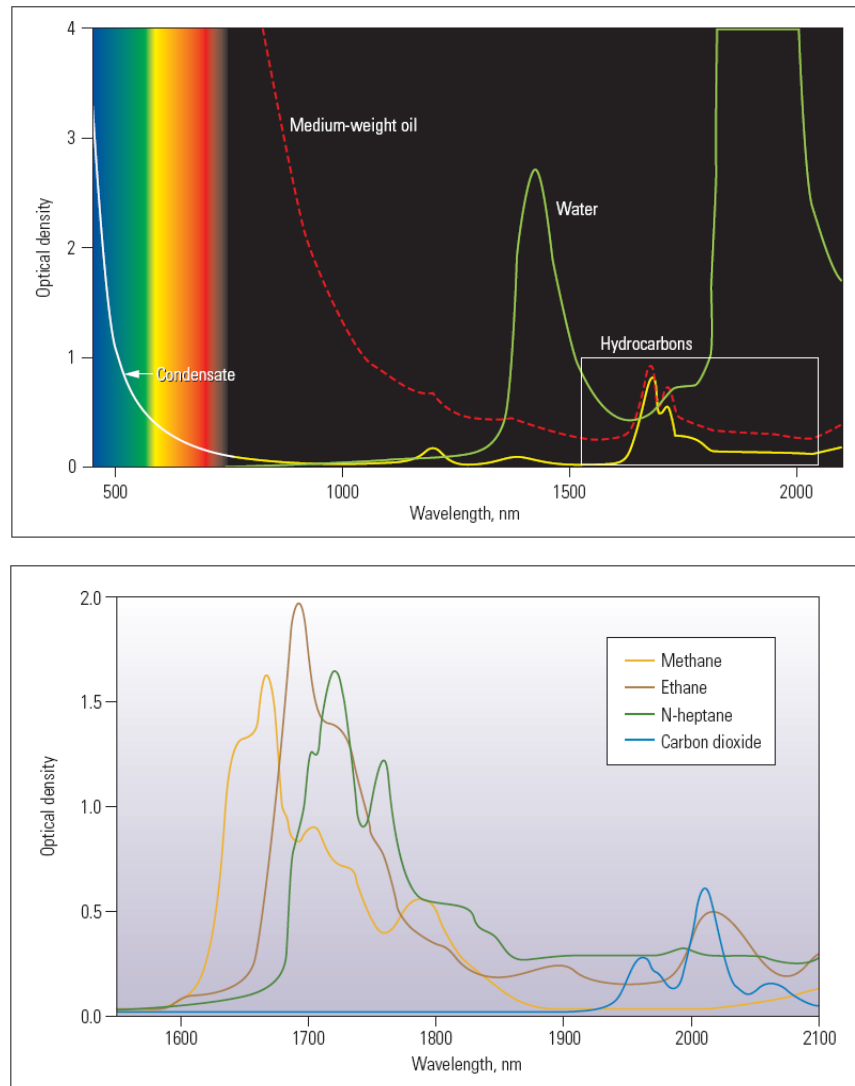


Figure 3.6: Absorption spectra displaying signatures of water and different types of hydrocarbon (top). Absorption spectra focusing on the hydrocarbon peak for its components and CO<sub>2</sub> (bottom).

### 3.5 Cleanup and Sampling

A cleanup procedure starts usually after a pretest. After the formation pressure is established, the pump module is turned on to flow the fluid from the reservoir into the wellbore. The pump rate can be adjusted to achieve the pressure drawdown desired. The fluid analyzer starts monitoring the fluid flowing from the reservoir into the WFT tool. In the case of hydrocarbon sampling in WBM, initially 100% mud filtrate flows for a period of time, later a hydrocarbon breakthrough occurs, and then the cleanup reduces the water-cut. Typically the desired level of cleanup is achieved when the water-cut measured is less than or around 10%. The formation fluid samples can be collected by diverting the fluid into the PVT-quality bottles carried on the WFT string.

Figure 3.7 shows a WFT station including a cleanup and an IPTT test periods. The sequence contains the pretests of the dual-packer and the single-probe inlets, and it follows the DP inlet drawdown, and finally the pressure buildup. The flowing DP inlet is located 9.8 ft deeper than the observer SP inlet in this example. The pressure drawdown is created by a pumpout from the DP inlet. The measurements of water-cut, pump rate, hydrocarbon composition, pressures of the DP and SP inlets are continuously recorded along with other auxiliary measurements.

The recorded pressure and water-cut measurements are later used in an inversion process to generate multiphase flow properties. These two measurements during the cleanup are relatively independent, and their radius of influence in the reservoir is different and depends on the reservoir properties, such as horizontal and vertical permeabilities, porosities, fluid compressibilities and viscosities, pressure drawdowns created by pump rates. The measured pressure and water-cut are connected to each other due to the multiphase skin, relative permeability, capillary pressure and water-cut development of the mud-filtrate invasion. The pressure pulse travels tens of feet while the oil movement reaches several feet into the reservoir. The mud-filtrate invasion can be a couple of feet in the reservoir (see Figure C.23 in the field example in Appendix C). The pressure buildups provide the average horizontal and vertical permeabilities during the IPTT test in the flow unit while openhole logs, either with porosity-permeability correlations or NMR measurements, present detailed distribution of the reservoir properties. This step is crucial since knowing vertical and horizontal permeabilities along with other reservoir properties will establish thorough responses of oil and water velocities, and pressure transients in the near wellbore region in a heterogeneous formation.

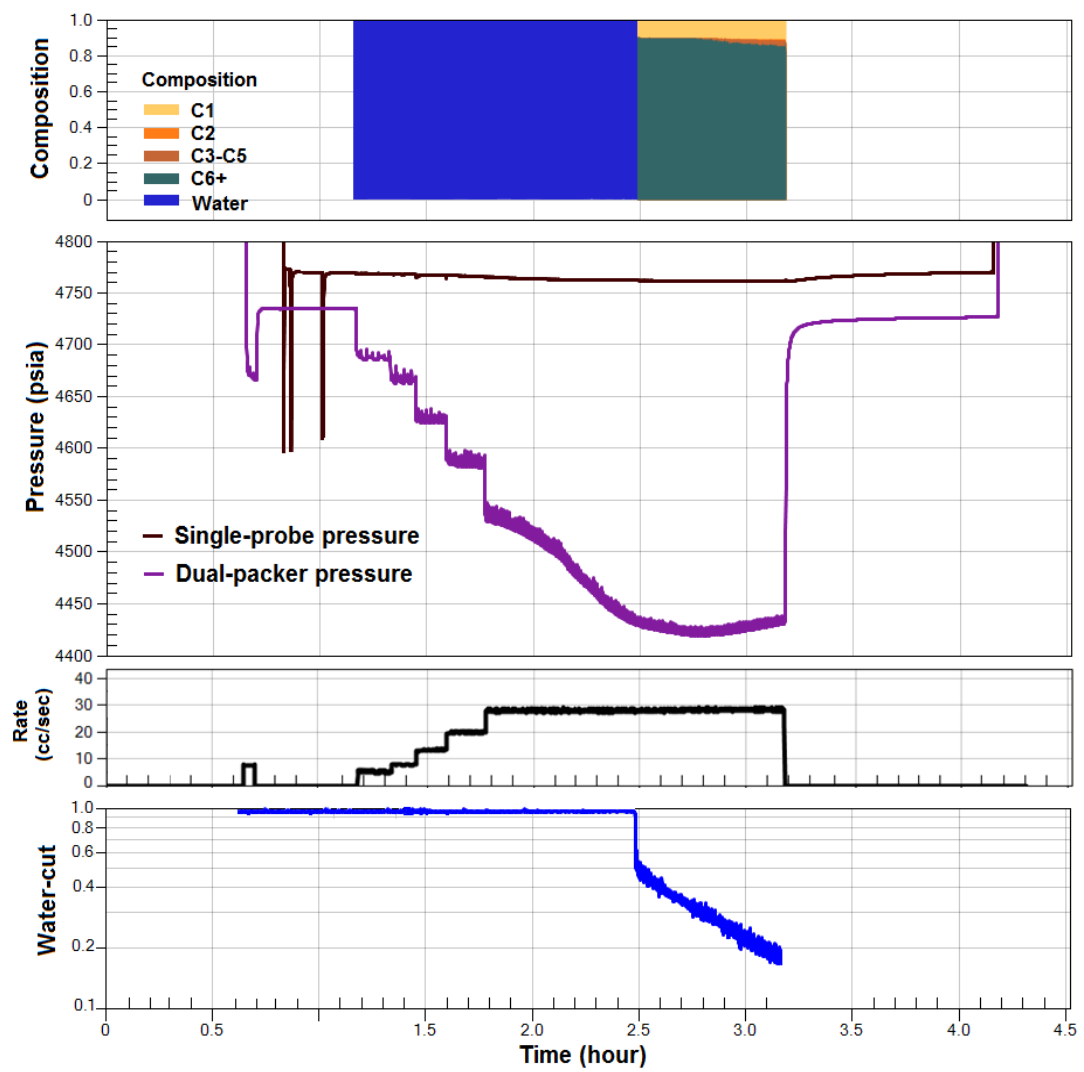


Figure 3.7: WFT measurements during the periods of pretesting, cleanup and IPTT test.

## CHAPTER 4. NUMERICAL MODEL

In this chapter we have set up a synthetic numerical model in order to investigate the effects of formation and fluid properties, WFT inlets and tool geometry, numerical modeling features, and processes taking place during drilling and logging. The sensitivities of the forward numerical runs have assisted in improving the model before implementing it in field cases.

The synthetic forward model prepared includes the WFT DP inlet and flowlines. The model consists of a partially completed single well close to the top of the formation. The wellbore is invaded with the mud filtrate from its entire openhole section, but the DP inlet isolates its own interval during the cleanup and the model acts like a partially completed well. Outer, top and bottom boundaries of the model have no flow. The outer boundary is sufficiently far away so that the pressure transient response does not experience any boundary effects. The model does not have a fluid transition zone since the oil-water contact (OWC) is assumed deeper than the reservoir, hence the numerical model initiates water and oil saturations at  $S_{wi}$  and  $(1-S_{wi})$  respectively.

A mud-filtrate invasion comprising dynamic and static filtration periods occurs with a constant-flux analytical aquifer at the sandface of the wellbore for the entire reservoir unit. The dynamic filtration is 0.5 day. After the drilling is completed, openhole logs and other operations took 3.5 days, it is followed by a WFT cleanup. The static filtration starts after the dynamic filtration and continues with a constant influx rate during the WFT cleanup and buildup periods (Figure 4.1). However the static filtration stops only across the sealing element of the inlet during the WFT operation. The cleanup and buildup periods are chosen similar to common field cases as six hours and two hours in this order. Although the DP inlet is used throughout the exercise in this chapter, the gridding designs of SP and 3DRP inlets are described in the following sections as a reference.

The relative permeability and capillary pressure curves used in the model are displayed in Figure 4.2. Unless stated otherwise, it is assumed that a single set of relative permeability and capillary pressure curves is representative of the mud-filtrate invasion and cleanup events in our study. Properties of the forward numerical model are presented in Table 4.1 to 4.4.

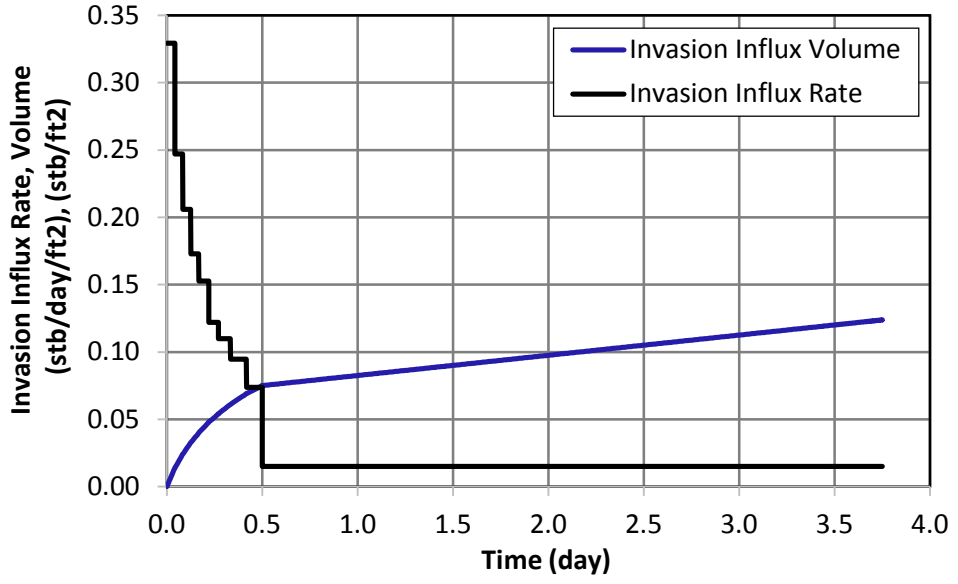


Figure 4.1: Mud-filtrate Invasion design illustrating dynamic (before 0.5 day) and static (after 0.5 day) filtration periods of the synthetic numerical model.

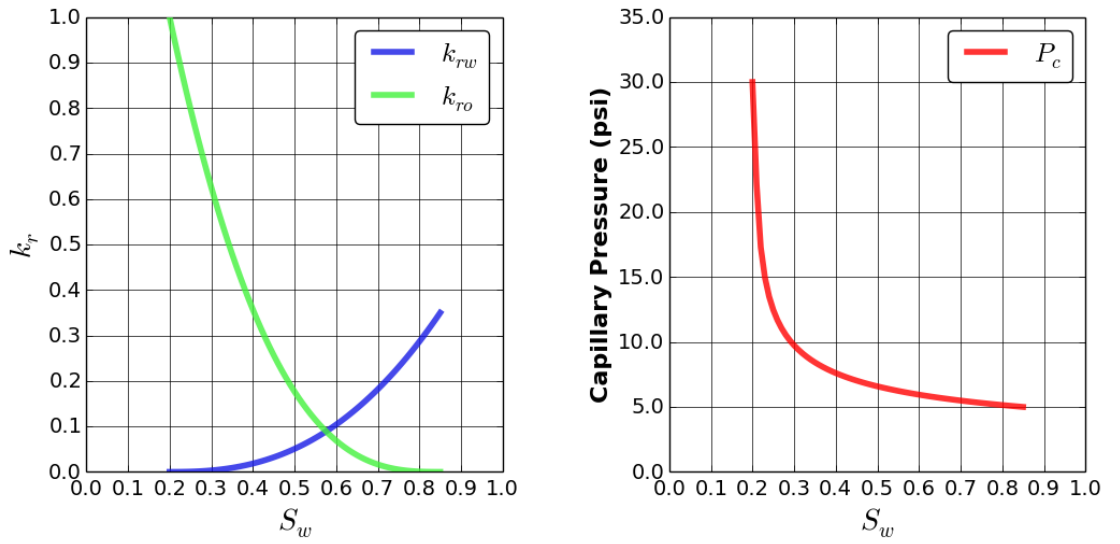


Figure 4.2: Relative permeability and capillary pressure curves of the synthetic numerical model assumed for both mud-filtrate invasion and WFT cleanup measurements.



Table 4.1: Invasion, cleanup and buildup parameters. The cleanup rate is for the circular grid and the radius of invasion is an average value at the end of the dynamic filtration.

Properties	Input	Unit
Dynamic filtration duration, $dynt$	0.5	day
Static invasion influx rate, $statq$	0.0150	stb/day/ft <sup>2</sup>
Cleanup start time	3.5	day
Cleanup duration, $t_{cleanup}$	6	hr
Cleanup rate, $q_{cleanup}$	53	L/hr
Pressure buildup duration, $t_{PBU}$	2	hr

Table 4.2: Reservoir properties of the synthetic numerical model.

Properties	Input	Unit
$h$	53.00	ft
$h_w$	3.333	ft
$z_w$	47.55	ft
$r_w$	0.354	ft
$R$	816	ft
$k_h$	20.00	md
$k_v/k_h$	0.60	
$Skin$	2.00	
$c_r$	1.25e-6	psi <sup>-1</sup>
$P_i$	3403.6	psia
$\phi$	0.30	fraction
$S_{wi}$	0.20	fraction
$S_{or}$	0.15	fraction
$n_w$	2.50	
$no$	2.80	

Table 4.3: Fluid properties of the synthetic numerical model. The fluid viscosities and densities are at downhole and surface conditions respectively.

Properties	Input	Unit
$\mu_o$	0.75	cP
$\mu_w$	0.55	cP
$c_o$	10.24e-6	psi <sup>-1</sup>
$c_w$	3.00e-6	psi <sup>-1</sup>
$\rho_o$	0.865	g/cc
$\rho_w$	1.153	g/cc

Table 4.4: Grid properties of the synthetic numerical model.

Properties	Count
Cell	71496
DR	216
DØ	1
DZ	331

## 4.1 Gridding

Radial gridding is used for DP, SP, and 3DRP inlets. The gridding differs for each inlet due to the inlet geometry as detailed in the following sections. A commercial black-oil simulator is used in the numerical model (ECLIPSE Reservoir Simulator Technical Description, 2015).

### 4.1.1 Dual-Packer Modeling

The DP inlet is modeled with a 2D R-Z radial grid due to the full circumferential opening of its interval. The multisegment well model is applied, and it properly accounts for the multiphase flow and the segregation in the internal storage volume between the packers. The model has a constant cell size of 0.25 cm for the inner 174 radial grid cells in order to capture near-wellbore events in detail since the largest pressure drops, the fastest fluid velocities, the mud-filtrate invasion, the skin effect due to flow restrictions, damage and multiphase flow occur in the near wellbore region. Beyond these inner cells, the grid grows geometrically to the boundary with a factor of 1.3. The distance between the wellbore and the outer boundary is 816 ft. The azimuthal grid increment is set to 90 degrees and the rates are reduced accordingly to one-fourth of the actual. The height of the grid cells is 0.5 cm across the open DP interval. Away from the inlet, the height of grid cells grows geometrically toward upper and lower boundaries with a factor of 1.15 (Figure 4.3).

Sensitivity analyses are conducted over the gridding and timestep intervals. The sensitivity analyses are detailed on the size of the inner radial cells and the height of the cells across the DP inlet. This is a rather important stage because it assists to reduce the run time without compromising the data quality. It is shown that the distribution of relatively larger inner radial grid cell sizes makes oil breakthrough earlier and decreasing the size makes oil breakthrough later. The increased inner radial grid size has also a larger pressure drawdown. The effect is minimized with a radial grid size of 0.25 cm. The grid size smaller than 0.25 cm increases radial grid counts with an additional computational time. Therefore, the inner radial grid is chosen as 0.25 cm. Figure 4.4 shows the bottomhole pressure and water-cut during the cleanup with different innermost radial grid sizes and keeping the height of the grid cells as 0.5 cm across the DP inlet.

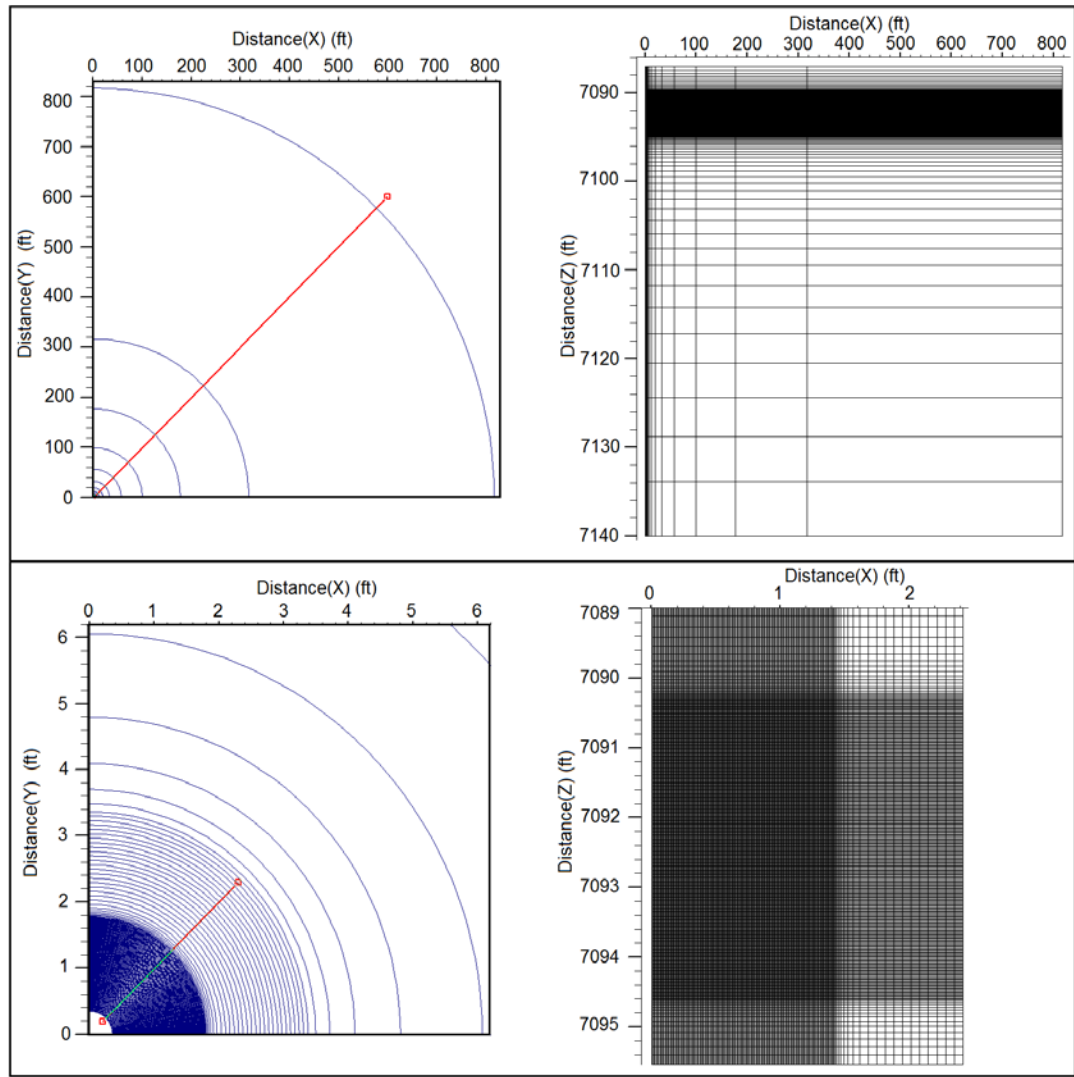


Figure 4.3: Radial gridding of the model is displayed in several sections. The top left and the top right graphs depict the top and the cross-sectional views of the entire model respectively. The bottom left and the bottom right graphs show the near wellbore region from the top and the cross-sectional zone where the DP inlet is set respectively. The red lines on the left show the absolute locations of the cross sections displayed on the right.

Figure 4.5 uses the innermost radial grid size of 0.25 cm, and the height of the grid cells across the DP inlet is altered from 0.25 cm to 5 cm. Vertical gridding affects the bottomhole pressure and water-cut calculations when the height of the grid cells across the DP inlet is greater than or equal to 5 cm in this synthetic homogenous reservoir. Since the innermost radial grid cell size of 0.25 cm is chosen as the optimum, the height of the grid cells across the DP inlet is not suggested to be larger than the innermost radial grid cell in order not to distort the flow pattern occurring near the wellbore during the cleanup. Therefore, the height of the grid cells across the DP inlet is also set to 0.25 cm for the further studies. This is particularly critical to have a finer scale representation of

heterogeneous reservoirs in field examples. The multisegment well model is not used for the DP inlet in Figure 4.5. Figure 4.10 later compares the same case with and without the multisegment well mode in detail.

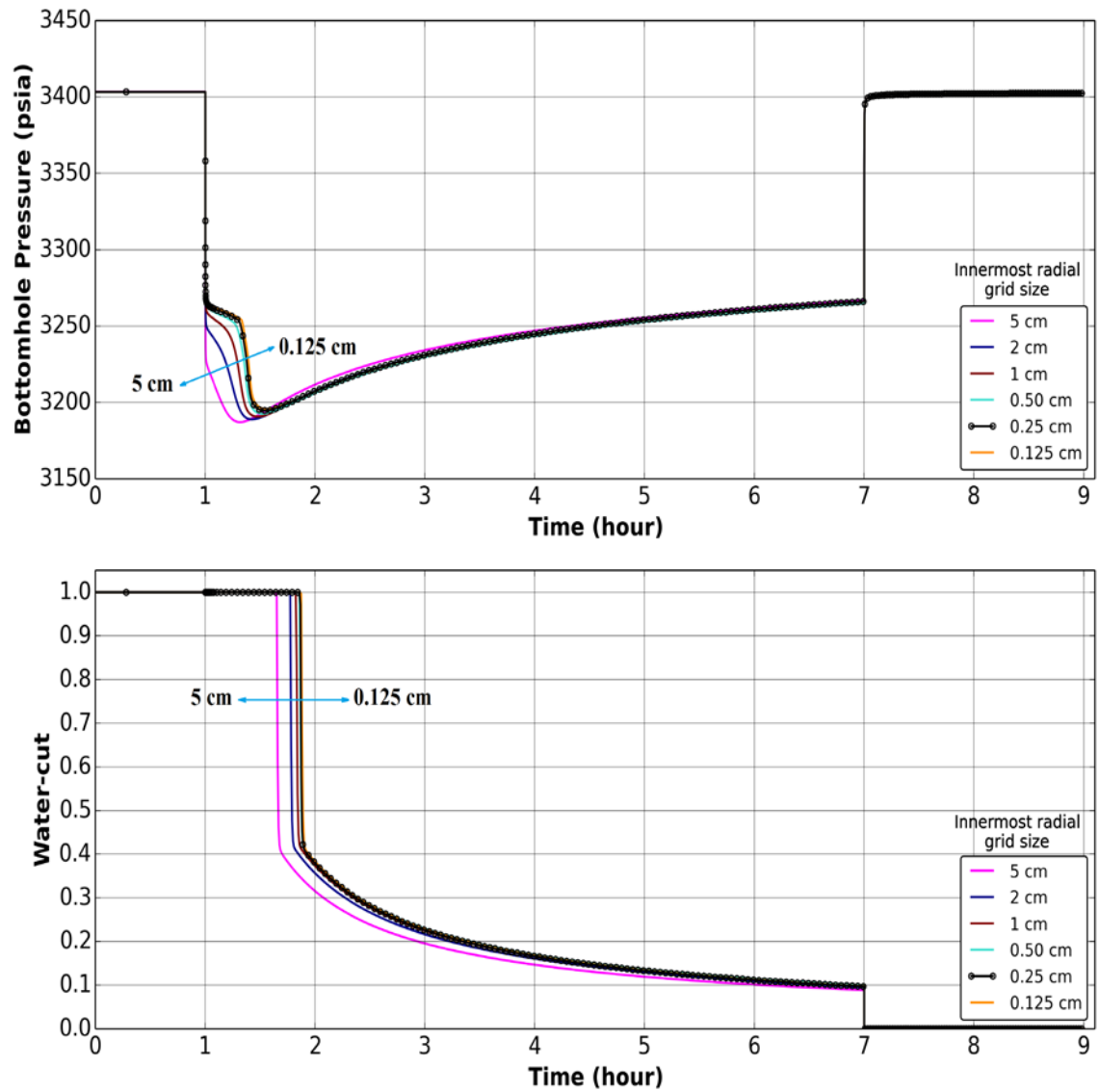


Figure 4.4: Base case runs with different innermost radial grid sizes having an impact on the pressure drawdown and the water-cut measurements during the cleanup process. The vertical grid size across the DP inlet is 0.5 cm. The multisegment well model is applied to the DP inlet.

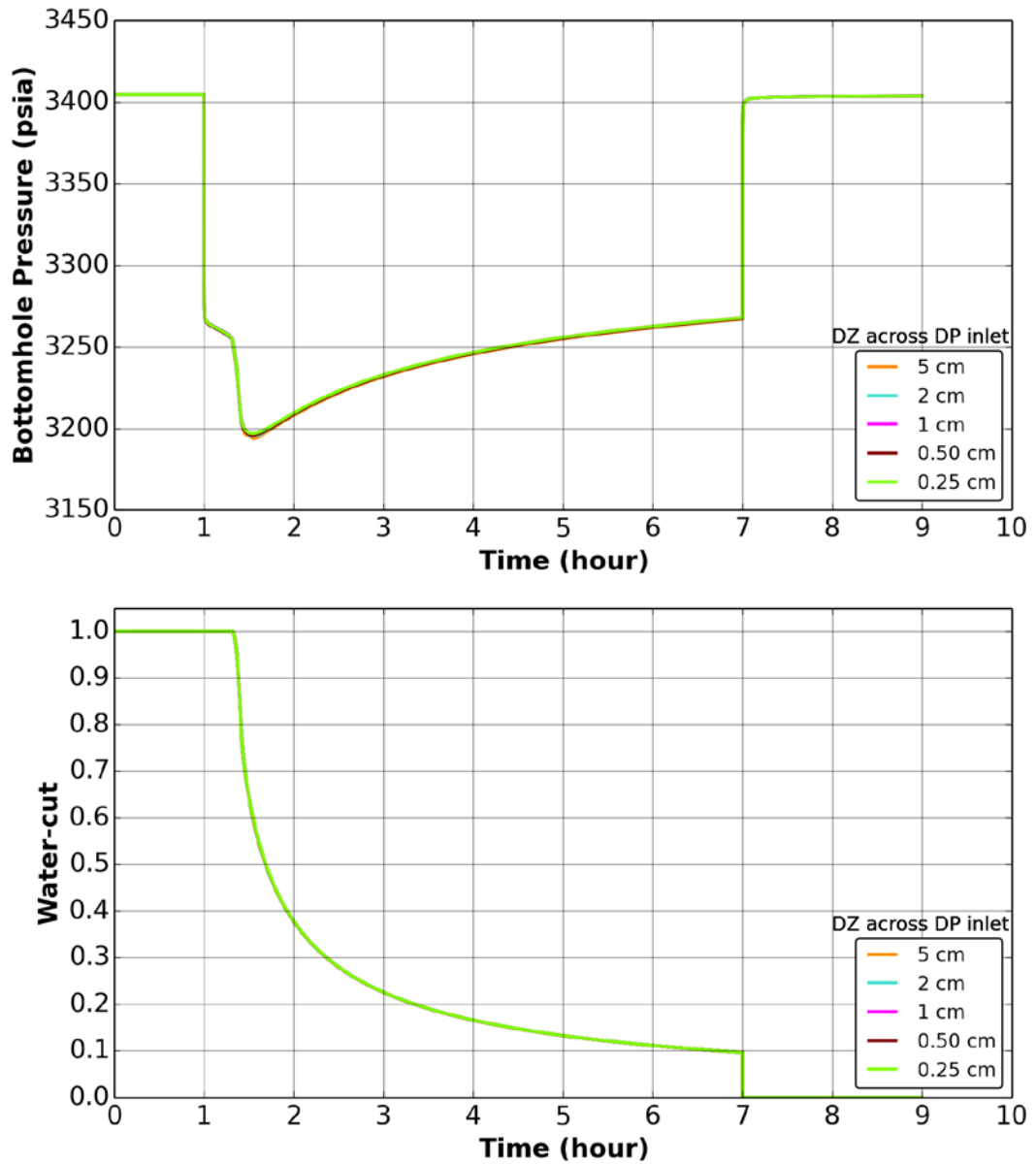


Figure 4.5: Base case runs with the innermost radial grid size of 0.25 cm. The vertical grid size across the DP inlet is modified. When the vertical grid height is less than 5 cm, the similar results are obtained. The multisegment well model is not applied to the DP inlet in this case.

#### 4.1.2 3D Radial Probe Modeling

The 3DRP inlet has four elongated inlets as shown in the middle picture of Figure 3.2. Figure 4.6 depicts a snapshot of the numerical model results of 3DRP inlet at the sandface. Figure 4.6 shows a model cross-section corresponding to the unfolded wellbore where the 3DRP inlet performs the mud-filtrate cleanup. Colors in the grid represent the fluid saturations. The 3DRP inlet geometry is radially gridded with fine grid increments so that drain shapes are honored and fluid fronts accurately captured. The model consists of a single well at the center of the radial grid. The well has open connections to the grid

corresponding to the shape of the 3DRP inlets. Prior to the cleanup, the mud-filtrate invasion is simulated by using a constant-flux analytical aquifer at the sandface for the entire reservoir unit. Outer, top and bottom boundaries of the model have no flow. The outer boundaries are sufficiently far away, such as 1500 ft or more so that no boundary effects are seen during the pressure transients. The inner radial grid cells have a constant cell size of 0.25 cm. Beyond the inner cells, the grid grows geometrically to the boundary. Azimuthally 45 degrees (a half of one inlet) of the full domain is modeled due to the symmetry of the problem, thus greatly reducing the number of cells. Accordingly, all rates in the model are reduced to one-eighth of the actual. The height of grid cells is 0.25 cm within the 3DRP inlet and grows geometrically upwards and downwards. The internal tool storage volume is much smaller in comparison to a DP interval so that the water-cut behavior during cleanup, as measured by the fluid analyzer, may be approximated to the sandface.

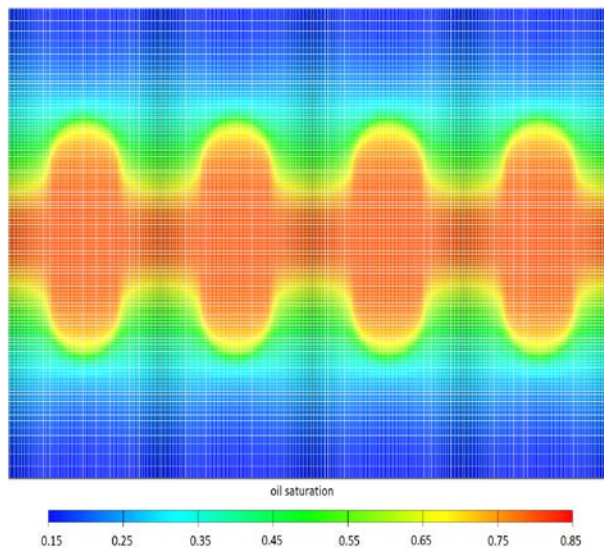


Figure 4.6: Numerical model results of 3DRP inlet at the sandface. The image of the unfolded wellbore is shown where 3DRP inlet performs the mud-filtrate cleanup. Colors in the grids represent the fluid saturations. Red color shows oil and blue color depicts WBM filtrate at the end of the cleanup period.

#### ***4.1.3 Single Probe Modeling***

SP inlets have relatively smaller flow areas in comparison to the DP and the 3DRP inlets. SP inlets are preferred in flow units where high permeabilities are observed or large pressure drawdowns are allowed during cleanups. The internal tool storage volume of an SP inlet is relatively small so that the water-cut behavior during a cleanup, as measured by the fluid analyzer, may be approximated to the sandface. The inner radial grid cells

for the invaded zone have a constant cell size of 0.25 cm. Beyond these inner cells, the grid grows geometrically to the boundary. Azimuthally 180 degrees (a half of the inlet) of the full domain is modeled due to the domain symmetry. All rates in the model are halved accordingly. The height of grid cells is around 0.20 cm within the SP inlet and grows geometrically upwards and downwards. The height of grid cells within the SP inlet is smaller in relation to its flow area (see Figure 3.2 for flow areas of the inlets). Figure 4.7 depicts the SP inlet gridding.

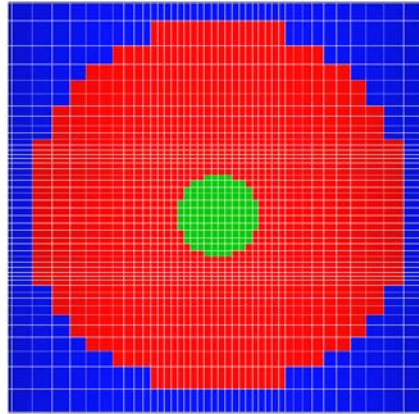


Figure 4.7: Cross-section ( $\theta$ -Z) of a numerical grid for a large-diameter (LD) single-probe. Green cells represent the flow area ( $0.85 \text{ in}^2$ ), red cells represent the sealing packer around the SP inlet, and blue cells are a part of the sandface.

## 4.2 Time Stepping

Results of various simulation timesteps are shown during the cleanup and the pressure buildup in Figure 4.8. The insets in the figure focus on the oil breakthrough and the early cleanup periods where larger changes of the water-cuts and the pressures occur during the cleanup. Relatively smaller timesteps are required to capture the changes in the periods presented in the insets of the figure. Timesteps of the mud-filtrate invasion are kept identical to have the same invasion profile before the cleanup. The timesteps in the figure represent the maximum allowed values for the particular run. The timestep starts with 0.1 second and grows with a factor less than two until reaching the maximum allowed value and continues with the value during the cleanup. The same is also applicable for the pressure buildup. The forward runs highlight that 60-second or less timesteps are reasonable to be able to shorten the run times for the same timestep growth factor. For example, the forward runs having 60-second and 10-second timesteps are completed in 195 seconds and 356 seconds, respectively.

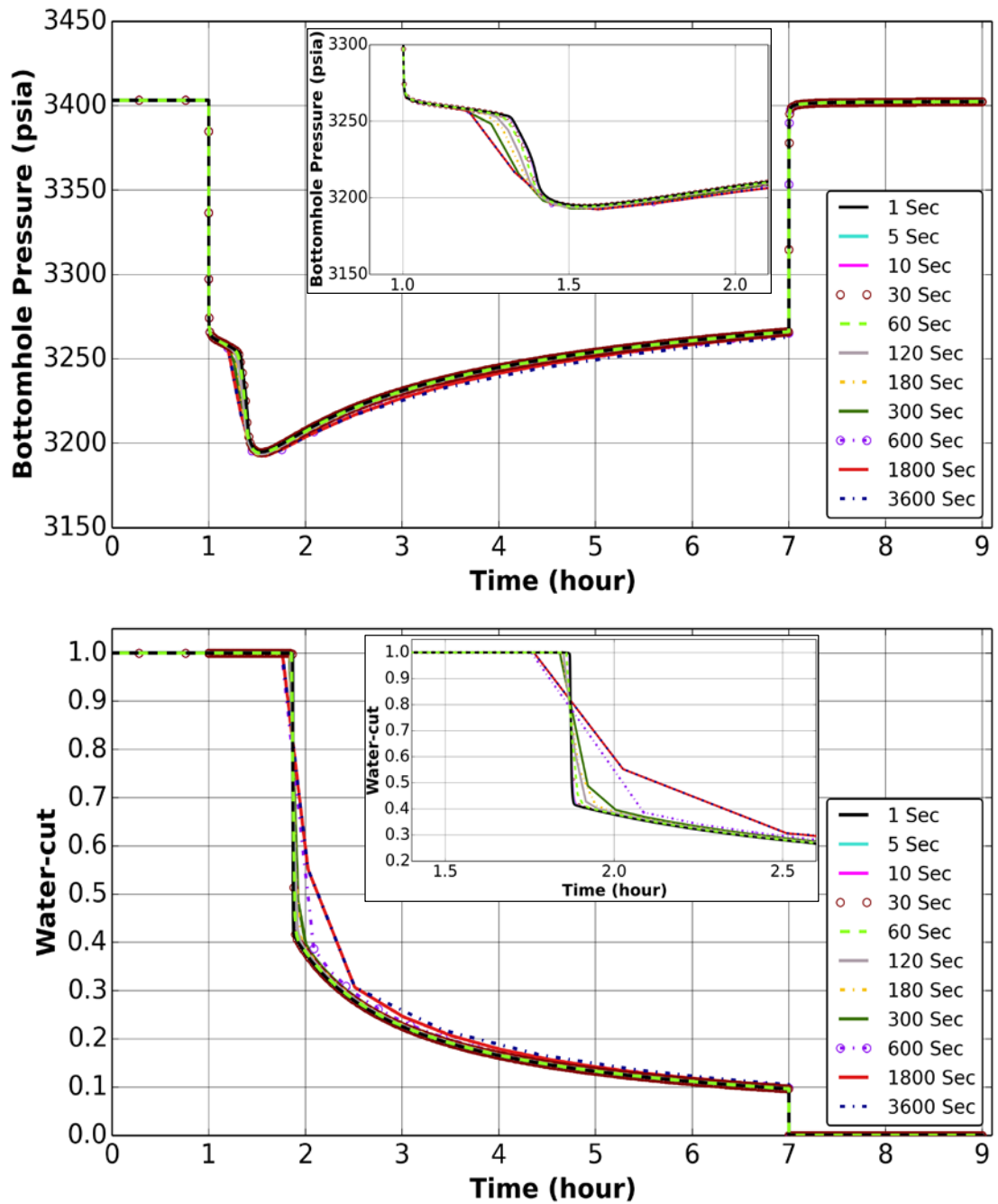


Figure 4.8: Responses of the bottomhole pressures (above) and the water-cuts (below) are shown for the runs having various maximum allowed timesteps. The insets focus on the oil breakthrough and the early cleanup periods where larger changes occur.



### 4.3 Multisegment Well Model

The DP gridding model uses the multisegment well model based on the drift-flux flow model (Multisegment Well Model, ECLIPSE Reservoir Simulator Software Technical Description, 2015). The drift-flux flow model enables the fluid phases to flow with different velocities within the DP interval, and it is also capable of modeling counter-current flow, which allows the heavy and light phases to move in opposite directions when the overall flow velocity is small or the well is shut in (Shi *et al.*, 2003) (see Chapter 2.4 for the detailed model).

The behavior of the cleanup, when the DP inlet is used, shows a late arrival of hydrocarbon to the fluid analyzer, and then follows a sharp decrease in the water-cut. When hydrocarbon flows into the DP interval, it starts segregating and accumulating in the upper part of the DP interval due to the fluid density contrast. This delays the hydrocarbon arrival to the entry port close to the bottom inside the DP interval, as the lower part of the interval is still filled with the WBM filtrate. Over time, hydrocarbon keeps accumulating and moves downwards in the interval. The multisegment well model allows the entire segregation event and captures the correct volume of the fluids and delays hydrocarbon detection due to the storage volume between the sandface and the fluid analyzer.

Figure 4.9 shows the multisegment well model representation of the DP interval and its flowline. The implementation of the correct tool geometry generates a detailed behavior of the fluid movement from the reservoir into the tool where bottomhole pressures and water-cuts are measured. The segments from 7:1 to 15:2 represent the DP interval, which is open to a flow from its entire length of 3.333 ft. The node at the junction of 4:1 and 8:2 is the fluid intake into the tool, which is 1.09 ft from the bottom of the interval. The distance to the fluid intake from the top of the interval is approximately  $\frac{2}{3}$  of the length of the entire interval. The fluid analyzer for the water-cut measurement is located on the flowline at the node of 2:1. The bottomhole pressure is reported at the datum depth.

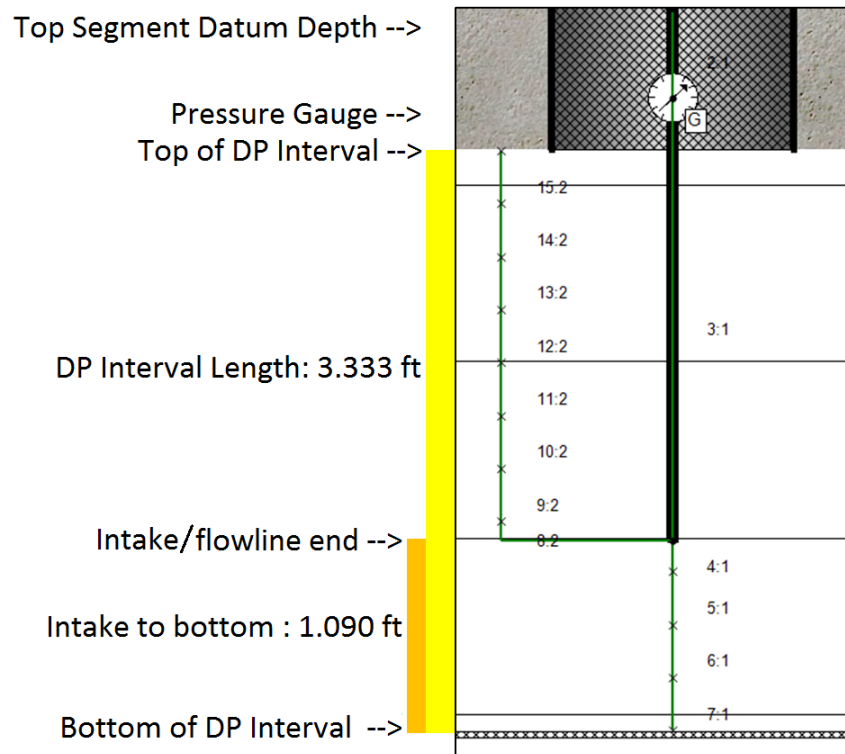


Figure 4.9: Completion schematic of the multisegment well model representing the DP interval with its dimensions.

Black-oil simulations comparing homogenous and multisegment flows are displayed in Figure 4.10. The homogenous flow represents the contamination measurement at the sandface while the multisegment flow with the correct WFT geometry represents the contamination level at the fluid analyzer. The sandface flow is depicted with the orange water-cut curve at the top plot in Figure 4.10. The sandface flow indicates that the water-cut is detected theoretically by a fluid analyzer at the sandface, which is not the case during a WFT DP cleanup. The curves of the sandface and the multisegment flows merge when hydrocarbon reaches to the DP flowline inlet approximately at 2/3 from the top of the DP interval. At this point, the produced concentration will equal the sandface concentration. Prior to reaching this point, hydrocarbon accumulates in the interval and only mud filtrate (water) flows as shown with the black water-cut curve at the top plot in Figure 4.10. Although the water-cut behavior is strongly affected by the segregation event in the interval volume, the bottomhole pressure measurements are very similar for both flow types as presented at the bottom plot in Figure 4.10. This is because the bottomhole pressure in both cases is measured at the same datum depth where the pressure gauge is located in the WFT tool.

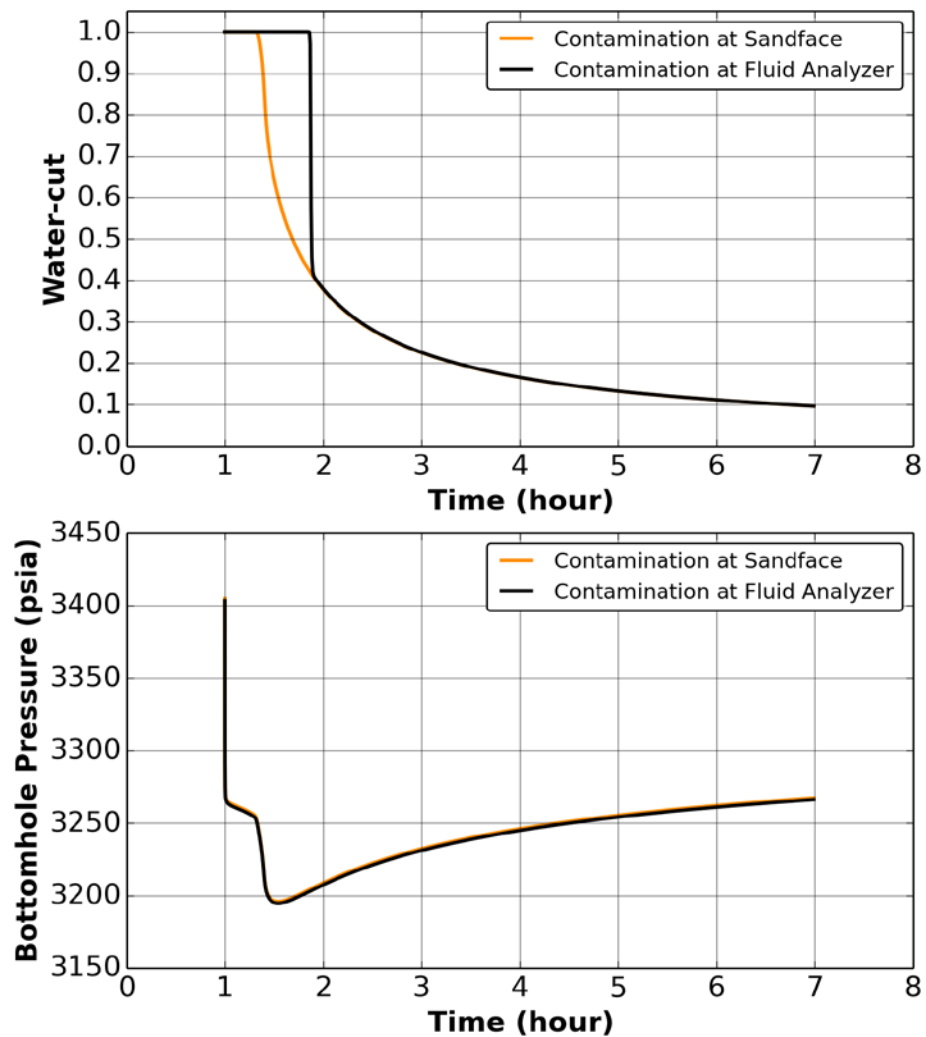


Figure 4.10: Water-cut (top) and bottomhole pressure (bottom) behaviors are displayed during the DP cleanup at the sandface and at the fluid analyzer.

Figure 4.11 presents a detailed comparison of the water-cut and pressure responses in 8.5 in hole. The DP interval contains a 17-liter interval storage at this hole size. Figure 4.11 compares the homogenous flow at the sandface, the homogenous flow with the DP interval storage, and the multisegment flow incorporating hydrostatic, friction and acceleration terms of a properly defined WFT DP inlet completion. Due to very slow flowing rates, friction and acceleration terms are negligible in the multisegment flow; hence the curves with the black line, and the blue and green symbols are identical. The multisegment flow incorporating slip velocities and fluid segregation accurately pictures the delayed arrival of hydrocarbon to the fluid analyzer, which measures the water-cut in the WFT tool. The homogenous flow, which has no segregation and slip calculations, represents the sandface measurements of the flow depicted with the orange curve in Figure 4.11. For the clarification, a homogenous flow with a 17-L wellbore storage is added as a brown curve into Figure 4.11. It shows that simply adding the wellbore storage

volume in a homogenous flow will not approximate a solution to the complex segregation and slip flow in the DP inlet.

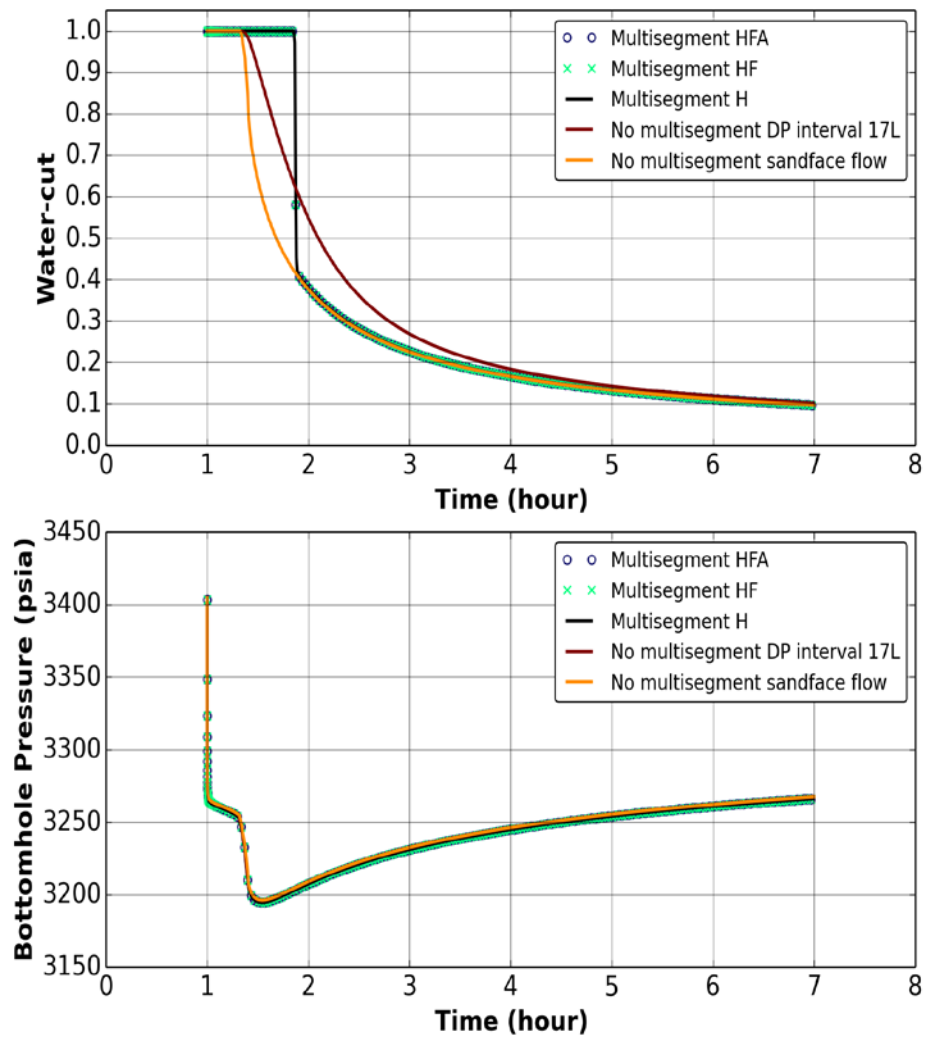


Figure 4.11: Comparisons of the DP inlet multiphase and homogenous flow options. The multiphase flow generates a segregated flow while the homogenous flow uses an average density of the phases in the inlet storage. H, F, A are hydrostatic, friction, and acceleration terms, respectively and their combinations can be used in the multisegment flow runs.

The multiphase flow model may be simplified in an analytical model: A complete segregation of the fluid phases is assumed in the DP interval for an immiscible contamination while the hydrocarbon is above the water due to their density differences. When the volume of the hydrocarbon in the DP interval reaches approximately  $2/3$  of the interval volume, the produced concentration will equal the sandface concentration as explained earlier. Prior to that, only WBM filtrate is produced. Below is the logic of the analytical approximation of the multiphase flow model:

$$V_o^{n+1} = V^n + \Delta t^n q^n (1 - C_{sf}^n), \quad V_o(t_o) = 0 \quad (4.1)$$

$$\text{if } V_o^{n+1} \geq \frac{2}{3} V \quad (4.2)$$

$$C^{n+1} = C_{sf}^{n+1} \quad (4.3)$$

else

$$C^{n+1} = 1 \quad (4.4)$$

end

where  $C$  is water-cut at the fluid analyzer,  $C_{sf}$  is water-cut at the sandface,  $q$  is production rate,  $V$  is the DP interval volume,  $V_o$  is volume of hydrocarbon in the DP interval.

#### 4.4 Mud-Filtrate Invasion

The correct representation of the invasion profile is a crucial step for generation of the multiphase flow properties. In this synthetic example, the DF period takes 0.5 day and the SF period continues after that. Radial invasion profiles in relation to saturation and pressure are presented in the presence of the capillary pressure near the wellbore in Figure 4.12 and 4.13. It is important to note that the DF period displays a sharper shock front due to its bigger invasion rate, and the SF period smears the shock front because of the capillary pressure and its much smaller invasion rate.

Volumes and durations of the DF and SF periods are not exactly known. Volume estimates will be acquired from the depth of investigation analysis of a 1D or 2D resistivity and salinity inversion process or may come from drilling reports. The total invasion time is established from the timeline of drilling and WFT cleanup. It is also recognized that logging times play a crucial role for measurements in capillary pressure cases. The time gap between openhole and WFT logs will change the saturation distribution in the near-wellbore region due to the slow, but continuous invasion during the SF period. This saturation change depends on, other than the reservoir and fluid properties, the SF rate, the time gap before the WFT cleanup, and the capillary pressure. When the mud cake seals, the SF rate is relatively small, and the water saturation dissipates due to the capillary pressure around the wellbore as displayed in Figure 4.12

(also see Chapter 4.6.6). Figure 4.13 shows the oil pressure progress during the DF and SF periods. Figure 4.13 also presents the supercharged formation pressures during the DF period, and the supercharged pressures quickly dissipate to the near-initial pressure in the SF period. Figure 4.14 displays the difference of water and oil pressures due to the capillary pressure during the invasion. Figure 4.15 is similar to Figure 4.14 and shows the difference of the phase pressures as the capillary pressures during the invasion.

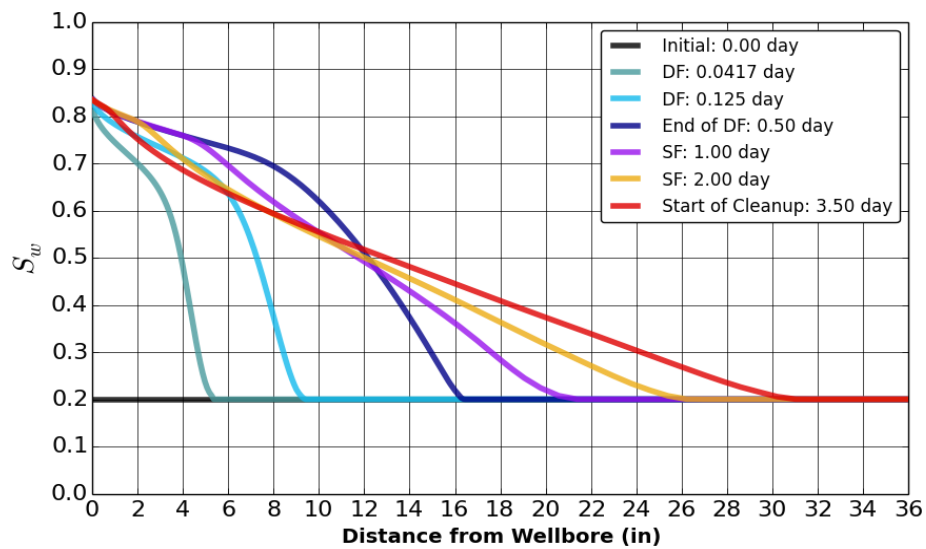


Figure 4.12: Water saturation progress during the WBM filtrate invasion in the near-wellbore region at the center of the DP interval in the presence of capillary pressure.

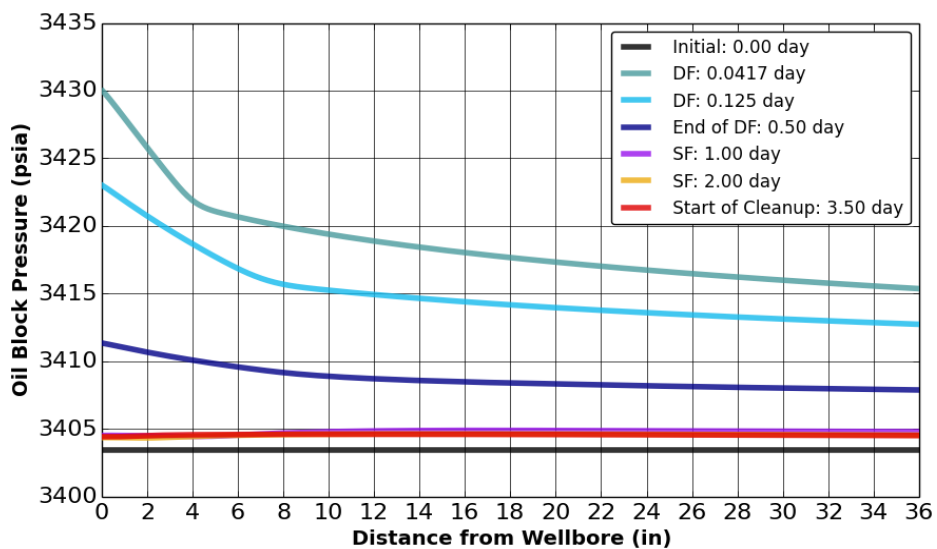


Figure 4.13: Oil pressure progress during the WBM filtrate invasion in the near-wellbore region at the center of the DP interval in the presence of capillary pressure.

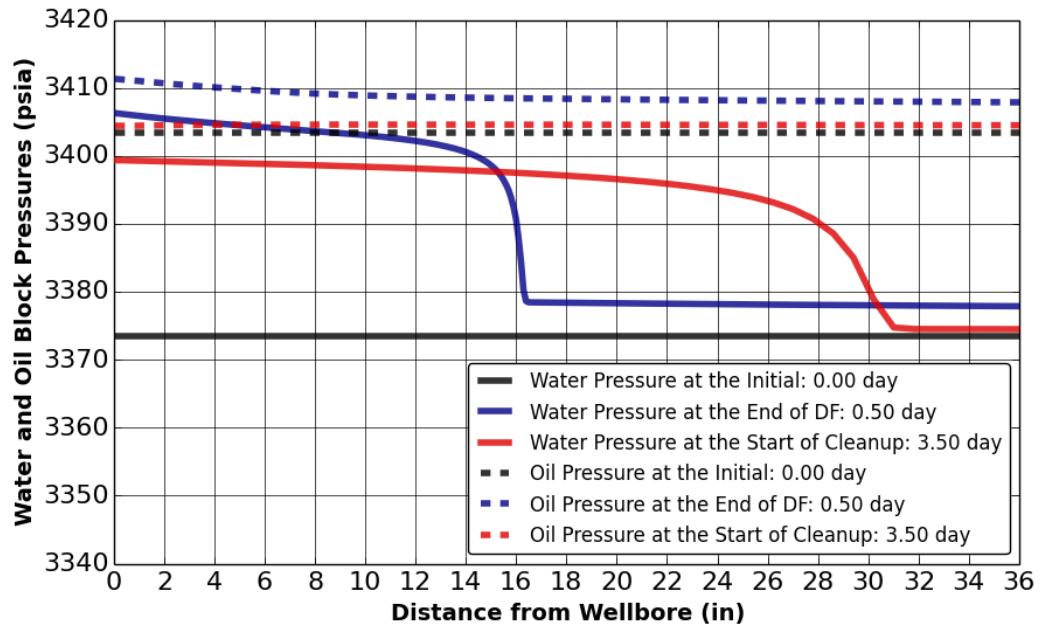


Figure 4.14: Water and oil block pressures during the progress of the WBM filtrate invasion in the near-wellbore region at the center of the DP interval in the presence of capillary pressure.

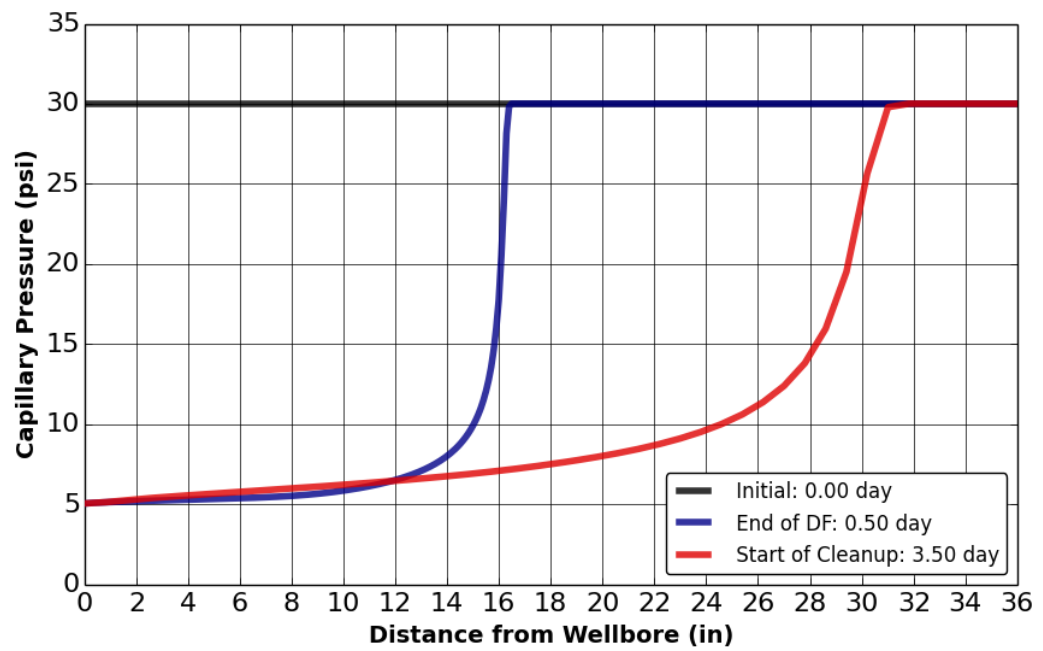


Figure 4.15: Capillary pressures during the progress of the WBM filtrate invasion in the near-wellbore region at the center of the DP interval.

## 4.5 Cleanup

The cleanup process increases the oil saturation in the vicinity of the near-wellbore region although SF still occurs. The cleanup, generally being several hours to reduce the contamination, may not bring the water saturation to the initial reservoir saturation condition (or it requires an extensive volume of pumpout to achieve that), but this is not a requirement since the water-cut level below or around 10% is sufficient for sampling.

The water-cut (represented at the top figure in black) in Figure 4.10 displays the cleanup progress with a constant rate of 8 bbl/day conducted until the water-cut reaches 10% just before the sampling. Figure 4.16 to 4.19 show the reservoir properties near the wellbore at the specific event times. Figure 4.17 shows the oil pressure change during the cleanup, and the following pressure buildup. Figure 4.18 shows the water and oil pressures during the same period in the presence of the capillary pressure. Figure 4.19 displays the capillary pressures during the DF, SF, cleanup and pressure buildup periods in the near-wellbore region at the center of the DP interval.

DF creates the majority of the mud-filtrate invasion into the reservoir while the formation pressure is increased representing a supercharged pressure (Figure 4.16 and 4.17) as explained earlier. When SF starts and the time delay occurs until WFT logging, the water saturation around the wellbore is redistributed. Meanwhile, the supercharged pressure due to DF is reduced, but still higher than the initial formation pressure in this example. It is also noticed that the capillary pressure effect from DF to SF periods increases as seen in Figure 4.19. The capillary pressure change is also visual in oil and water block pressures in Figure 4.18. The cleanup decreases the water saturation at the sandface to around 40% just before the sampling in this example, while the pre-invasion water saturation is 20%. Depending on the relative permeability and the capillary pressure at the cleanup saturation, the flowing pressure reduces, then increases slightly as presented in Figure 4.17. Figure 4.18 also represents the flowing oil and water block pressures affected by the capillary pressure, which is determined by the saturation profile at the particular timestep. Figure 4.20 illustrates the saturation profile at the end of the DP cleanup zooming to a height of 10.76 ft from the top, and to a distance of 32.73 ft into the reservoir from the wellbore. The saturation profile in Figure 4.20 represents a homogenous reservoir cleanup, which is more efficient horizontally due to  $k_v/k_h$  ratio creating relatively higher cleanup rates horizontally.



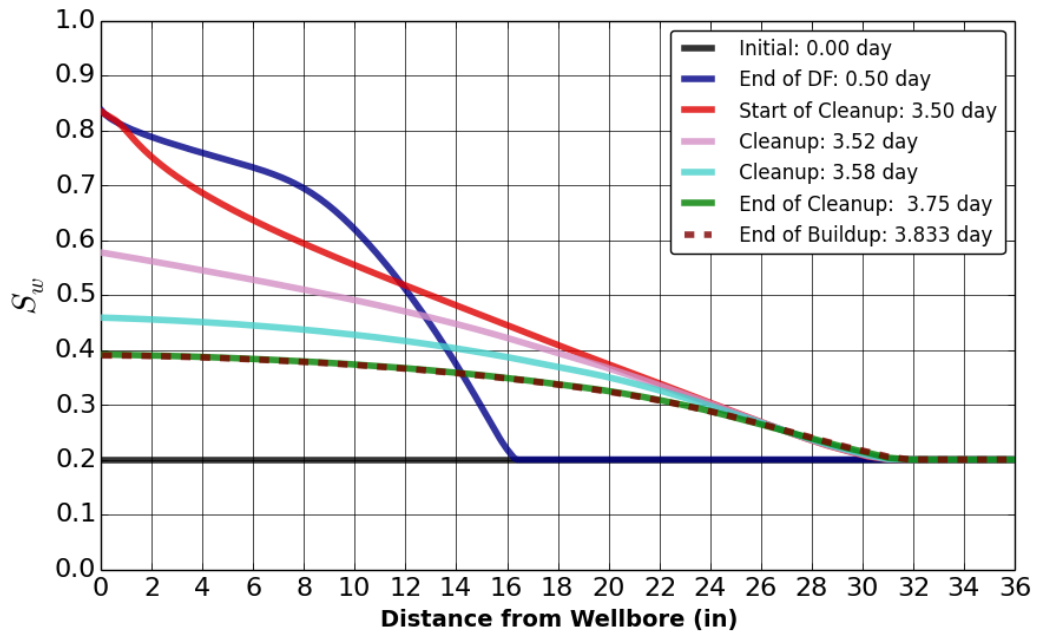


Figure 4.16: Water saturation profiles including the invasion, cleanup and pressure buildup events depicted in the near-wellbore region at the center of the DP interval in the presence of capillary pressure.

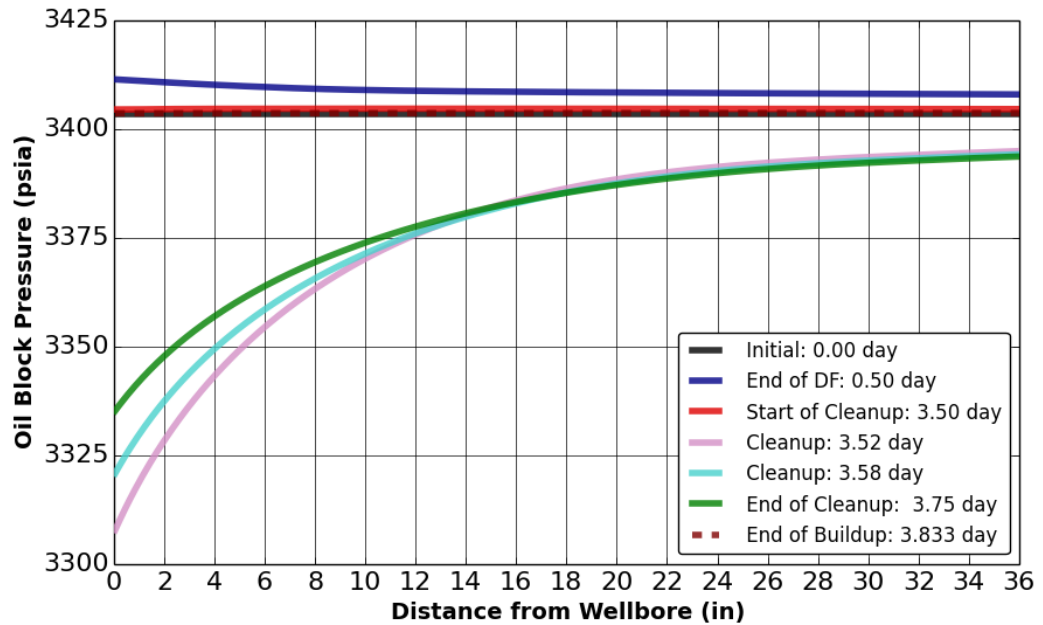


Figure 4.17: Pressure profiles including the invasion, cleanup and pressure buildup events illustrated in the near-wellbore region at the center of the DP interval in the presence of capillary pressure.

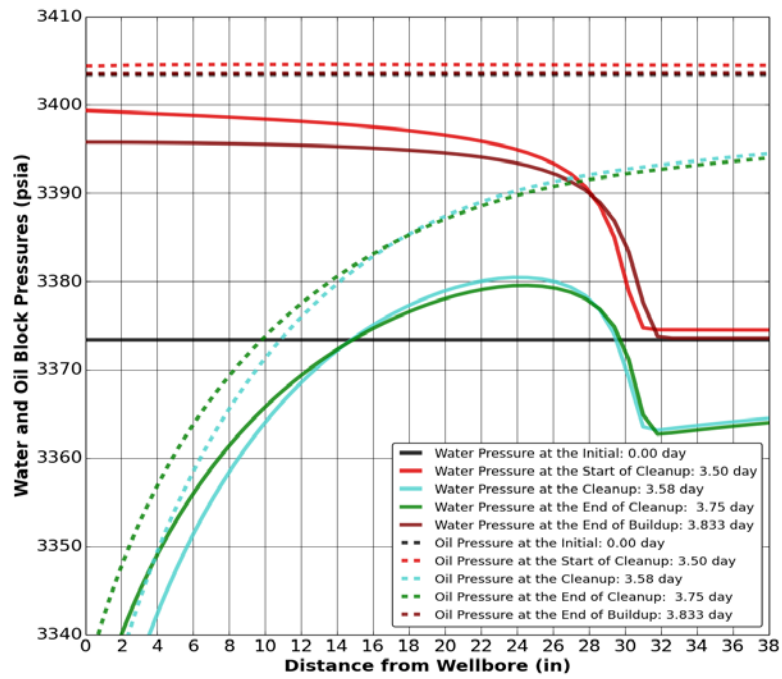


Figure 4.18: Water and oil block pressures during the progress of the cleanup in the near-wellbore region at the center of the DP interval in the presence of capillary pressure.

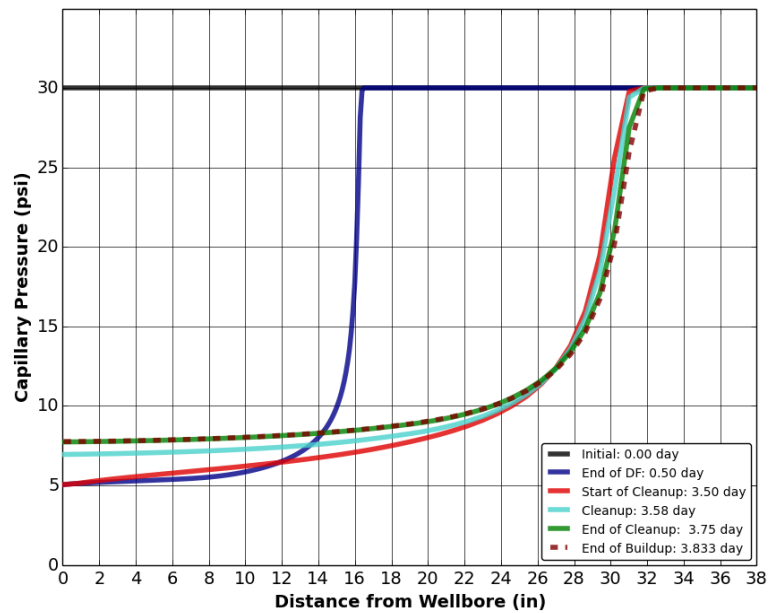


Figure 4.19: Capillary pressures during the progress of the DF, cleanup, and at the end of the pressure buildup in the near-wellbore region at the center of the DP interval.

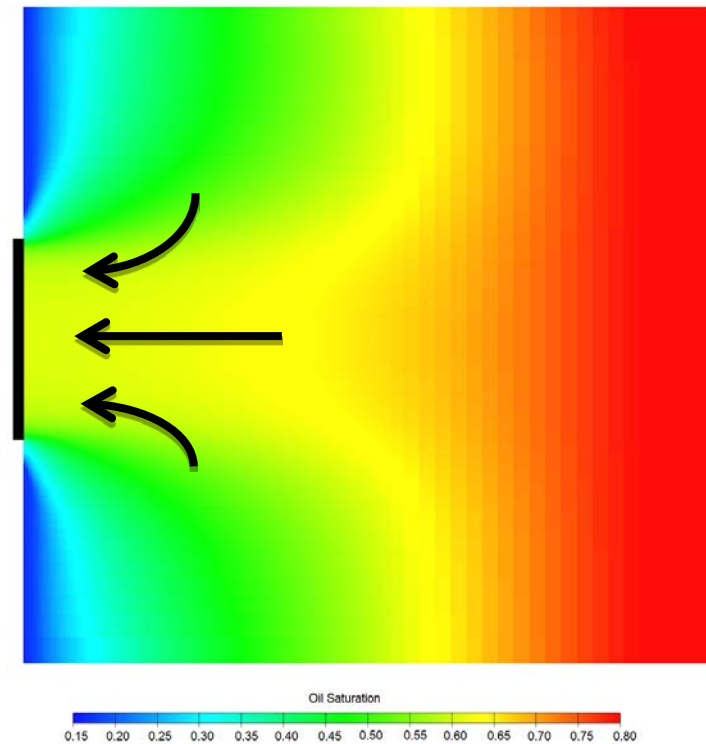


Figure 4.20: A radial-vertical (R-Z) cross-sectional view of the near wellbore region at the end of the DP cleanup. The DP is located at the center left (displayed as a black vertical line). The grid is zoomed to a height of 10.76 ft from the top, and to a distance of 32.73 ft into the reservoir from the wellbore. The arrows represent the cleanup direction.

The bottomhole pressure measured in the wellbore during the cleanup has a very distinguished shape shown as the connection pressure in red at the top plot in Figure 4.21. The bottomhole pressure drops sharply from the formation pressure in the early period. Then it reaches a near plateau followed by a further dip and finally increases gently. The behavior of the bottomhole pressure does not necessarily have the same trend for different cases when there are different fluid and rock properties, such as fluid viscosities, capillary pressures, relative permeabilities, heterogeneities, pumpout rate, damage skin, and so on. However, a detailed answer is provided to improve our confidence level in preparation of the numerical simulation process. It is important to note that the model has a capillary pressure implementation.

When the pressure pulse travels within the vicinity of the wellbore at the initial stage of cleanup, the water moves with its highest relative permeability and oil moves with its lowest behind the displacement front. Pressure and saturation profiles along the production interval are not uniform because of the partial completion (the DP interval) and relative permeability effects. Once oil arrives to the interval, it decreases connection

productivity, which depends on the total mobility, and the production is redistributed among other connections in the interval since the pumpout rate is constant. The cleanup progresses with decreasing water-cut and increasing oil relative permeability, which has an increasing effect over the total mobility. The WFT bottomhole pressure, which is calculated over the time with the changing total mobility, has the same trend as the connection pressures of the cells. The connection production rate of each phase at the reservoir conditions are calculated with Equation 2.18. The progress of the DP cleanup is explained in detail within the time intervals as marked with the letters from Figure 4.21 to 4.24.

Beginning of the cleanup to Point A: The block pressure smoothly goes down because of the production. There is not much change in the total mobility due to very small change in the water saturation.

Between A-B: The oil front approaches to the DP interval. The total mobility decreases due to the oil saturation increase and the water saturation decrease in the relative permeability curves, which reduces the connection productivity. The drawdown pressure increases, which enhances the connection productivity. These two effects go with different speeds and directions. The block pressure is recovered as a result because the mobility change is faster at this period, which decreases production relatively faster.

Between B-C: The total mobility decreases and then slowly increases while the water phase mobility decreases and the oil phase mobility increases. In the same period the drawdown pressure increases. These two processes increase the connection productivity and the block pressure decreases due to more production.

After Point C: The total mobility increases due to a higher oil relative permeability and a lower water relative permeability, which decreases drawdown pressure.

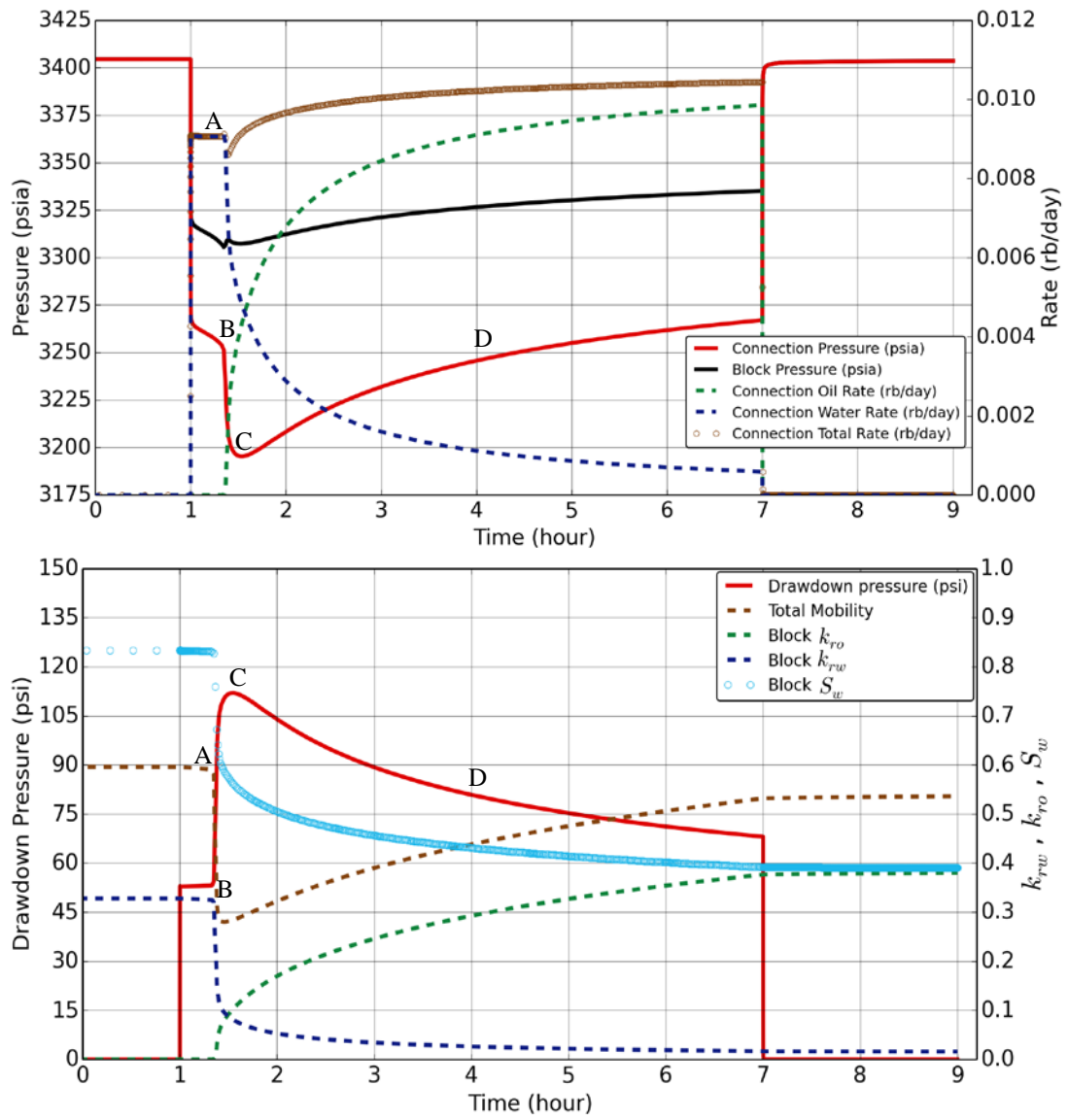


Figure 4.21: Cleanup event detailing the changes of pressures, rates and relative permeabilities at the center of the DP interval. The periods are marked as A, B, C, D, which are before, at, early after and late after the oil breakthrough, respectively.

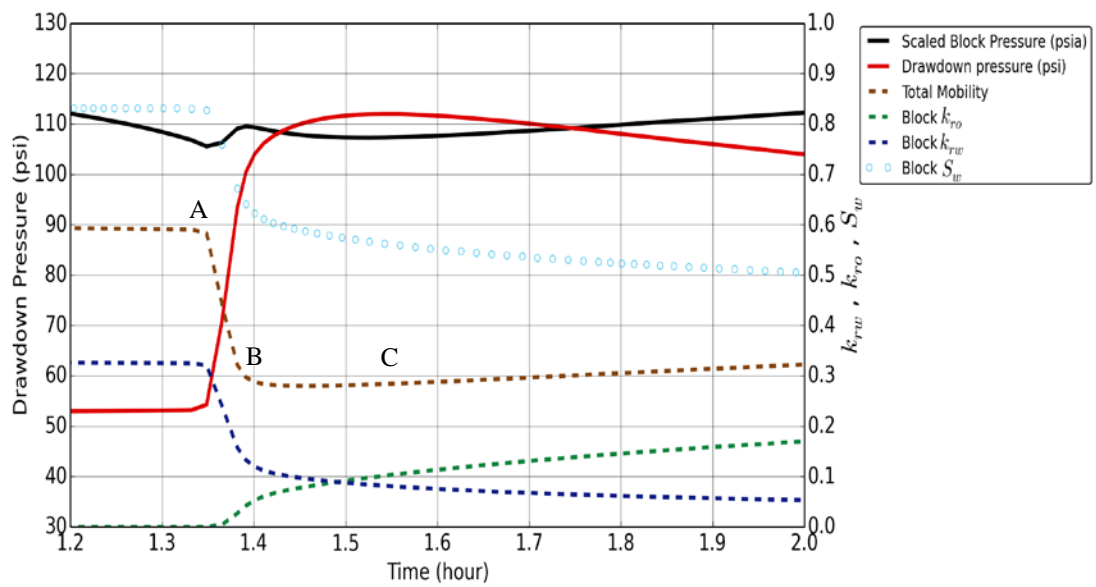


Figure 4.22: Cleanup event detailing the oil breakthrough period of Figure 4.21.

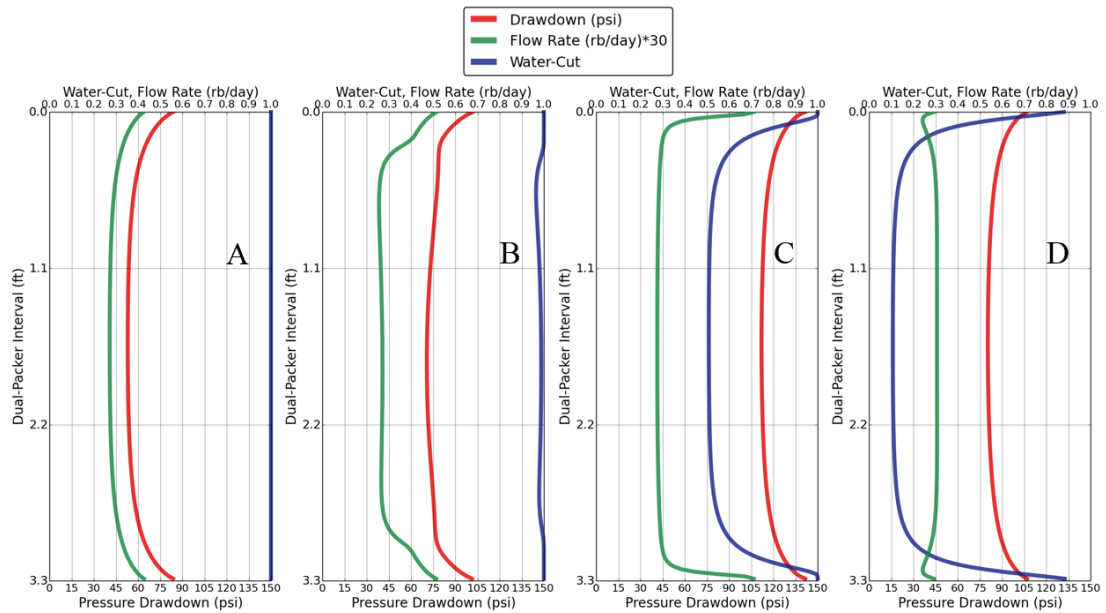


Figure 4.23: Cleanup event showing the pressure drawdown, water-cut, and rate across the DP interval before (A), at (B), early after (C), late after (D) the oil breakthrough.

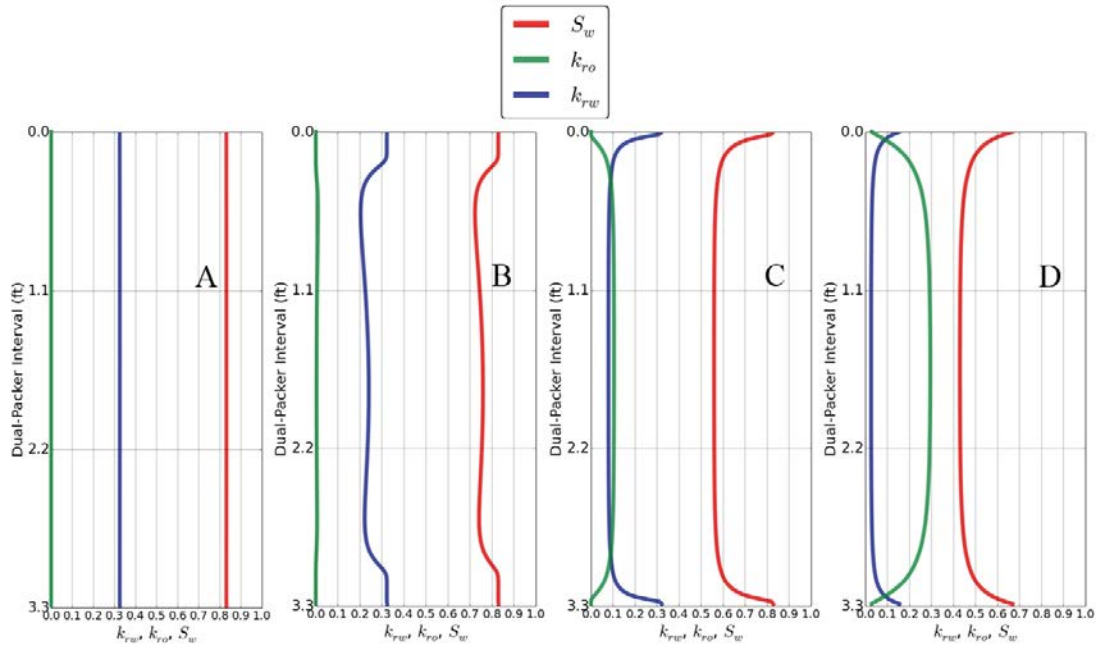


Figure 4.24: Cleanup event showing the water saturation, oil and water relative permeabilities across the DP interval before (A), at (B), early after (C), late after (D) the oil breakthrough.

## 4.6 Events and Properties Affecting Invasion and Cleanup

In this section we investigate the events and properties influencing the observed datasets during the invasion and cleanup periods.

### 4.6.1 Dynamic and Static Filtrations

Following analyses aim to establish sensitivities of DF and SF rates and durations. The total volume of invasion and event times of drilling and logging are assumed to be known. The total volume of invasion can be obtained either from openhole logs or accurate drilling reports. Arbitrary estimates of DF and SF rates and durations are used while honoring the total volume of invasion. Forward model results are compared with the base case datasets used in this chapter for the history matching of WFT water-cuts and bottomhole pressures.

Figures 4.25 through 4.27 show the DF and SF sensitivities, while keeping the cleanup start time and the total invasion volume as known parameters. It can be concluded from the sensitivity analyses presented in the figures that not only the total invasion volume should be known, but also the DF volume and the SF rate should be estimated. The total

invasion volume can be obtained from DOI analyses of openhole logs at the time of logging. The WFT cleanup is conducted after the openhole logs, and the invasion further progresses due to the continuous SF period. An estimate of the SF rate may be obtained by DOI from the openhole logs, and using the time gap between the openhole logs and the WFT cleanup. If the SF rate is estimated and the total invasion volume is known, the invasion volume in the DF period can also be estimated due to the known timeline from drilling to logging. By this way, the DF rate and its duration may not be accurately required provided that the DF invasion volume is already achieved. The initial DF rate may be estimated with a pressure overbalance and formation properties in a pressure drawdown equation for an infinite acting reservoir. Although, the DF duration is generally difficult to estimate, the invasion volume knowledge of the DF period can be sufficient as mentioned previously. This can be seen in Figures 4.25 and 4.27 in which incorrect DF durations are compensated by DF rates, while SF rates are reasonably correct, and the history matches are fairly good.

The results also indicate that, with the known total invasion volume, the cleanup data is mostly sensitive to the SF rate. Knowing the total invasion volume and matching that volume with an incorrect SF rate does not provide a good history match (see Figure 4.26). The SF rate accuracy can be improved before the WFT cleanup by time-lapse array resistivity logs from which the time-dependent DOI can be obtained. It is also possible to optimize the DF and SF rates and durations without prior knowledge with an additional computational cost. The field examples in Chapter 5 follows the course of optimization of the DF and SF properties concurrently.

Figure 4.28 represents the cases where SF is continuous and completely ceased. No SF in an openhole is highly unlikely unless a cased hole sampling operation is conducted with a special WFT tool, which does not allow any invasion. When SF is discontinuous, the oil saturation increases in the vicinity of the near-wellbore region due to the capillary pressure and the gravitational segregation.



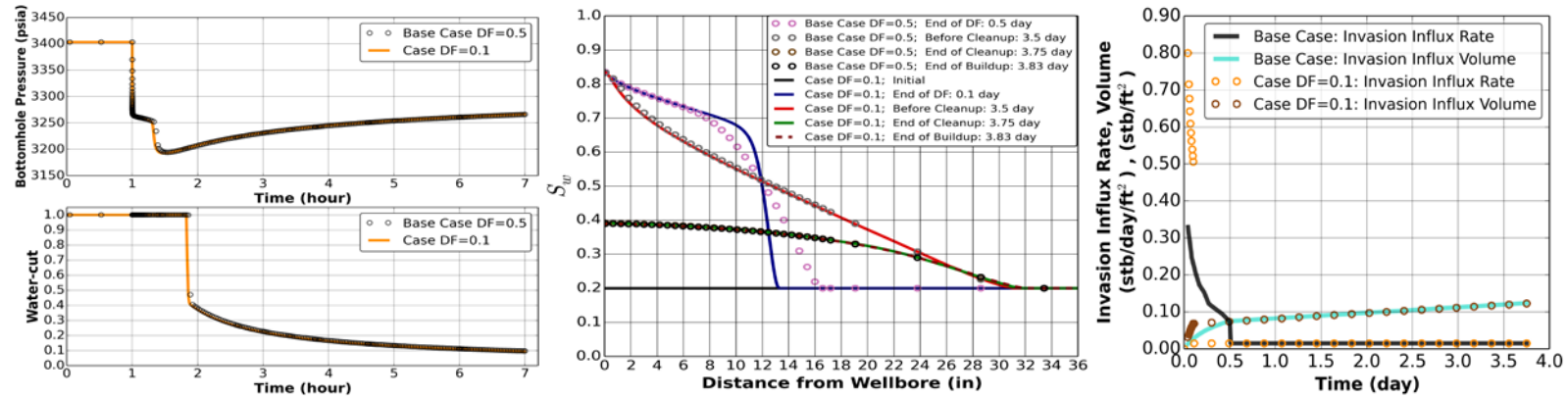


Figure 4.25: History match comparison of the 0.1-Day DF vs. the base case. DF influx rate is increased. SF influx rate and cumulative invasion volume are kept equal to the base case. The matches of bottomhole pressures and water-cuts are acceptable as seen on the left.

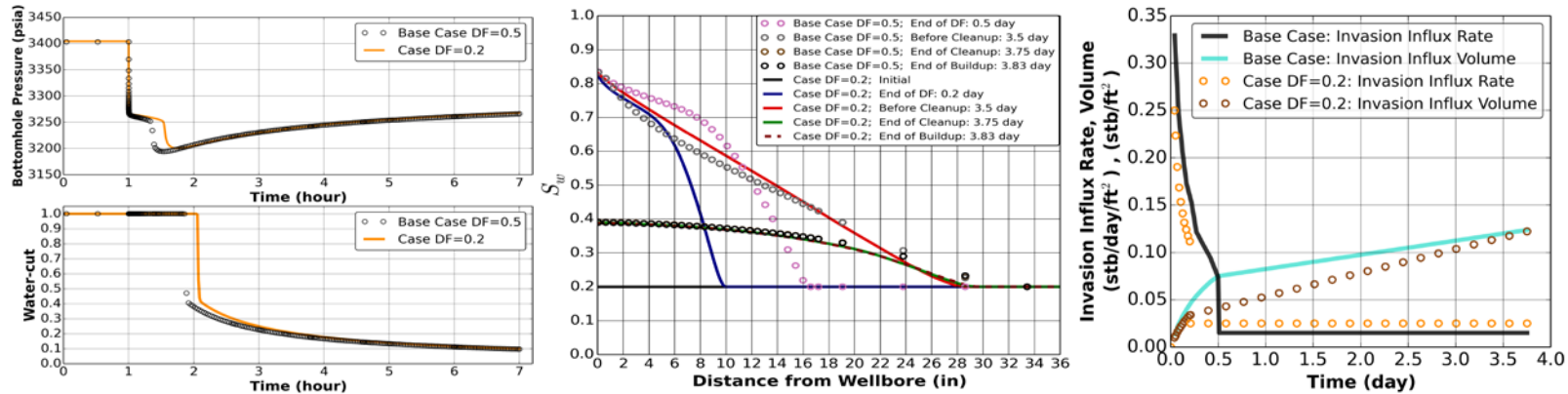


Figure 4.26: History match comparison of the 0.2-Day DF vs. the base case. DF influx rate is reduced. Static filtration influx rate is increased to match the cumulative invasion of the base case before the cleanup. The matches of bottomhole pressures and water-cuts are not acceptable. This is due to an increased water saturation profile (red curve in the middle plot) near the wellbore just before the cleanup starts.

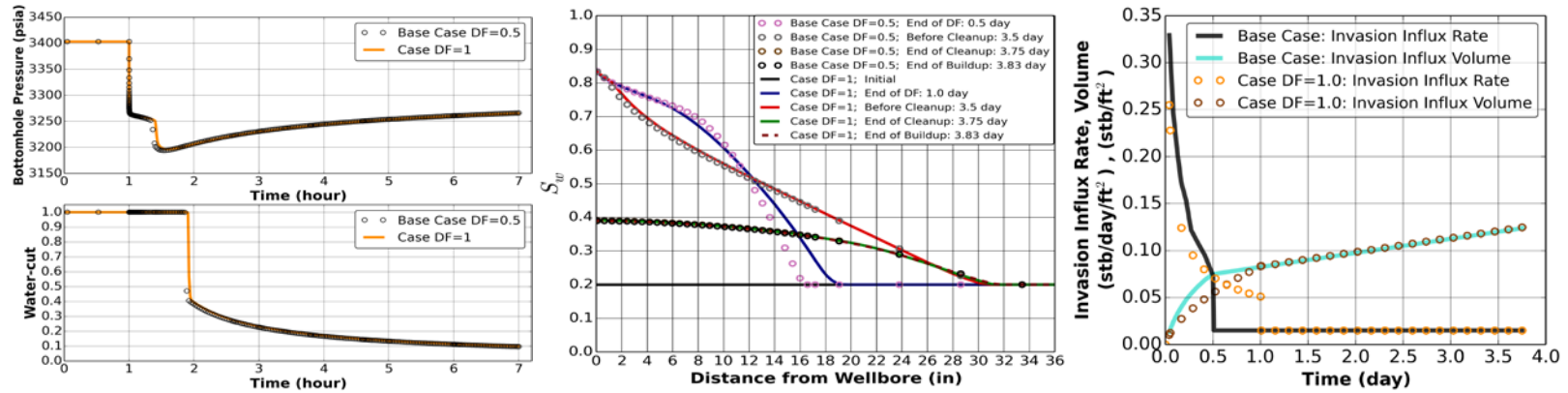


Figure 4.27: History match comparison of the 1-Day DF vs. the base case. The SF influx rate and the total volume of invasion are kept equal to the base case. The matches of bottomhole pressures and water-cuts are acceptable as seen on the left.

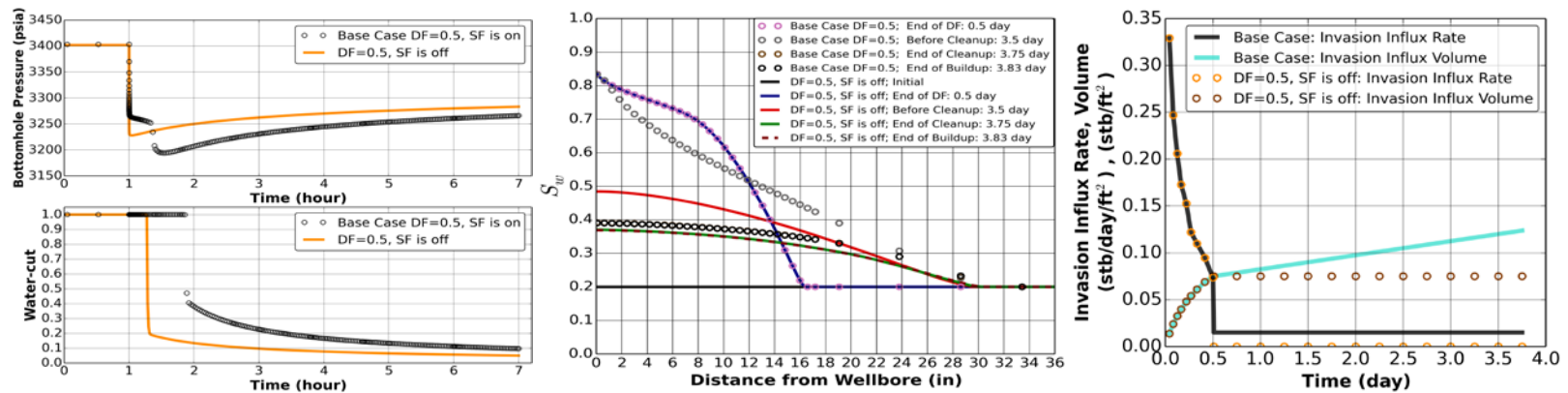


Figure 4.28: Comparison of continuous SF vs. no SF, while both cases share the same DF profile.

#### 4.6.2 Viscosity

Viscosities of the mud filtrate and the formation fluids have an impact on the invasion and the cleanup. The base and sensitivity cases assume that the mud filtrate and the formation water viscosities are equal. The base case capillary pressure curve is used in the sensitivity cases. Figure 4.29 shows that when the oil viscosity increases, the invasion goes deeper into the formation without a sharp shock-front during the DF period. The base case is represented with the curves having black circular markers. When lowering the mobility ratio,  $(k_{rw}/\mu_w)/(k_{ro}/\mu_o)$ , a more efficient displacement occurs, hence less of the shock-front smearing is observed during the DF period. Figure 4.30 shows that the shock front slowly dissipates due to capillary pressure and gravity effects during the SF period. Figure 4.31 displays the near-wellbore saturations during the cleanup and highlights that a higher oil viscosity establishes more oil saturation around the wellbore at the end of the cleanup. This is due to a higher pressure drawdown observed during the cleanup since the pumpout rates are equal in all sensitivity cases (Figure 4.32). The oil breakthrough depends on the mobility ratio, capillary and gravitational forces. When the oil and water viscosities are equal, the oil breakthrough times and the invasion profiles are similar if the capillary pressure is ignored. However, when the capillary pressure is implemented, the oil breakthrough is earlier in the same oil and water viscosity cases (Figure 4.46). Also, the lower the viscosities, the earlier the oil breakthrough in the capillary pressure cases (Figure 4.32).

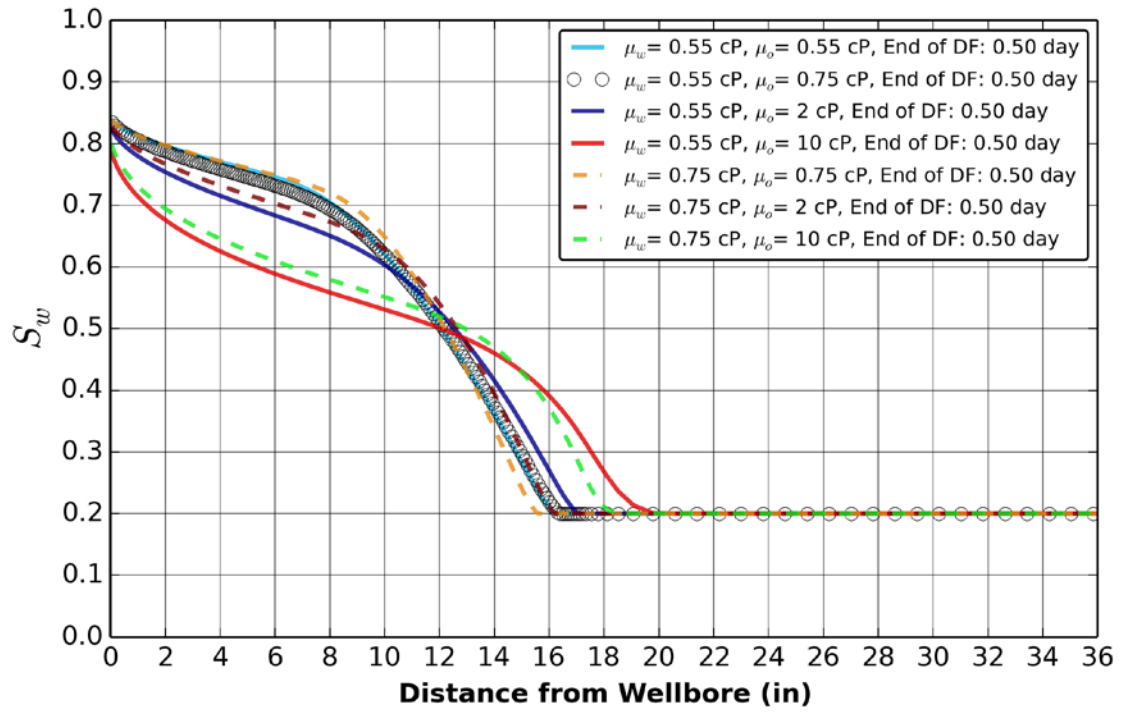


Figure 4:29: DF saturation profiles with different oil and water viscosities in the near wellbore area.

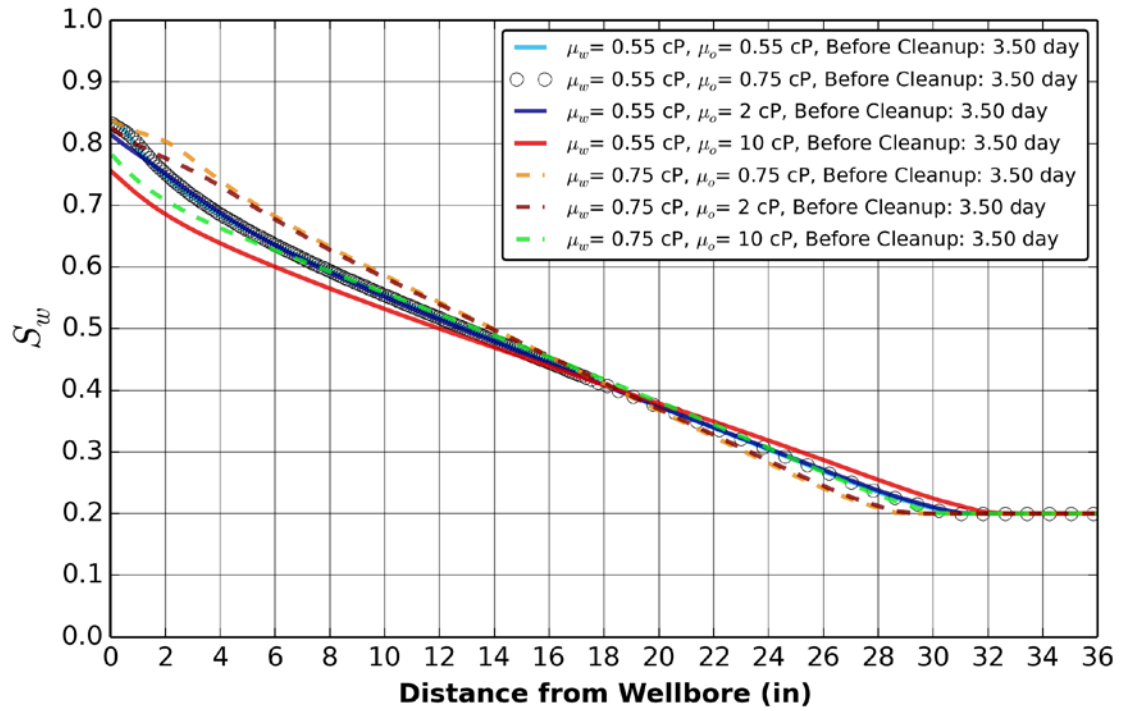


Figure 4.30: SF saturation profiles with different oil and water viscosities in the near wellbore area.

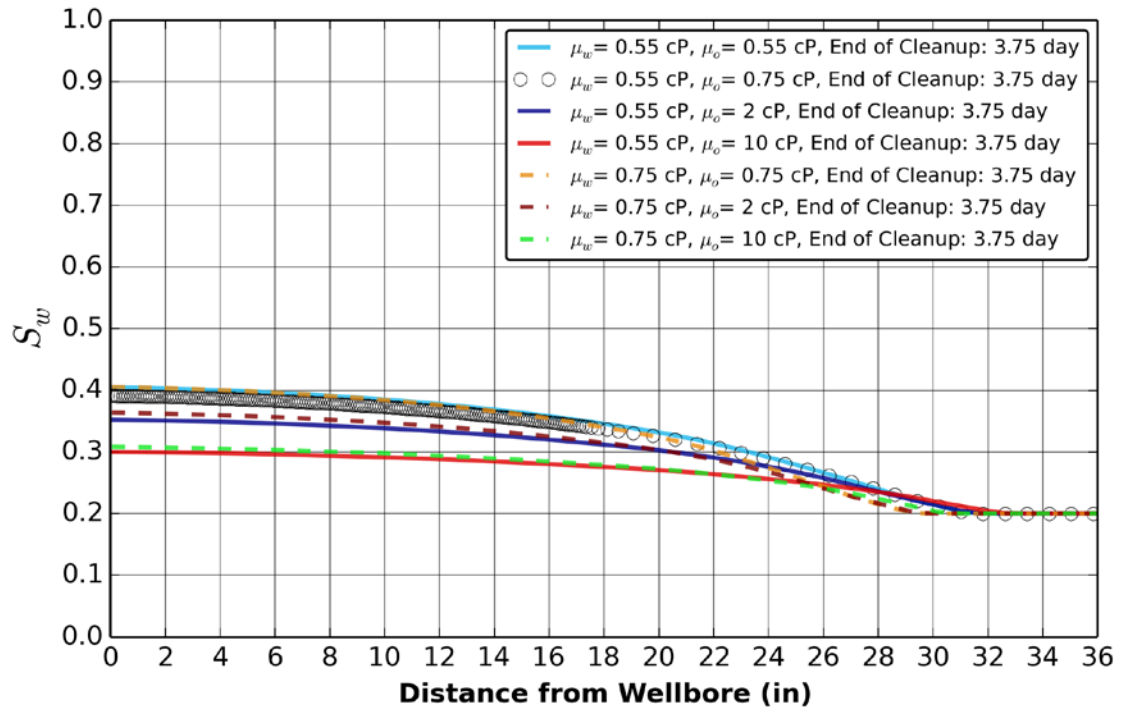


Figure 4.31: Water saturation profiles at the end of the cleanup with different oil and water viscosities in the near wellbore area.

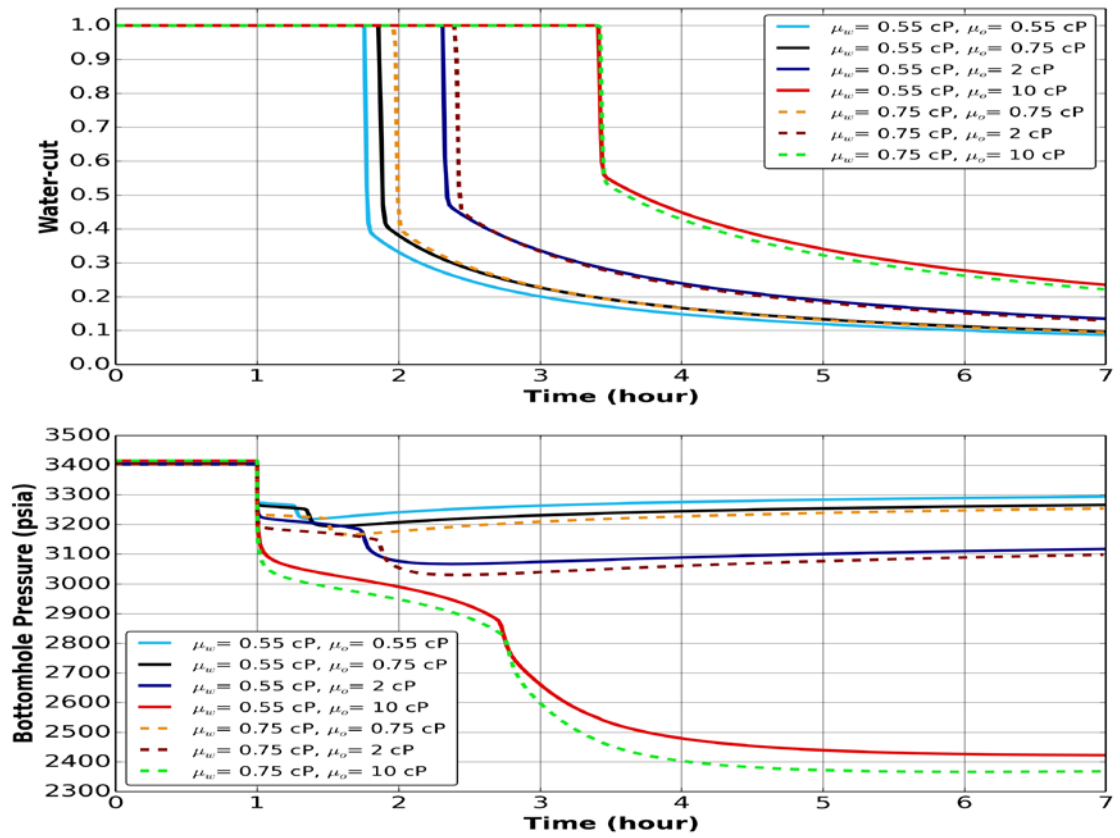


Figure 4.32: Viscosity contrasts influencing the oil breakthrough and the bottomhole pressure during the cleanup period.

#### ***4.6.3 Permeability Anisotropy***

Figure 4.33 and 4.34 show the permeability anisotropy cases at the end of the DF period, just before the cleanup, and at the end of the cleanup located at the center and the top of the DP interval. The horizontal permeability is not changed, but the vertical permeability is altered. The figures show that water saturation profiles of the DF and SF periods are grouped together at near-equal values in the vicinity of the wellbore region. The figures also indicate that during the cleanup, saturation profiles are different, but not with a large magnitude for our cases. This interesting saturation distribution is further investigated at the sandface, 8 in, 15 in and 22 in into the reservoir across the DP interval in Figure 4.35. The DP interval resides between 3.8 ft and 7.1 ft from the top boundary of the reservoir. The center of the DP interval is at 5.5 ft. The figure confirms that the saturation profiles during the DF and SF periods grouped together at near-equal values and the cleanup saturation profiles are different. The invasion periods, although governed by capillary, viscous and gravitational forces, are mainly influenced by the influx rate and the horizontal permeability since the horizontal permeability is assigned to a layer and the invasion occurs across the entire reservoir. The vertical permeability effect seems less than the horizontal permeability during the invasion. However, during the cleanup from the DP interval, reduction in the vertical permeability increases the drawdown and makes the hydrocarbon breakthrough earlier with the same flow rate and the horizontal permeability, and the opposite is also true as shown in Figure 4.36.

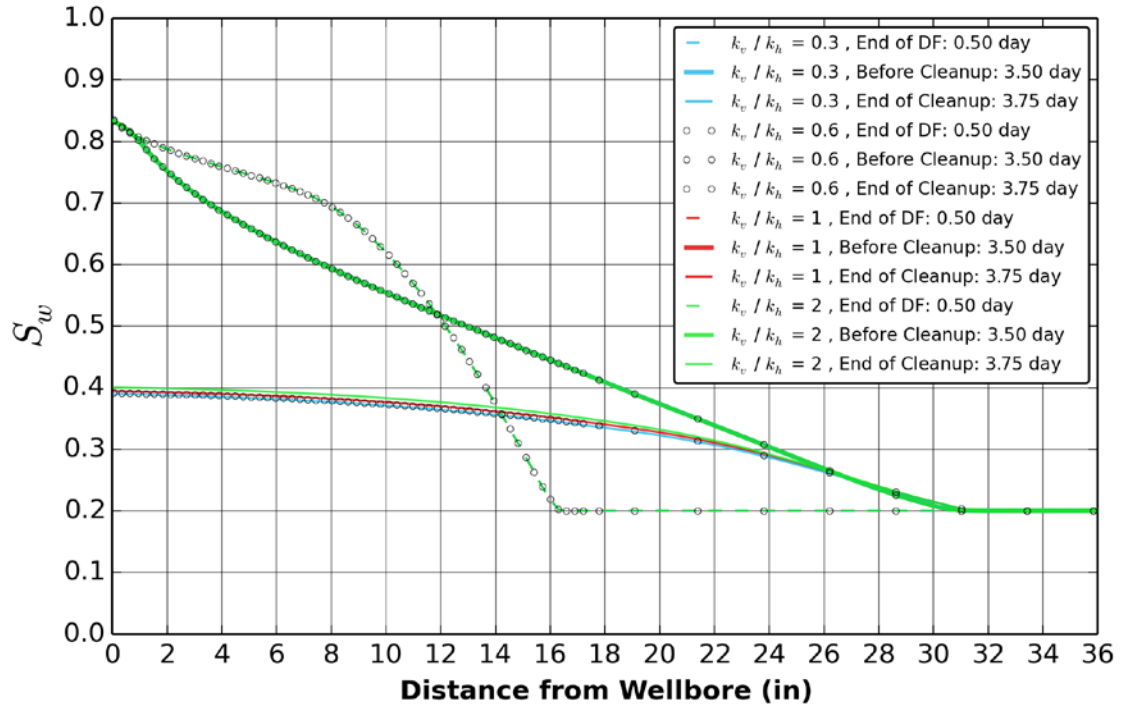


Figure 4.33: Water saturation profiles at the end of the DF, at the beginning and the end of the cleanup at the center of the DP interval in the anisotropy cases.

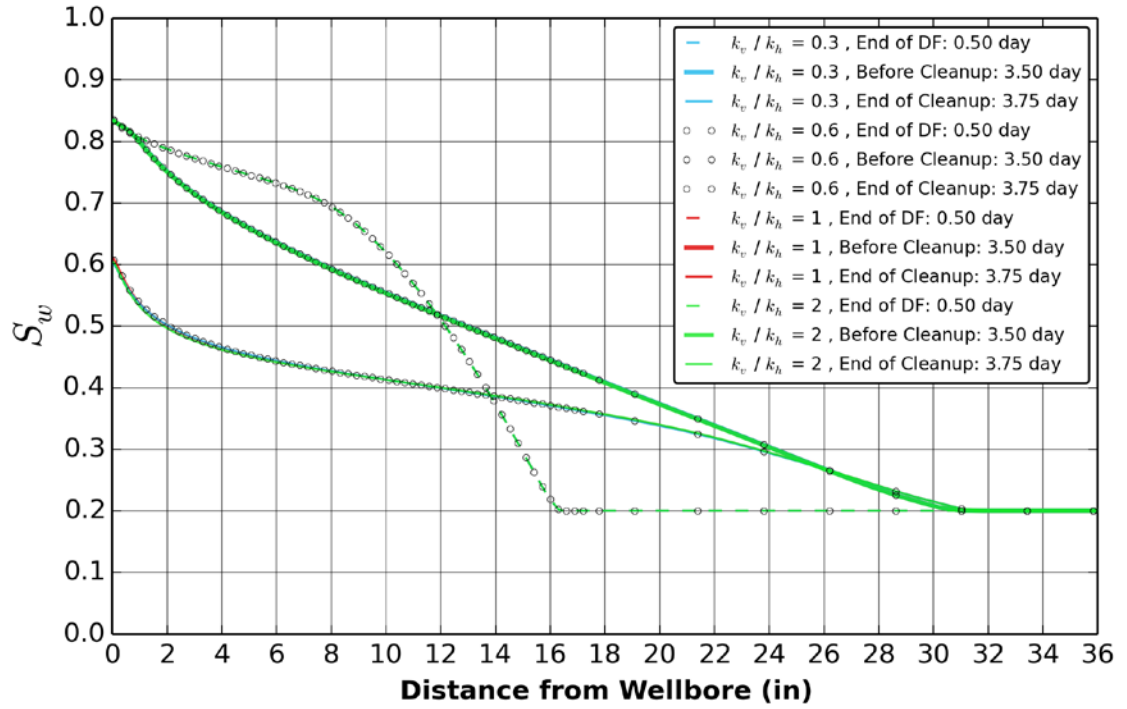


Figure 4.34: Water saturation profiles at the end of the DF, at the beginning and the end of the cleanup at the top of the DP interval in the anisotropy cases.

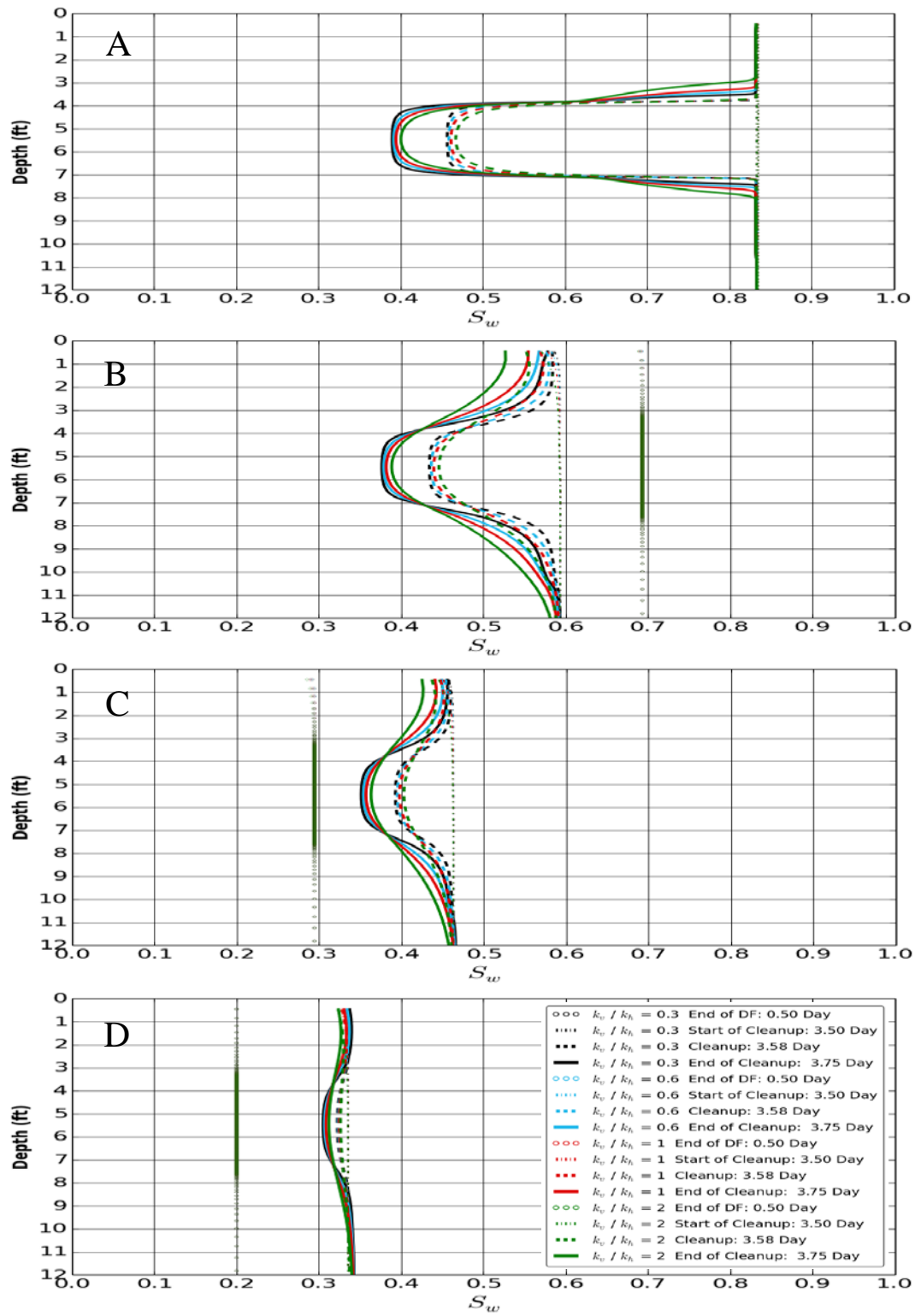


Figure 4.35: Water saturations are presented across the DP interval at the sandface (A), at 8 in (B), 15 in (C) and 22 in (D). The center of the DP interval is at 5.5 ft and the height of the DP interval is 3.3 ft residing between 3.8 ft and 7.1 ft from the top of the reservoir. The horizontal permeability is kept unchanged, but the vertical permeability is altered in the anisotropy cases.



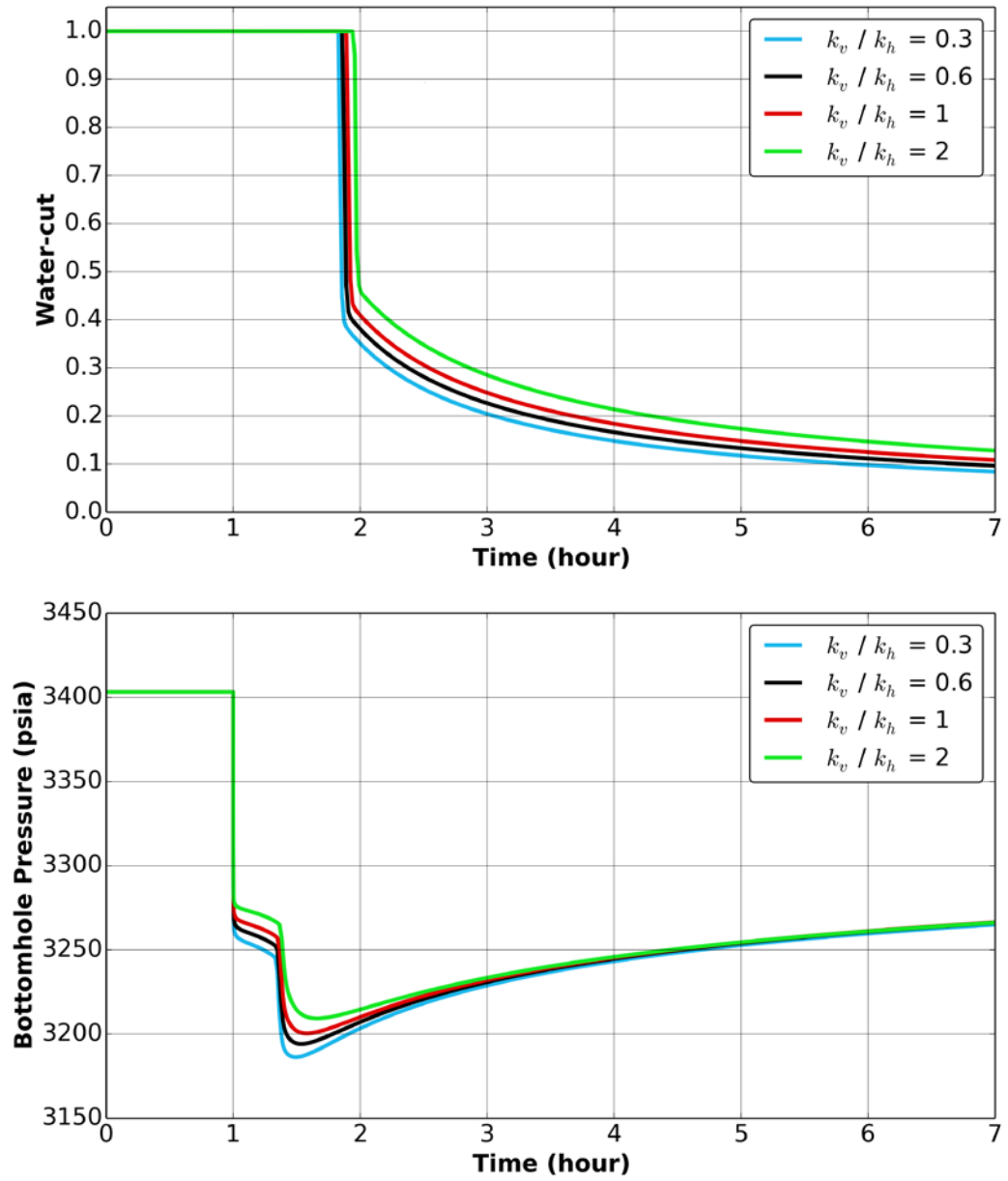


Figure 4.36:  $k_h$  is 20 md and  $k_v/k_h$  is 0.6 in the base case.  $k_h$  is not changed, but  $k_v/k_h$  ratio is altered to 0.3, 1, and 2.

#### 4.6.4 Porosity

Figure 4.37 displays the WFT bottomhole pressures and water-cuts during the cleanup for the three different porosity cases. All other reservoir properties are kept unchanged and the base case has the porosity of 0.3. Figure 4.38 shows the porosity effect on the saturation profiles during the invasion and the cleanup. The higher the porosity, the shallower the depth of invasion, and the quicker the oil breakthrough because the mud-filtrate invasion volumes and durations are identical in each case.

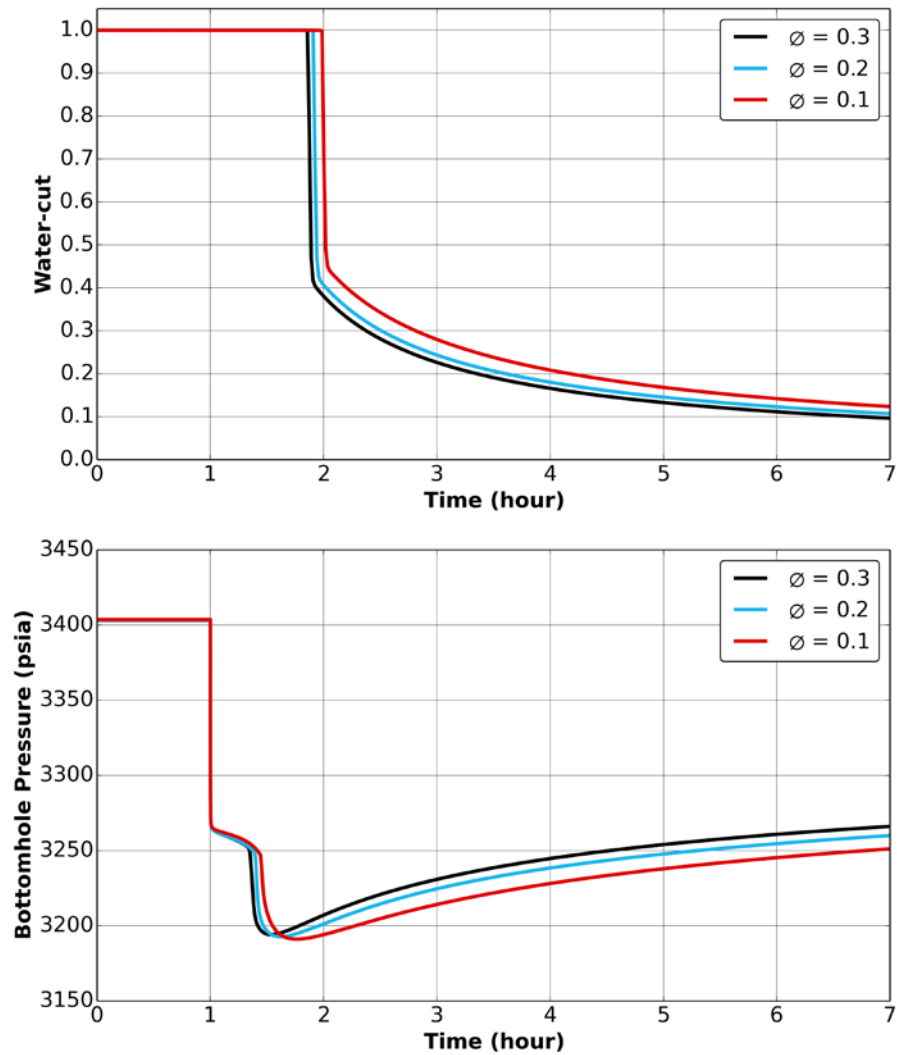


Figure 4.37: Cleanups are conducted with the three different porosities. The porosity is equal to 0.3 in the base case.

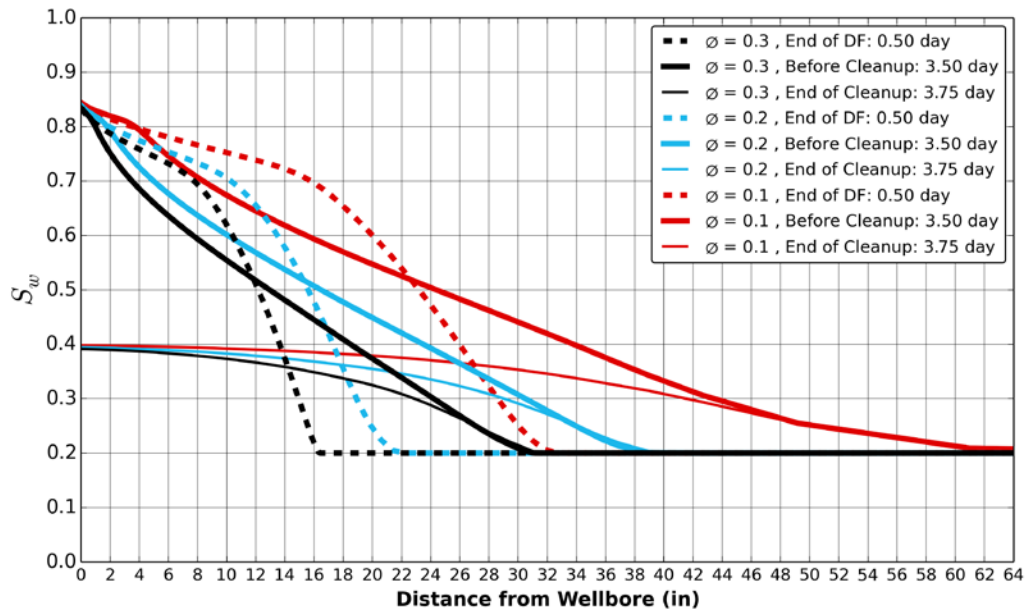


Figure 4.38: Saturation profiles at the end of the DF period, at the beginning and the end of the cleanup for the porosity cases of 0.3, 0.2 and 0.1. The invasion volumes and durations are kept the same as in the base case.

#### 4.6.5 Damage Skin

A larger damage skin creates a higher pressure drawdown with the same pump rate as known and the hydrocarbon breakthrough is earlier although the water-cut trend on the cleanup is similar (Figure 4.39). The connection pressure (CPR), bottomhole pressure (WBHP) and block pressure at the sandface (BPR) are displayed for each skin factor in Figure 4.39. If bottomhole and connection pressures are at the same datum depth, they are equal to each other. The block pressures are different (although they are slightly different in these cases) for each skin factor due to different wellbore pressures altering the block pressures at the sandface. Figure 4.40 shows the saturation profiles into the reservoir with the damage skin cases of 0, 2 and 4. The base case has the skin factor of 2. The invasion profiles are unaltered and the cleanups with the different skin factors display minor changes in the saturation profiles. One might expect that because of a larger skin factor, with the same pump rate, the pressure drawdown is more and higher oil saturations are expected in the near wellbore region. WFT pump volumes are generally small during the cleanup and sampling; hence, the additional saturation changes due to the extra pressure drawdown in the vicinity of the wellbore is relatively small (Figure 4.40).

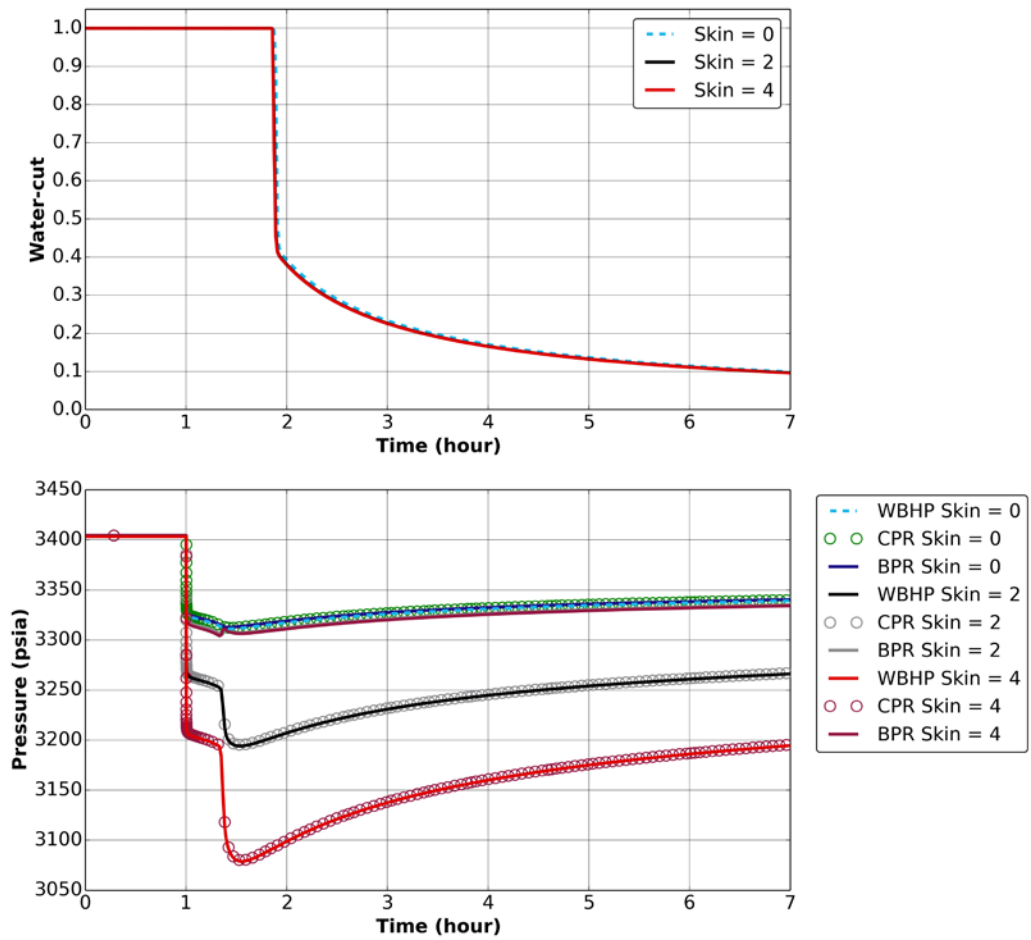


Figure 4.39: Damage skin values are compared during the cleanup. The base case has the damage skin of 2.

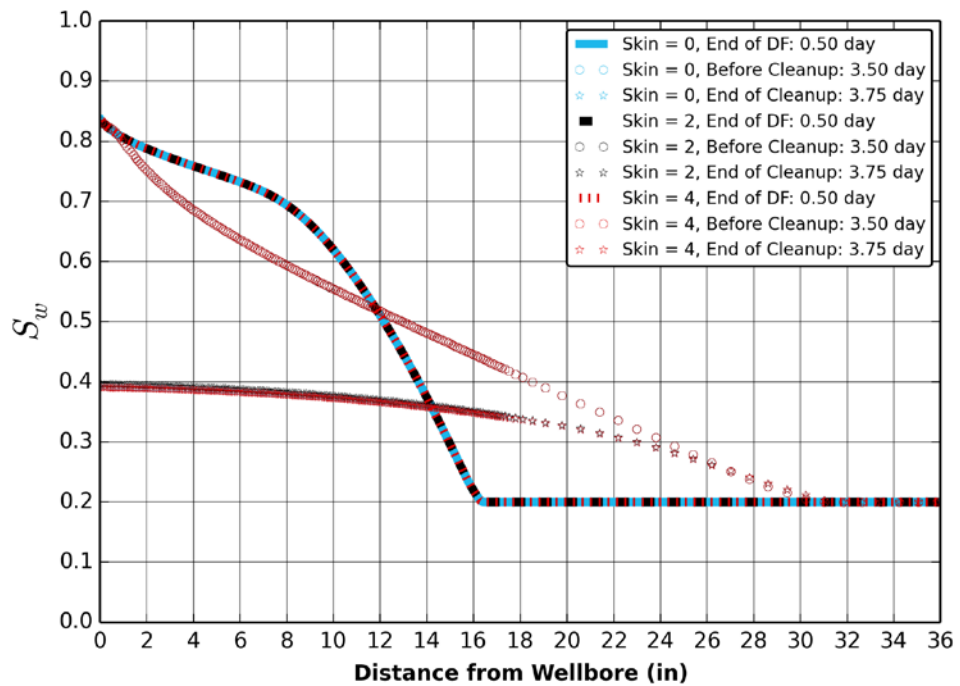


Figure 4.40: Water saturation profiles for the skin factors of 0, 2, and 4 at the end of the DF period, at the beginning and the end of the cleanup.

#### 4.6.6 Capillary Pressure

The capillary pressure affects the invasion and cleanup processes by altering the saturation profiles in the invaded zone. The same capillary pressure curve is assumed applicable for both the invasion (imbibition) and the cleanup (secondary drainage) processes in our study. Figure 4.41 presents the capillary pressure curves on a semilog graph used in this section. The curve with the black markers represents the capillary pressure in the base case. Figures 4.42 to 4.45 illustrate the capillary pressure effects during the invasion and the cleanup. The general trend shows that the capillary pressure having a higher maximum value at  $S_{wi}$  with a lower pore-size distribution index,  $\lambda$  generates more smearing at the invasion front. The capillary pressure continuously alters the saturation distribution in the invaded zone during the DF and SF, and the cleanup periods. The capillary pressure changes the water-cut and bottomhole pressure behaviors during the cleanup since the saturation profile is altered in the near-wellbore region. Higher  $P_d$  and lower  $\lambda$  values create larger capillary pressure values at  $S_{wi}$  where the oil breakthrough is relatively earlier. This is because the oil pressure is higher than the water pressure, and oil moves towards the wellbore and the progressing mud-filtrate invasion is also transported deeper into the formation while near-wellbore water saturations are decreased. If no capillary pressure is introduced in the model, the invasion front is sharper and the oil breakthrough occurs relatively later. The purpose of this comparison is to show that the time delays after drilling or between openhole logs play a significant role when capillary pressure is included in modeling.

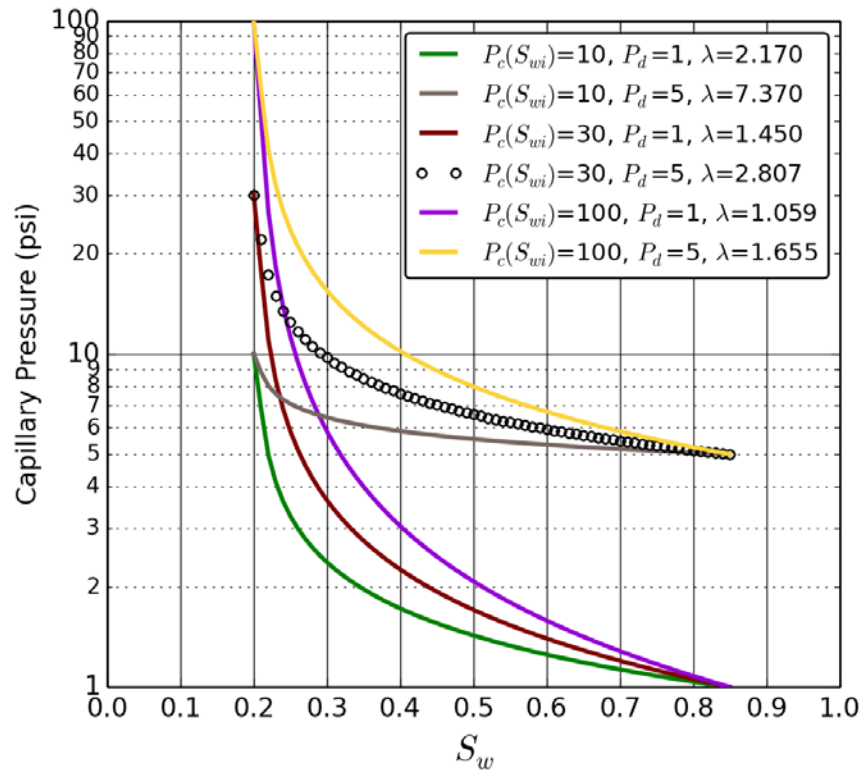


Figure 4.41: Capillary pressure curves used for the sensitivity analyses. The curve with the black markers represents the capillary pressure in the base case. The capillary pressures are generated with the modified Brooks and Corey capillary pressure correlation.

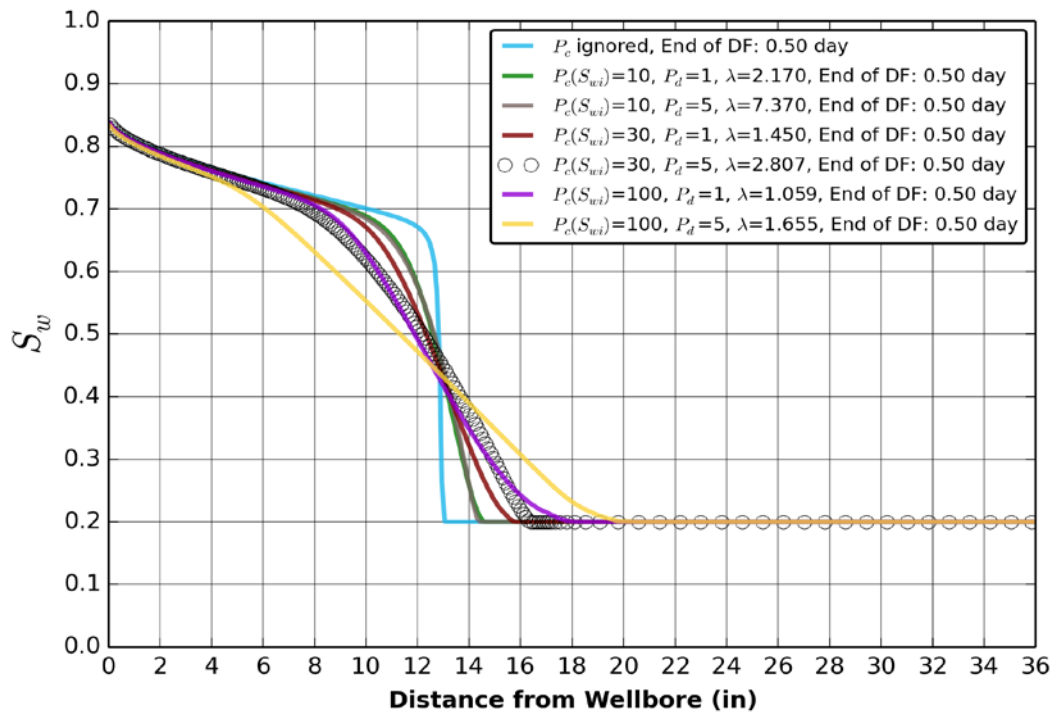


Figure 4.42: Water saturation profiles with the capillary pressure curves at the end of the DF period displayed from the wellbore to 36 in into the reservoir.

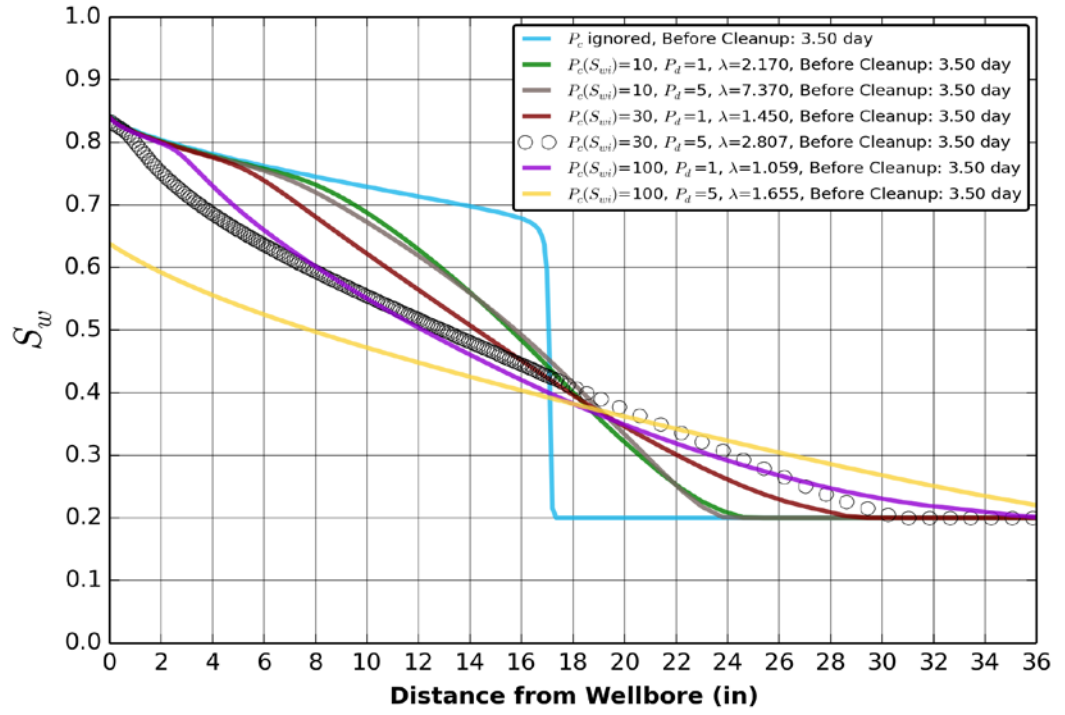


Figure 4.43: Water saturation profiles with the capillary pressure curves at the beginning of the cleanup displayed from the wellbore to 36 in into the reservoir.

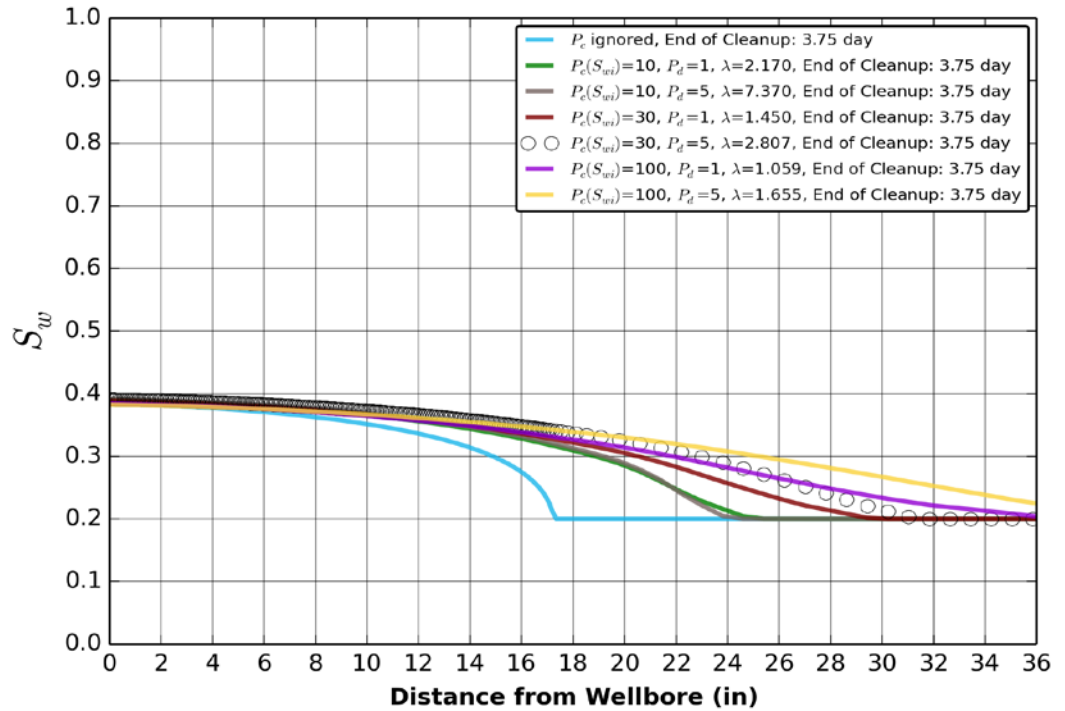


Figure 4.44: Water saturation profiles with the capillary pressure curves at the end of the cleanup displayed from the wellbore to 36 in into the reservoir.

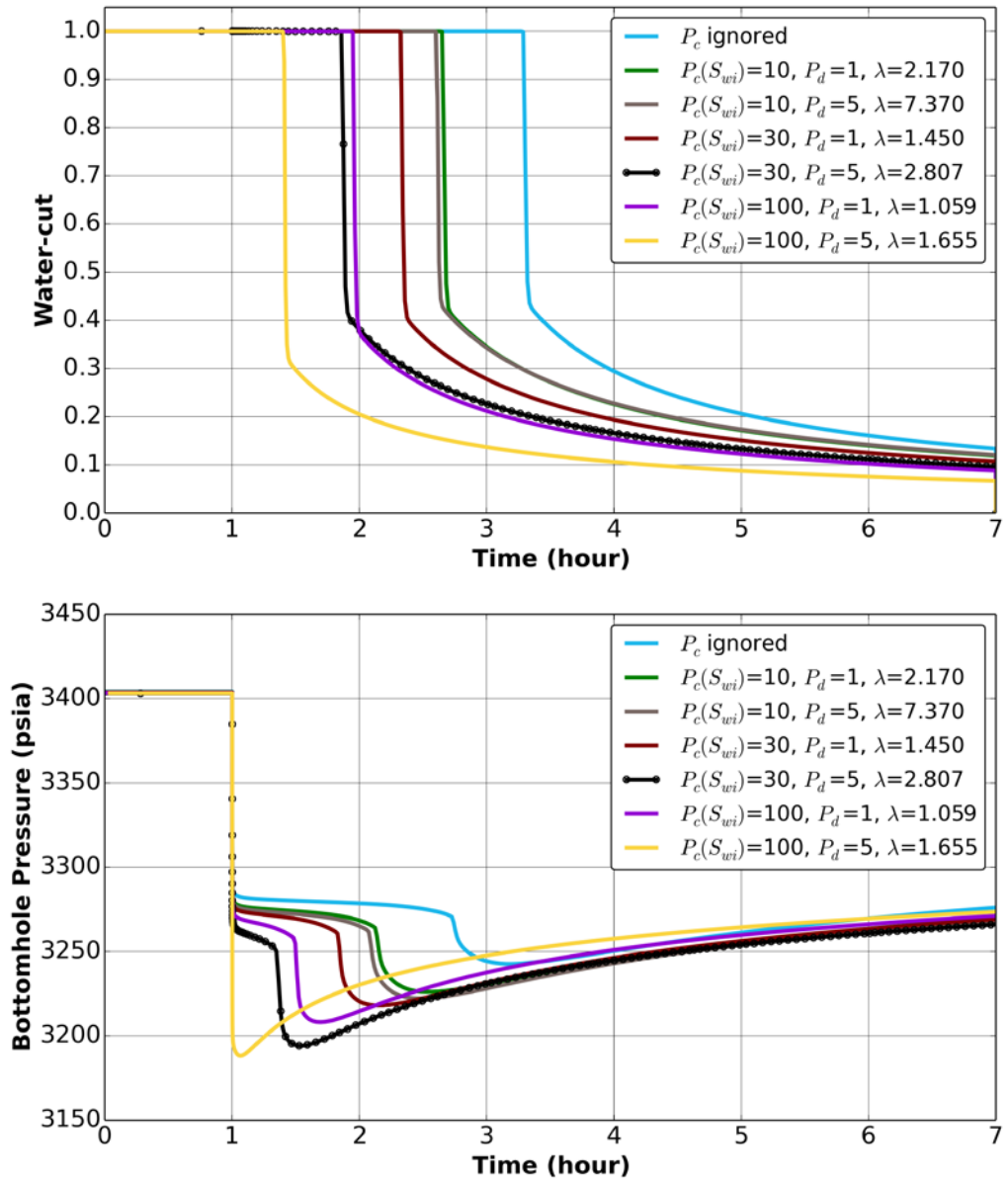


Figure 4.45: WFT bottomhole pressures and water-cuts are displayed with the capillary pressure sensitivities. The black curves represent the base case. Higher  $P_d$  and lower  $\lambda$  values create a higher capillary pressure at  $S_{wi}$  and generate relatively an earlier oil breakthrough.



Figure 4.46 compares the effects of viscosities and capillary pressures together. Two sets of viscosities are implemented while the capillary pressure in the base case is applied and later ignored. In both cases oil and water viscosities are kept equal to 0.55 cP and 0.75 cP. When the capillary pressure is ignored since the mobility ratio in both viscosity cases are equal, the invasion profiles are nearly the same and the invasion generates sharper shock fronts (Figure 4.47). The cleanup profiles are also very similar except that due to a larger pressure drawdown when oil and water have higher viscosities, it will create slightly better cleanup with the same pump rate. When the capillary pressure is applied for the equal viscosity cases, the lower viscosity case shows an earlier oil breakthrough because of larger smearing of the shock-front during the invasion. This is due to a quicker exchange of the fluid phases with the same capillary pressure.

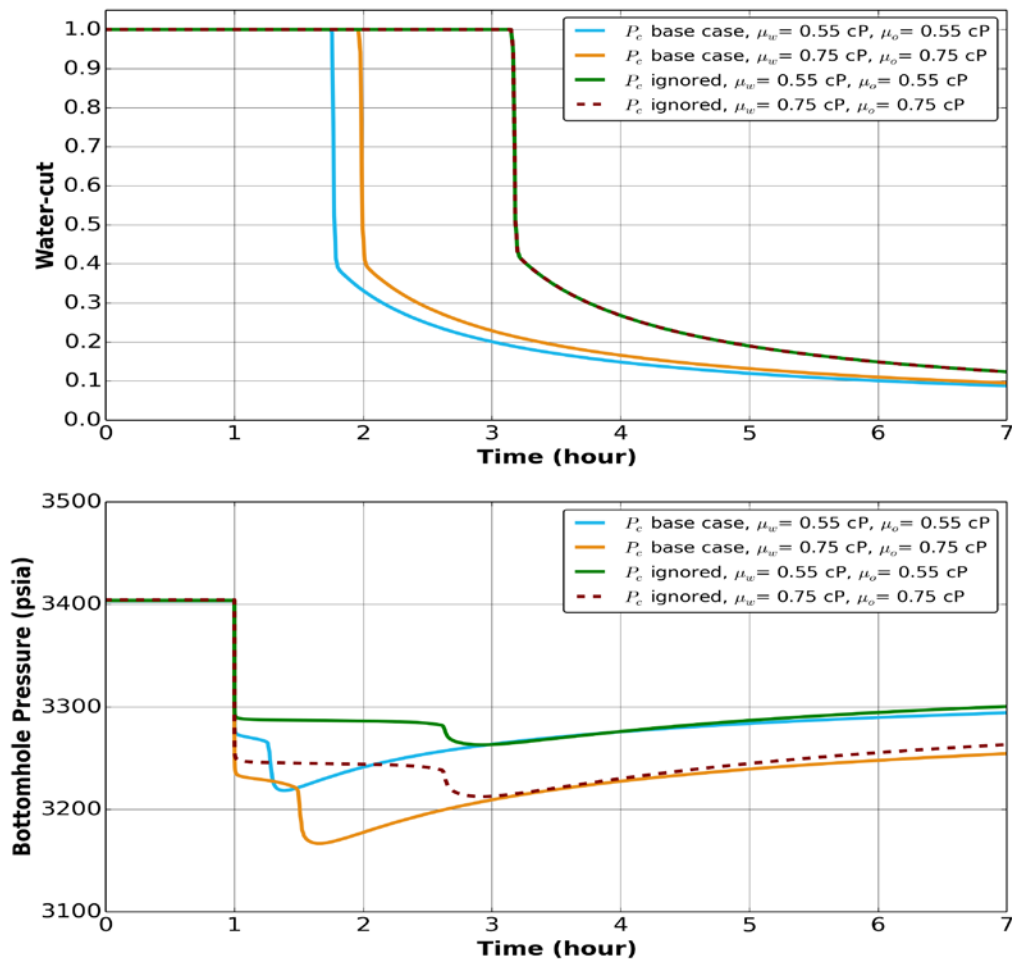


Figure 4.46: WFT bottomhole pressures and the water-cuts during the cleanup when the capillary pressure is applied and later ignored for the two sets of equal fluid viscosities.

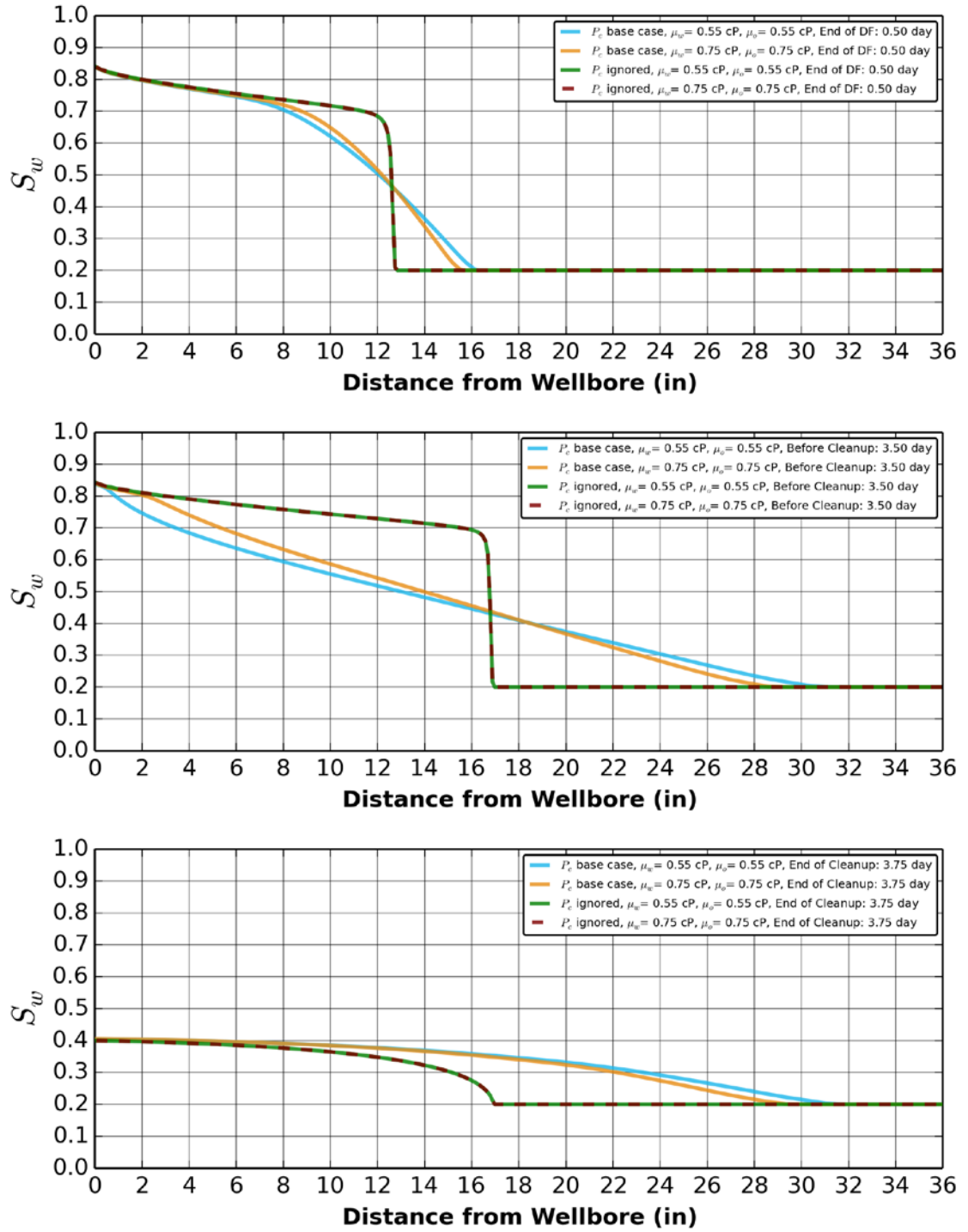


Figure 4.47: Water saturation profiles at the end of DF (top), before the cleanup (middle), and after the cleanup (bottom) when the capillary pressure is applied and later ignored for the two sets of equal fluid viscosities.

Figure 4.48 imitates an operational delay before the WFT cleanup while the capillary pressure is implemented as in the base case. All of the cases have identical DF periods and matching SF rates with various SF durations. Figure 4.1 shows the influx rates for the DF and SF periods. Figure 4.48 indicates that when the cleanup starts right after the DF period, the oil breakthrough time is not earlier comparatively although the invasion volume is relatively lower (the blue curves in Figure 4.48). The capillary pressure becomes more influential after a short time in the SF period, and the oil breakthrough occurs earlier (the green, red and black curves in Figure 4.48). The relationship of the oil breakthrough time depends on the duration and influx rates of the DF and SF periods. If the SF period becomes excessively long, then the volume of the mud-filtrate invasion, relative to the reservoir volume influencing, increases and the oil breakthrough is delayed again (the dashed curves having brown, purple and yellow colors in Figure 4.48). Figure 4.49 shows the capillary pressure influence over the water saturation profiles for each case displayed at the start of the cleanup. Figure 4.50 displays the water saturation profiles at the end of the cleanup. When SF duration is extended, the depth of invasion is deeper, and also translates to higher sandface water saturations. In summary, the invasion rates and their durations, and the magnitude of the capillary pressure will create a different oil breakthrough and saturation profile scenarios. This could be further complicated when heterogeneities are introduced and multiple DF and SF periods are forced into the reservoir due to the necessary operations in the wellbore, such as wiper trips or movements of tools that scrape the mud-cake.

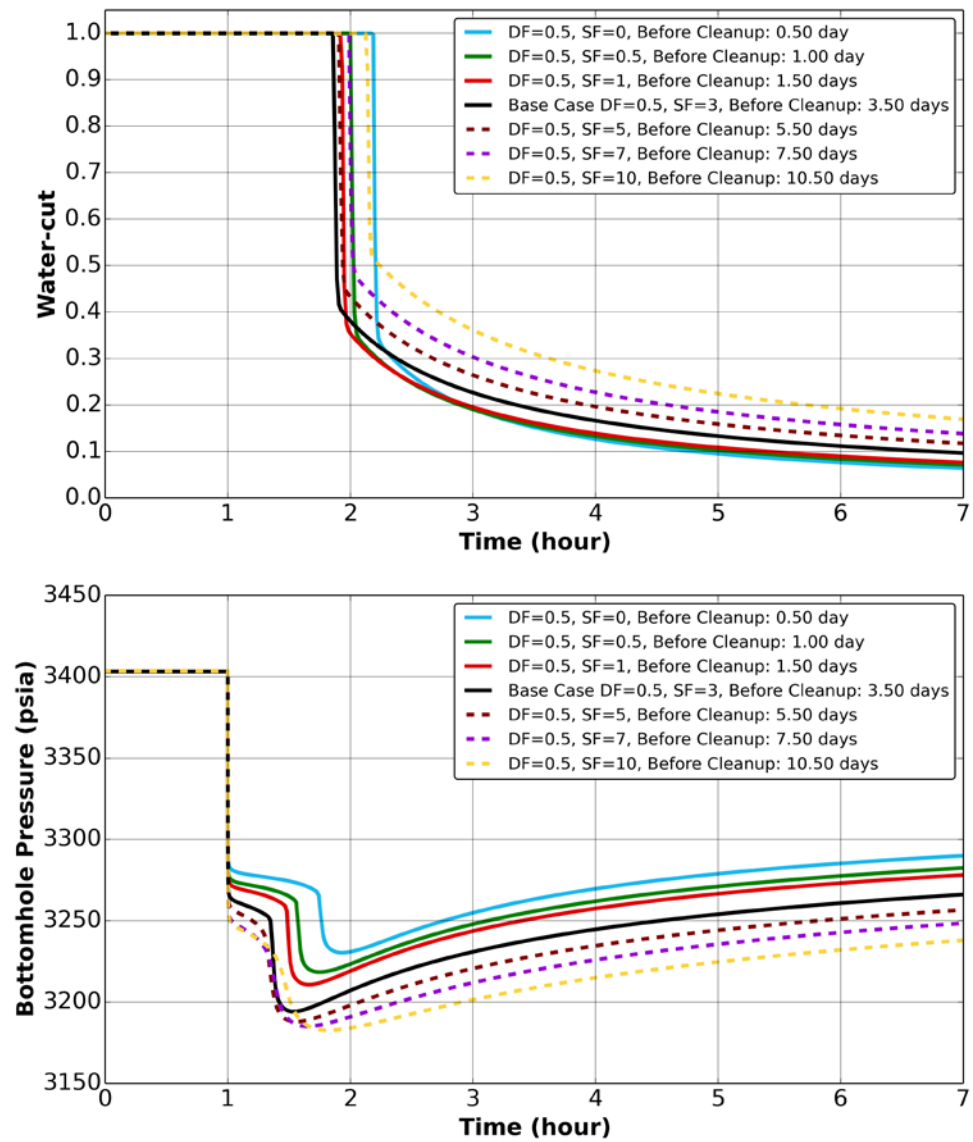


Figure 4.48: WFT bottomhole pressures and water-cuts during the cleanup. All of the cases have identical DF periods and matching SF rates with various SF durations.

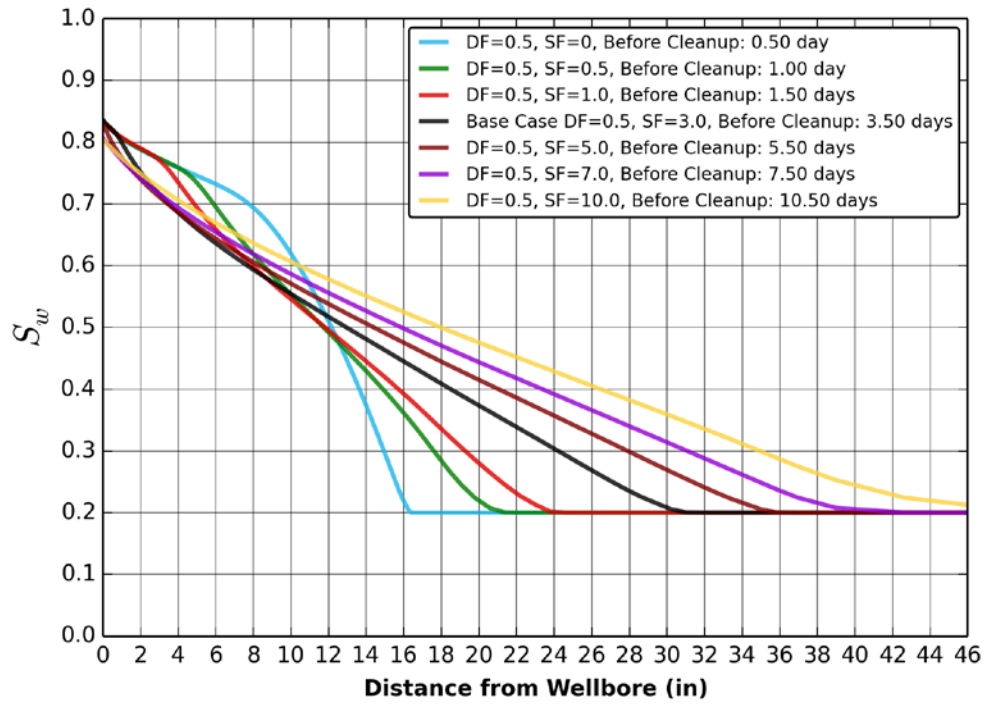


Figure 4.49: Water saturation profiles for each case before the cleanup in the vicinity of the wellbore. All of the cases have identical DF periods as in the blue curve and the matching SF rates with various SF durations.

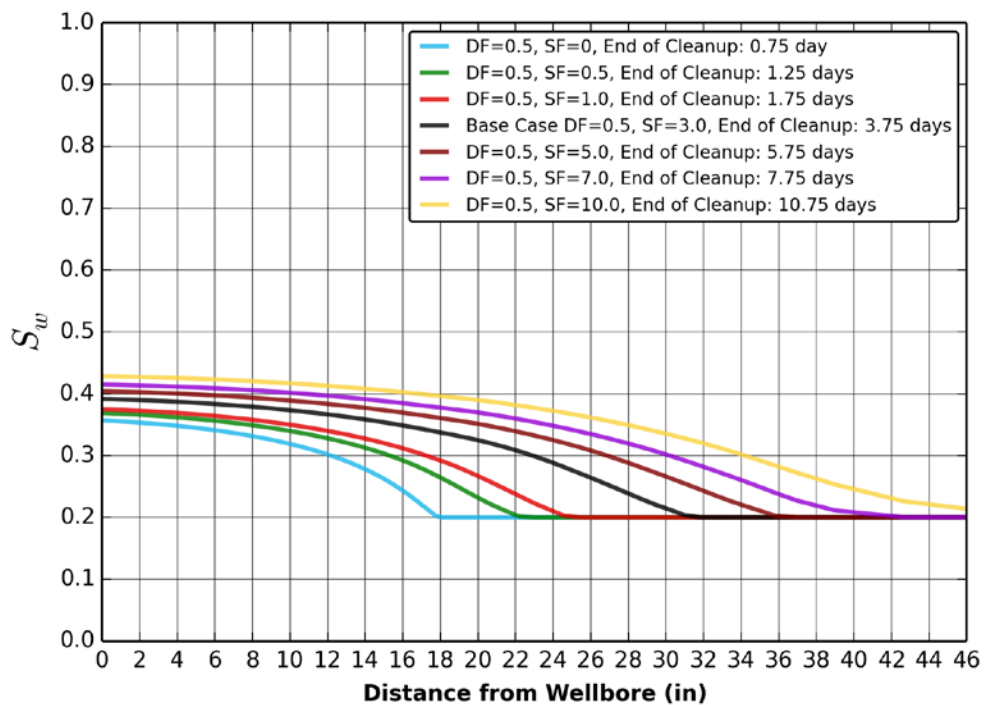


Figure 4.50: Water saturation profiles for each case at the end of the cleanup in the vicinity of the wellbore. All of the cases have identical DF periods and the matching SF rates with various SF durations.

#### 4.6.7 Hysteresis

The hysteresis section is brief since we did not include synthetic or field examples. When the hysteresis of relative permeability and capillary pressure is considered in a numerical model, the mud-filtrate invasion follows imbibition curves. When the cleanup starts as a drainage process, scanning drainage curves are generated as a new trend from the current block saturation (see Chapter 2.8 for details). Figure 4.51 shows increasing distances specified as shallower to deeper (left to right) from a wellbore into the reservoir. The location near to the wellbore (shallower) has the largest amount of mud-filtrate saturation of around 0.60 before the cleanup. The location stated as deeper in the reservoir is also in the invasion zone and shows the maximum mud-filtrate saturation of 0.45 before the cleanup. The location called as deepest represents the uninvaded zone and at the initial saturation condition ( $S_{wi} = 0.20$ ). Orange arrows show the direction of the imbibition process while purple arrows display the direction of the drainage process according to the scanning curves. Black circular marks present the numerical results of progressing capillary and oil relative permeability values in both processes. Black cross marks are the numerical results for the water relative permeability curves in both processes. When the cleanup begins, the mud-filtrate saturation starts receding from its maximum value in the block following the drainage scanning curves as explained earlier.

The objective of the WFT hysteresis optimization should be to obtain bounding imbibition and drainage curves. This is because generation of the bounding curves from core analyses is often performed and preferred for certain simulation scenarios, and establishing scanning curves from core analyses is difficult and rare. Unlike the WFT hysteresis process, it is not common for a well to go through waterflood and production cycles sequentially. Reservoirs are initialized with drainage curves, and then imbibition curves are applied for the waterflood in the case of water injectors and oil producers. Both scanning imbibition and drainage curves as in Figure 4.51 are not generally used for the waterflood in a numerical model although these cycles may occur in such scenarios: during coning and moving banks of different fluids in space over time, a shut-in producer with a water-cut is put back on production after oil reinvading the near wellbore region, a three-phase case of water-alternating-gas (WAG) scheme. In the WFT hysteresis process, the parameterization method selected should follow the expected saturation hysteresis trends, which may require further studies to clarify, and should also accurately establish the bounding curves for a general application.

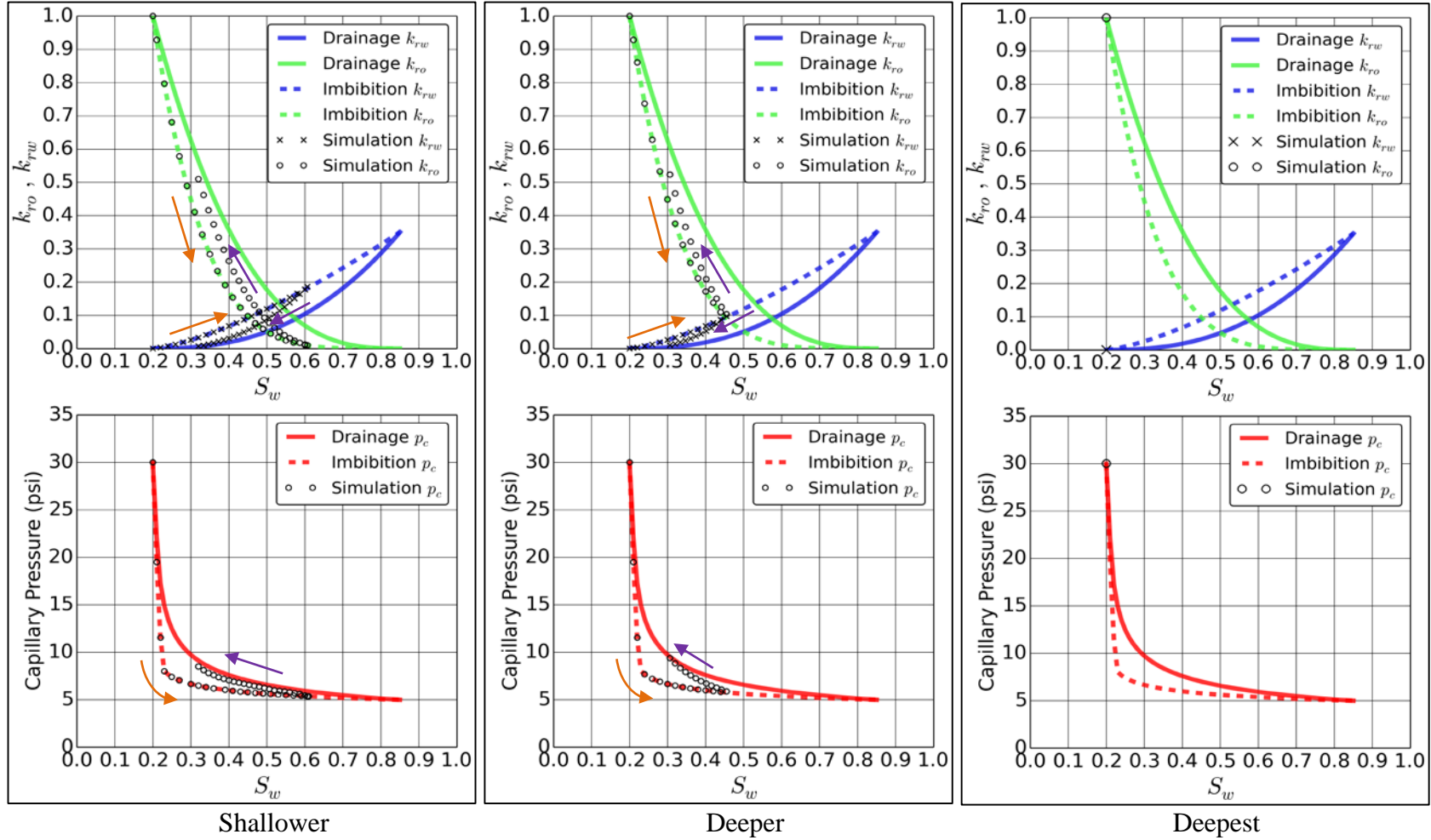


Figure 4.51: Progress of relative permeabilities and capillary pressures in a hysteretic process at the shallower to deeper locations in the reservoir. Orange arrows show the direction of the imbibition process while purple arrows display the direction of the drainage process.

## **CHAPTER 5. WORKFLOW FOR GENERATION OF RELATIVE PERMEABILITIES AND CAPILLARY PRESSURES**

Both gradient and stochastic based optimization methods are used in the synthetic examples; however, the stochastic based optimization is chosen for the field examples. The reasons are explained in Chapter 5.4 in detail. The proposed workflow of stochastic based optimization for generation of relative permeabilities and capillary pressures is valid in hydrocarbon reservoirs for wells drilled with WBM and summarized as follows:

1. Analyze openhole logs for rock and fluid properties, and mud-filtrate invasion:
  - i. Obtain initial guess of mud-filtrate invasion profile from inversion of electrical and dielectric logs (optional).
  - ii. Calculate water and oil saturations (optional).
2. Prepare simulation data according to geological and petrophysical logs, and their accurate timelines:
  - i. Interpret horizontal and vertical permeabilities and damage skin from WFT pressure transient tests (possible to parameterize).
  - ii. Set up WFT tool for its modular configuration and volume calculations. Verify the measurement depths of water-cut and bottomhole pressure for the multisegment well model.
3. Perform sensitivity and optimizer runs with parameters:
  - i. Establish ranges for input parameters as realistic as possible from openhole logs and WFT pressure transient analyses, (i.e. IPTT).
  - ii. Run simulation cases and conduct history matches with mismatch parameters.
4. Analyze results provided by the optimizer:
  - i. Examine the model match for observed vs. modeled with the help of global objective values.
  - ii. Obtain confidence intervals of individual parameters.
  - iii. Perform statistical evaluation methods for goodness of fit and check the uniqueness of individual parameters.
5. Rerun the simulation with final parameters and observed datasets to confirm the history match.

Figure 5.1 depicts the workflow of the stochastic based optimization process.



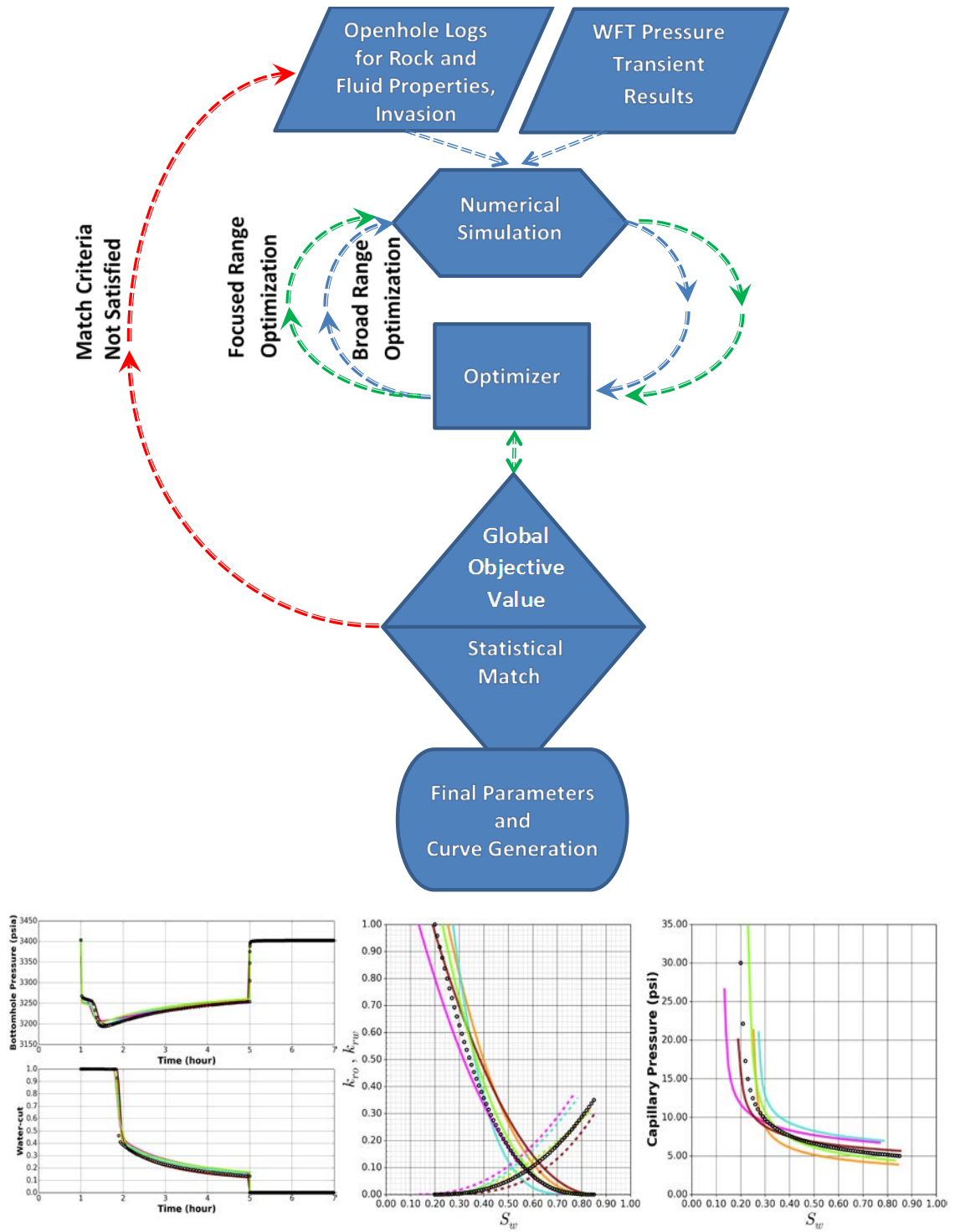


Figure 5.1: Diagram of the stochastic based optimization process.

## 5.1 Analysis of Openhole Logs

Reservoir properties of the uninvaded zone away from the wellbore are required to set reservoir initial conditions; therefore logging tools should measure beyond the invaded zone in the reservoir. Alternatively, interpretation techniques must be able to compensate for the near-wellbore mud-filtrate contamination. When possible with the physics of the measurement, the logging tools should have a significant depth of investigation. When the physics of the measurement prevents a deep investigation, the interpretation techniques must deal with the mud-filtrate invasion. The mud-filtrate invasion creates a flushed zone, but it may not flush the entire hydrocarbon saturation to residual as explained earlier in Chapter 4. The invaded zone creates a transitional zone before reaching to the initial undisturbed reservoir conditions, which exhibits a challenge for obtaining  $S_{wi}$  and  $S_{or}$  values. The interpretation techniques are applied for approximation of saturation values since the flushed zone saturation,  $S_{xo}$  may not be equal to  $S_{or}$ , and  $S_{wi}$  measurement requires an analysis beyond the invaded zone (Log Interpretation Principals / Applications, 1989).

Triple combo (Gamma-Ray, Neutron, Density, and Resistivity) logs can be used regularly in clastic reservoirs. Lithology and porosity can also be evaluated from the nuclear logs, such as Gamma-Ray, Neutron, Density, and Photo Electric Factor (PEF). Clastic pore geometry and lithology are generally correlated. Absolute permeability may also be associated to lithology. Saturations of the uninvaded and invaded zones can be obtained from resistivity logs with the Archie equation and the effect of clays can be incorporated in clastic reservoirs.

On the other hand, carbonate reservoirs show several challenges: Carbonate pore geometry and lithology generally do not correlate. Permeability does not have a trend with mineralogy. Saturation becomes challenging since Archie exponents,  $m$  and  $n$ , are not correlated to either mineralogy or porosity. Evaluating mineralogy is relatively easy with PEF except when anhydrite occasionally appears. Total porosity is solved with lithology, density, neutron, and NMR porosity if available. NMR porosity is later partitioned into several pore geometry components for an absolute permeability estimate, which is calibrated using WFT data.

Capillary pressure curves for a primary drainage process can be obtained from NMR logs. NMR pore partitions solve saturation distribution using the deep and shallow resistivity logs. Flushed zone saturations can be verified independently from resistivity logs by using Sigma, Dielectric or NMR logs if available. Dielectric logs can provide Archie exponents. This method will assist in improving the resistivity based saturation estimates (Ramamoorthy *et al.*, 2008).

Openhole logs are recorded during the mud-filtrate invasion in an imbibition process. Their interpretation can deliver the invasion fluid volumes and the depth of invasion (DOI) at the time of logging. It has been demonstrated that array resistivity measurements, either induction or laterolog, can be used to establish the radial advancement of the invasion profile (Ramakrishnan *et al.*, 1997). Array resistivity logs can be applied to estimate the imbibition fractional flow and relative permeability curves either from 1D (Capillary pressure and gravity terms are not included.) or 2D (Capillary pressure and gravity terms are included.) inversion.

The 1D invasion flow model is based on two-phase (water and hydrocarbon) and three-component (oil, water, and salt) radial transport (Ramakrishnan and Wilkinson, 1997). Array resistivity logs are used to characterize the invasion profile with an assumption that a single snapshot of radial conductivity variation is sufficient to reconstruct the multiphase flow behavior of the formation. The model is described by the two-phase Darcy equation by ignoring capillary pressure and gravity terms. The inversion results can provide fractional flow curves as a function of saturation, and filtrate loss per unit depth.

The 2D invasion flow model improves the 1D model by incorporating the capillary pressure and gravity terms (Liang *et al.*, 2011). The model numerically solves the mud-filtrate invasion process and uses the WFT pressure transient data. The mud-filtrate invasion, although it is uncontrolled, is treated as a water injection process into the hydrocarbon-bearing formations. The 2D fluid flow problem is described by a two-phase, three-component (oil/gas, water, salt) transport model. The numerical simulation solves the Darcy's equation for two-phase and salt concentration with the brine tracking option in a fully implicit black-oil simulator.

The openhole log interpretation for the mud-filtrate invasion and saturations is an optional process for our workflow. However, if the openhole log interpretation is available, it can decrease uncertainties on saturations and invasion volumes, which in turn reduces counts of parameters and sensitivity runs. This is especially important if saturation endpoints are established from the openhole logs since they may become less sensitive in some cases. Commercial software packages, such as Techlog and GeoFrame are used for openhole log interpretations (Techlog and GeoFrame User Manuals, 2015).

## **5.2 Preparation of Simulation Dataset**

A fully implicit black-oil simulator (ECLIPSE Reservoir Simulator Technical Description, 2015) is used for numerical runs. The numerical simulation dataset is prepared with the inputs from fluids, petrophysical and geological properties as well as from the WFT tool geometry and the WFT observed data in several days. Most Petrophysical and IPTT inputs are assumed ready a priori from interpretations of all other available logs and data. The inlet volumes are honored and the fluid segregations are accounted for. The mud-filtrate invasion consists of DF and SF periods. Field time records of drilling, logging and WFT cleanup are implemented in order to design the invasion accurately. The depth of invasion is parameterized and the volume of invasion, if known, is respected. Fluid contacts and saturation distribution are initialized according to the petrophysical model. For simplicity, properties of the mud filtrate and the formation water are kept identical. WFT pressure transient test analyses for horizontal and vertical permeabilities are incorporated into the dataset. If absolute permeabilities are not known, they can be also put in the iteration loop to be estimated. The effective oil permeability obtained from the WFT pressure transient analysis is later distributed to the reservoir for correct heterogeneities with a trend obtained from either WFT pretest mobilities or log driven permeabilities, such as NMR logs. Skin factor is always parameterized since knowing each skin component is relatively difficult in a multiphase flow environment. A single set of relative permeability and capillary pressure curves for both invasion and cleanup is used unless mentioned specifically that hysteresis is applied. WFT flow rates are strictly followed and forward optimization runs are conducted to be able to match water-cuts and bottomhole pressures recorded during the WFT cleanup.

### 5.3 Design of Optimization

As an optimization engine, a commercial software package for assisted history matching is used in the workflow (MEPO User Manual, 2015). The software uses a stochastic based optimization (SBO) to reduce the difference between observed data and simulated responses as quantified by an objective function. A standard least-squares objective function is implemented in the workflow. The objective function consists of two mismatch contributions: water-cut and bottomhole pressure. Depending on the optimization strategy employed, the objective function is evaluated in a number of sampled points covering the input parameter space. A random sampling strategy such as Latin Hypercube sampling (LHS) (McKay *et al.* 1979) or an evolution strategy (ES) is applied. The LHS process screens the entire parameter ranges in defined compartments and prepares forward runs. The ES process modifies individual parameters in every generation of forward runs and exchanges them in the following generation. While the LHS process executes all the prepared forward runs, the forward runs in the ES process progress depending on the achievement of the match criteria. Both strategies provide a match when the global objective function value is at its minimum.

While avoiding the need for gradient information, stochastic optimization methods require a relatively large number of objective function evaluations, where each evaluation in itself requires a forward simulation run. However, they have significant advantages in terms of flexibility in the choice of parameters to optimize and ability to converge to a global optimum. Also, as they are often based on a population concept with multiple parents/children in a generation, many simulations can be run concurrently, whereas gradient based methods are inherently more sequential in nature (see Chapter 2.9).

The inversion process uses a stochastic optimization methodology allowing relative permeability and capillary pressure parameters to be inverted concurrently. Although any parameterization method can be implemented, MBC and LET parameterizations are used for the relative permeability curves and the MBC parameterization is chosen for the capillary pressure curve. The optimization includes parameters, such as relative permeability and saturation endpoints, pore-size distribution index and displacement pressure for capillary pressure, damage skin, horizontal and vertical permeabilities, and invasion volumes and durations for DF and SF to establish the depth of invasion. The endpoint saturations and invasion profile can be input from openhole log interpretations

or they can be optimized as well. Horizontal and vertical permeabilities and damage skin can be fixed or included in the optimization. In general, because parameters may correlate with each other, when fewer optimization parameters are chosen, fewer simulation runs are required and higher confidence levels are obtained for the resulting parameters.

#### **5.4 Analysis of Optimization Runs**

SBO is the chosen method for the relative permeability and capillary pressure analysis due to advances of computer clusters and their computational cost in SBO, and avoiding local minima and software limitations in GBO. However, GBO is also presented for clarity. SBO and GBO methods use different commercial software packages. The former uses MEPO (MEPO User Manual, 2015), while the latter uses SIMOPT (SIMOPT User Manual, 2015) software packages. Both optimization techniques share a fully implicit black-oil simulator (ECLIPSE Reservoir Simulator Technical Description, 2015) for numerical runs.

SIMOPT software for GBO can communicate with the simulator by means of altering parameter multipliers in the dataset directly. GBO runs depend on the number of predefined parameter multipliers available in the simulator keywords; however, the lack of certain parameter multipliers, such as relative permeability and capillary pressure curvatures, limits the design of numerical runs (See Appendix A). Initially the study was started with the GBO approach, but due to limiting parameter multipliers, it was shifted to the SBO method, and GBO examples were presented for comparison.

The main advantage of MEPO software for SBO is its flexibility to define the input parameters directly in the numerical simulator dataset for each run. MEPO uses Python (Lutz, 2010) programming scripts to generate ECLIPSE datasets and controls the runs and analyzes the results. In general, SBO run counts are more than GBO runs, but the SBO method allows multiple concurrent runs with available computer clusters, and the flexibility of altering the simulator dataset provides a complete freedom during the design of forward runs.

#### ***5.4.1 Analysis of Gradient Based Optimization***

GBO is performed by switching the gradient option in the black-oil simulator (ECLIPSE Reservoir Simulator Technical Description, 2015), which uses the endpoint scaling (EPS) option to parameterize relative permeabilities and capillary pressures. The EPS option allows modifying the endpoints of the relative permeability and capillary pressure curves while interacting with the gradient based optimizer (SIMOPT User Manual, 2015). The gradient option of the simulator provides gradients of the water-cut and the bottomhole pressure with respect to the parameters chosen. The GBO software then uses the gradients provided by the numerical simulator to achieve a logical regression during a history match, updating the property parameters by modifiers and calling the numerical simulator. It is observed that although local optima may be reached in some cases depending on the parameter search direction, the GBO method is faster than the SBO method and comparatively fewer regressions are required to reach to a solution.

GBO is a fast optimization technique due to its minimization methodology; however, GBO in the SIMOPT software does not have parameters to define mud-filtrate invasion, damage skin, curvatures of the relative permeability and capillary pressure curves. Damage skin has to be known or interpreted before the optimization. This may require an additional pressure buildup after WFT cleanup. Damage skin can be introduced as a reduction of permeability at the near wellbore region by applying a transmissibility multiplier similar to Hawkins' definition to skin factor. The depth of invasion cannot be used as an optimization parameter and it is fixed before the optimization. Sensitivities of the damage skin and the invasion may be conducted manually by assigning these two parameters. The most limiting factor of GBO with these commercial products is the fact that the numerical simulator does not have a way to define the Corey exponents or any other relative permeability model parameters. This means that the curvatures of the relative permeability curves have to be known before the optimization as well. This is a software limitation selected rather than the GBO method.

The GBO method is terminated for the SBO method unless a new GBO routine is rewritten for the GBO limitations mentioned. However, for the clarity of the points made, two synthetic GBO examples are presented in Appendix A.

#### 5.4.2 Analysis of Stochastic Based Optimization

SBO is implemented with a commercially available software (MEPO), which has a flexible setup of defining parameters, generating relative permeability and capillary pressure curves with the help of user provided software codes, as explained earlier. The SBO method then generates a list of simulation runs designed by LHS strategy, which is the preferred strategy initially since it screens the entire parameter ranges to assemble a plausible collection of the parameter values. The LHS strategy is generally followed by another LHS strategy in which known parameters are eliminated and ranges for unknown parameters are tightened. The simulation model is updated automatically with new values of parameters. Each additional parameter may require extra 100-300 SBO runs. The result of each forward run is history matched, and partial objective values are generated with water-cuts and bottomhole pressures. The global objective value is then constructed by a summation of the partial objective values. Following three different methods are applied for generating final parameters of relative permeabilities and capillary pressures.

The first method uses *single parameter trends*. SBO runs are conducted for the parameter ranges chosen in an LHS strategy. Least squares based objective function values are calculated from each run to determine the goodness of the history matching. Partial or global objective values from all SBO runs are plotted against the optimized range of the single parameter on a logarithmic scale. This method focuses on a single parameter at a time and the plots are repeated for each parameter. The method requires care that each parameter may not have an impact on the objective value independently during the history matching, or non-uniqueness may occur if some parameters are correlated with others. However, the lowest global objective function value for the particular parameter on the plot will provide a trend, which may present a solution or narrow down the parameter range in a search direction.

The second method benefits from *objective function values*. In an ideal scenario is that the LHS strategy samples the entire field frequently for each parameter and provides enough SBO runs although this requirement may take a large number of runs. Partial and global objective function values are then tabulated in the order from the lowest to the highest for each optimization run. In this case, a single run with the lowest global objective value (or the partial objective value depending on its weight function) should



be the best history match with its collective set of parameters. In this method, one run is the best match with its entire set of parameters and followed by other runs depending on their global or partial objective value.

In some cases SBO runs present that both methods have limitations, such as interdependency of parameters in the first method or a number of run requirements due to many parameters on the second method. Therefore, a hybrid approach is suggested as a third method. In this case, *single parameter trends with relaxed margins* are used for a search direction. The first and the second methods are always conducted and their consistencies are checked before the third method. This is a search method of the runs that are already performed and it does not require further forward runs. An additional search is conducted on the parameters in the completed runs by relaxing their margins. The method also applies a cutoff for the partial objective values so that the values do not increase beyond a limit while relaxing the margins of a single parameter. The runs falling into the category are plotted together to observe their history matches and the relative permeability and capillary pressure curves. The approach keeps relatively low partial objective values and provides a trend with a larger band on the relative permeability and capillary pressure curves, and the history matches, in which a true solution may be expected. This option should be used as a last resort, it does not provide a single match, but it may rather give a band for each curve.

As an example to select the forward runs for *swi* parameter in the third method, an interval search is defined as  $(swi_{min} - swi_{min} * \text{margin}\%), (swi_{max} + swi_{max} * \text{margin}\%)$ . Generally, this method requires more than one parameter with its relaxed margin in order to select additional runs. The method helps comparing the first and the second methods and looks into individual parameters versus individual runs with entire sets of parameters. This method plots the curves prepared from the collective parameters of each run as in the second method but uses a relaxed range for the parameters where the optimal ranges of the parameters are widened.

The first two methods are almost always applied sequentially to obtain the designed parameters from the forward runs. Generally, if a sufficient amount of forward runs are conducted with respect to the parameter counts, the first two methods should yield similar results. If the first two methods do not deliver desired results for the parameters, then the

third method provides a value range for each parameter, which may be treated as a confidence interval of its expected solution. Therefore, the analysis should start with the first two methods, and if not satisfactory, then the third method is also executed. Appendix B.2 should be visited for the use of the three methods stated here. Appendix B.2 presents a hierarchical approach starting from the first method until the third, and compares the results.

## **5.5 Synthetic Examples**

Synthetic GBO and SBO examples are prepared for oil reservoirs with WBM filtrate invasions. As described earlier, the SBO method is the preferred method for the study; however, the synthetic GBO examples are kept as a reference in Appendix A from which a future study may be developed.

The three synthetic SBO examples are presented in Appendix B in order to develop and explain the methods described in this chapter. The synthetic examples B.1 to B.3 have the same operational setup and model properties, and ignore capillary pressures. The DP inlet is used with the multisegment well model to account for the internal storage volume between the packers. The SBO examples have successively more difficult conditions. Example B.1 has seven unknown parameters with known saturation endpoints from openhole logs. Example B.2 has nine unknown parameters including saturation endpoints. Example B.3 introduces noisy observed datasets with nine unknown parameters. The LET relative permeability parameterization is used in these examples. The analyses are developed from relatively easier to more difficult cases without capillary pressures. Later capillary pressures are added into analyses as in the following synthetic example in Chapter 5.5.1.

The following synthetic SBO example uses a different set of operational setup and model properties from the SBO examples in Appendix B. Relative permeabilities and capillary pressures are estimated during the optimization. The synthetic example is similar to field cases and paves the way how to approach and optimize actual field cases.

### 5.5.1 Stochastic Based Optimization Synthetic Example

The synthetic SBO example includes the optimization of relative permeabilities and capillary pressures as well as DF and SF rates and their durations. The DF rate is designed with the power law decay as  $dynq \times time^{-0.5}$  where *time* is incremental from the start to *dynt*. DF is followed by SF during the invasion as described in Chapter 2.1. The SF rate (*statq*) is included as a constant. SF is properly designed such that it does not occur across the sealed elements and the intakes of the inlets during the cleanup, but SF occurs elsewhere in the reservoir.

The MBC parameterization is used in this exercise. Relative permeability curvature exponents for oil (*no*) and water (*nw*), saturation and permeability endpoints (*swi*, *sor*, *koro*=1, *korw*), damage skin (*SKIN*) are implemented. The invasion parameters, DF duration (*dynt*), DF rate multiplier (*dynq*), and SF rate (*statq*) are studied in order to model the invasion profile accurately. The capillary pressure curve is designed with two parameters: entry pressure (*pd*), and pore-size distribution index (*lmb*).

The model has the following known parameters: horizontal and vertical permeabilities, fluid and rock compressibilities, fluid viscosities, porosity, oil relative permeability value at the irreducible water saturation (*koro*), and total invasion duration (*totalt*) since the dates of drilling and WFT cleanup are recorded.

The model has the following unknown parameters: damage skin, relative permeability and saturation endpoints and the curvature exponents, except *koro*, capillary pressure parameters of entry pressure and pore-size distribution index, invasion profile parameters including dynamic and static filtration rates and their durations. The unknown optimization parameters are: *swi*, *sor*, *korw*, *nw*, *no*, *pd*, *lmb*, *SKIN*, *statq*, *dynq*, *dynt*. *koro* is set to unity.

Tables 5.1 through 5.4 detail the numerical simulation setup. Figure 5.2 depicts the radial gridding in an R-Z cross-sectional view. The DP inlet is designed with the multisegment well model. Figure 5.3 displays the water saturation profile during the mud-filtrate invasion and the cleanup.

Table 5.1: Parameters of invasion, cleanup and pressure buildup are listed in the synthetic SBO example. The cleanup rate is for the circular radial grid.

Properties	Input	Unit
Dynamic filtration duration, $dynt$	0.5	day
Static invasion influx rate, $statq$	0.0150	stb/day/ft <sup>2</sup>
Cleanup start time	3.5	day
Cleanup duration, $t_{cleanup}$	4	hr
Cleanup rate, $q_{cleanup}$	53	L/hr
Pressure buildup duration, $t_{PBU}$	2	hr

Table 5.2: Reservoir properties of the synthetic model in the synthetic SBO example.

Properties	Input	Unit
$h$	53.00	ft
$h_w$	3.333	ft
$z_w$	47.57	ft
$r_w$	0.354	ft
$R$	816	ft
$k_h$	20.00	md
$k_v/k_h$	0.60	
$Skin$	2.00	
$c_r$	1.25e-6	psi <sup>-1</sup>
$P_i$	3403.6	psia
$\emptyset$	0.30	fraction
$S_{wi}$	0.20	fraction
$S_{or}$	0.15	fraction
$n_w$	2.50	
$no$	2.80	

Table 5.3: Fluid properties of the synthetic model in the synthetic SBO example. The fluid viscosities and densities are at downhole and surface conditions respectively.

Properties	Input	Unit
$\mu_o$	0.75	cP
$\mu_w$	0.55	cP
$c_o$	10.24e-6	psi <sup>-1</sup>
$c_w$	3.0e-6	psi <sup>-1</sup>
$\rho_o$	0.865	g/cc
$\rho_w$	1.153	g/cc

Table 5.4: Grid properties in the synthetic SBO example.

Properties	Count
Cell	71496
DR	216
DØ	1
DZ	331

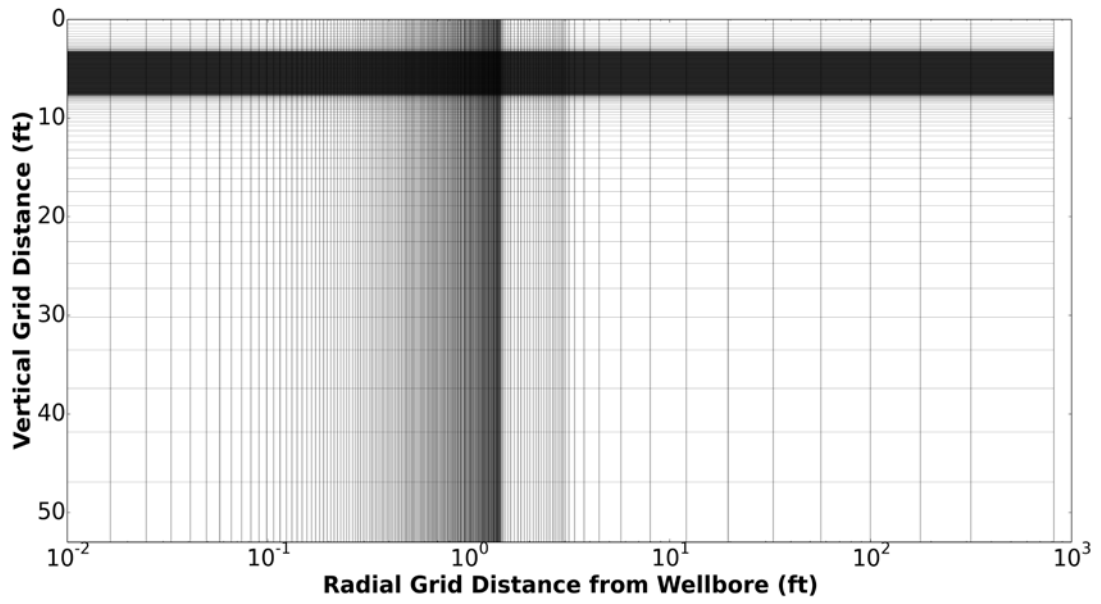


Figure 5.2: Radial gridding of the synthetic SBO example is displayed in an R-Z cross-sectional view.

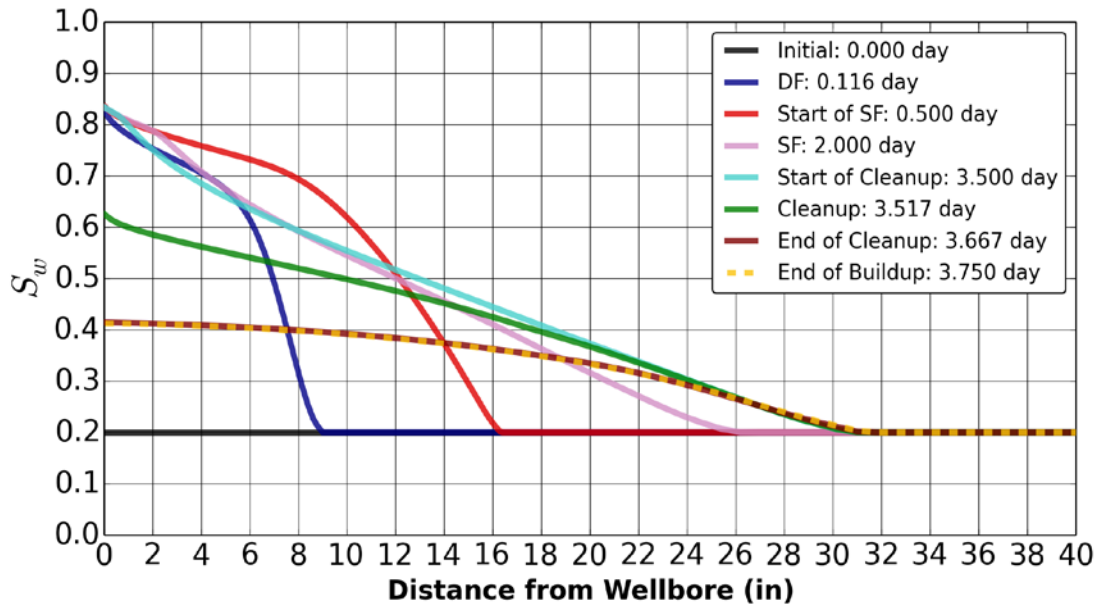


Figure 5.3: Water saturation progress of the mud-filtrate invasion and the cleanup in the near-wellbore region at the center of the DP interval for the model used in the synthetic SBO example.

### 5.5.1.1 Analysis of Single Parameter Trends

Global or partial objective function values of forward runs in each cycle are plotted against their single parameter values on a semilog scale (see Chapter 5.4.2 and Appendix B for details). A parameter is realized ideally from its lowest objective function value in a minimization process. An optimal range represents a visually obtained range for each parameter when evaluated against objective function values. The optimal range provides lower and upper bounding inputs in the following cycle. Loosely speaking, it can be used as a confidence interval for that parameter. If the optimal range is a very narrow range, a solution is reached with a confidence interval. If the optimal range is a large range, the solution presents uncertainties, and further forward runs are conducted in a following cycle after narrowing the ranges of the parameters displaying minimization trends.

The first optimization cycle has very broad ranges of parameters to study their trends. The first cycle has a total of 4000 LHS strategy runs. Then, the second cycle having additional 2000 LHS strategy runs are conducted with narrower ranges of parameters accomplished from the first cycle. The forward run counts in the cycles are increased in order to reduce the uncertainties in the results created by the extensive amount of parameters. The computational time for each run is approximately 15 minutes and 64 parallel runs are employed.

The ranges of the parameters in the first cycle are finalized from Figure 5.4 and summarized in Table 5.5. Figure 5.4 presents that the optimal ranges of the partial objective values have uncertainties around the observed or true values. *SKIN* shows a clear minimization trend estimated from both partial objective values. Ranges of *swi* and *sor* are minimized from WCUT. A range of *korw* can be obtained from both WCUT or WBHP. WBHP and WCUT are the partial objective values of bottomhole pressures and water-cuts, respectively. *nw* and *no* have large uncertainties. *dynq*, *dynt*, *statq* show minimization from both partial objective values, while *lmb* and *pd* do not display large minimization.

All the parameters are included in the second iteration cycle, either with narrower or same ranges obtained from the first cycle. The additional runs, although they have different parameter ranges, are combined with the first cycle runs and displayed in Figure 5.5. The optimal ranges of the parameters in the second cycle are finalized from Figure 5.5 and

summarized in Table 5.6. The second cycle shows that the results of the parameters are improved, and the final results can be accepted with the confidence intervals of the parameters. The final parameter value and Error% are presented in the final cycle in the tables. Error% is calculated with the optimal ranges and observed values. The columns highlighted as gray display the inactive (known) parameters in the tables. The resulting relative permeability and capillary pressure curves are illustrated with their optimal ranges and compared with the true curves in Figure 5.6.

Table 5.5: Ranges of the parameters are obtained from the analysis of single parameter trends in the first cycle of the SBO example. The parameters are not fixed for the next cycle. The results are finalized from Figure 5.4.

	<i>swi</i>	<i>koro</i>	<i>sor</i>	<i>korw</i>	<i>nw</i>	<i>no</i>	<i>lmb</i>	<i>pd</i>	<i>SKIN</i>	<i>dynq</i>	<i>dynt</i>	<i>statq</i>	<i>totalt</i>
<sup>1</sup> Observed	0.200	1.000	0.150	0.350	2.500	2.800	2.807	5.000	2.000	0.066	0.500	0.015	3.500
<sup>2</sup> Lower	0.050		0.050	0.100	1.000	1.000	1.000	0.100	0.000	0.030	0.100	0.005	
<sup>2</sup> Upper	0.350		0.350	0.600	5.000	5.000	10.000	9.000	10.000	0.100	1.000	0.030	
<sup>3</sup> Final													
<b>Optimal Range</b>	0.139, 0.282		0.142, 0.242	0.256, 0.400	1.629, 4.127	1.925, 3.816	1.995, 5.154	2.862, 6.974	1.570, 4.438	0.052, 0.086	0.231, 0.851	0.013, 0.019	

Table 5.6: Ranges of the parameters are obtained from the analysis of single parameter trends in the second cycle of the SBO example. The results are finalized from Figure 5.5.

	<i>swi</i>	<i>koro</i>	<i>sor</i>	<i>korw</i>	<i>nw</i>	<i>no</i>	<i>lmb</i>	<i>pd</i>	<i>SKIN</i>	<i>dynq</i>	<i>dynt</i>	<i>statq</i>	<i>totalt</i>
<sup>1</sup> Observed	0.200	1.000	0.150	0.350	2.500	2.800	2.807	5.000	2.000	0.066	0.500	0.015	3.500
<sup>2</sup> Lower Input	0.139		0.142	0.256	1.629	1.925	1.995	2.862	1.570	0.052	0.231	0.013	
<sup>2</sup> Upper Input	0.282		0.242	0.400	4.127	3.816	5.154	6.974	4.438	0.086	0.851	0.019	
<sup>3</sup> Final	0.212		0.151	0.320	2.145	2.582	3.034	4.985	2.013	0.068	0.489	0.014	
<b>Optimal Range</b>	0.193, 0.239		0.142, 0.238	0.320, 0.363	2.000, 3.200	2.256, 3.033	2.643, 4.144	3.974, 4.985	1.877, 3.468	0.060, 0.072	0.445, 0.572	0.014, 0.017	
<sup>4</sup> Error%	3.5, 19.5		5.3, 58.7	8.6, 3.7	20.0, 28.0	19.4, 8.3	5.8, 47.6	20.5, 0.3	6.2, 73.4	9.1, 9.1	11.0, 14.4	6.7, 13.3	

<sup>1</sup>Observed values refer to as the setup or true parameters of the synthetic example.

<sup>2</sup>Lower and Upper Inputs are the bounding parameter values updated from Optimal Range of a parameter from the previous cycle result.

<sup>3</sup>Final is the optimization result of a parameter in the cycle.

<sup>4</sup>Error% = |(Observed-Optimal Range)|\*100 / Observed.

The columns highlighted as gray represent the parameters that are fixed and not optimized.

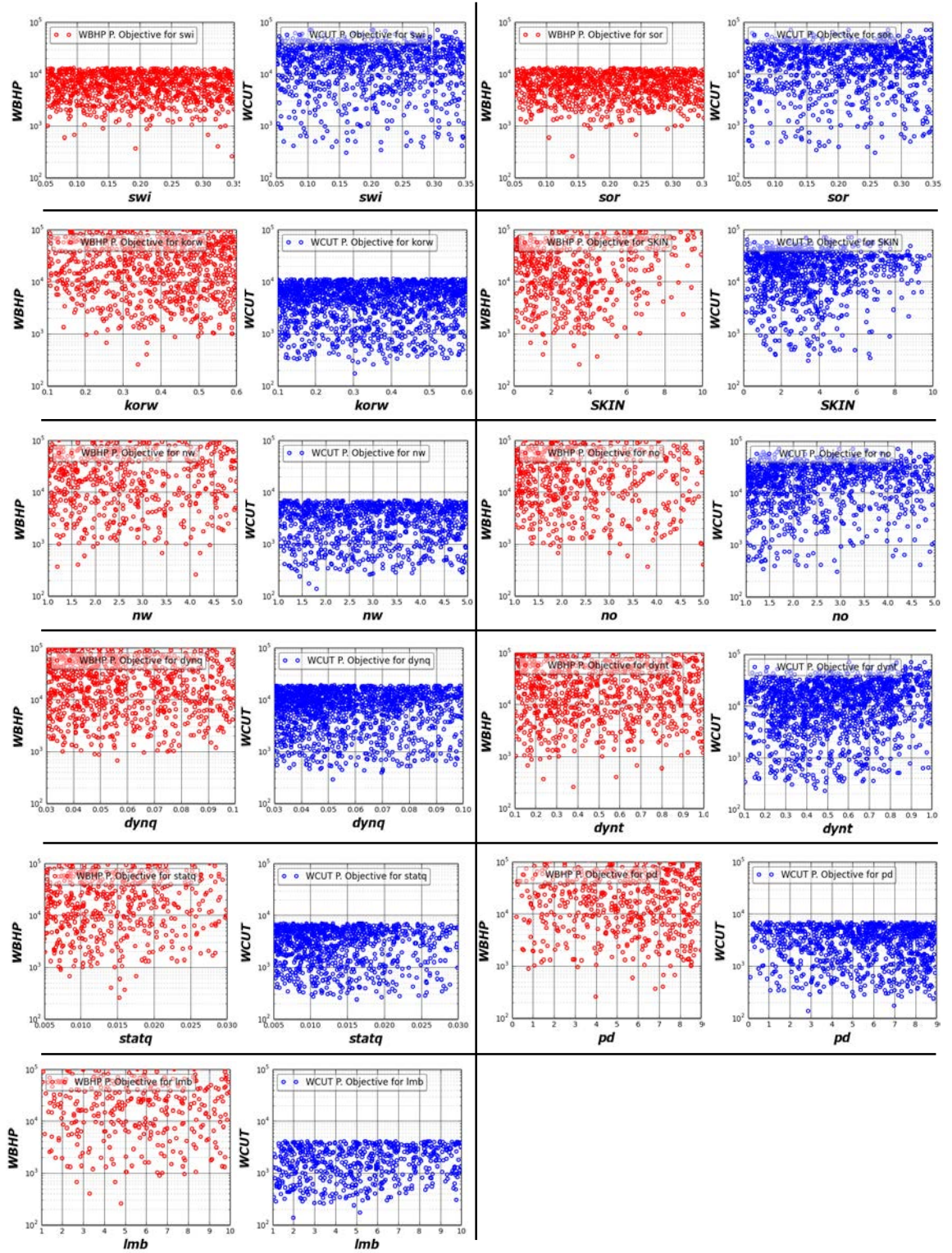


Figure 5.4: Partial objective functions are plotted against the individual parameters. Table 5.5 summarizes the first cycle results from the single parameter trends.



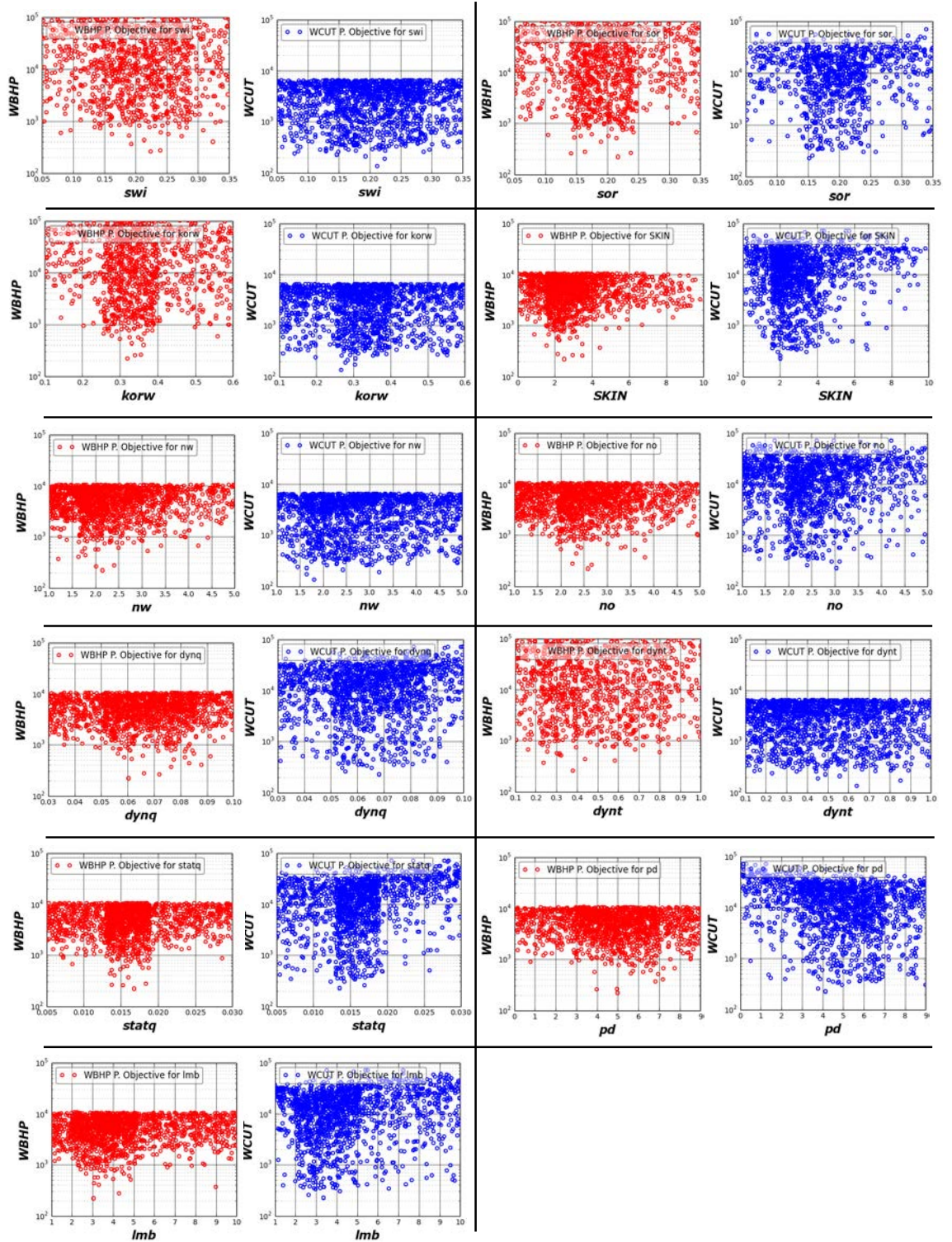


Figure 5.5: Partial objective functions are plotted against the individual parameters. Table 5.6 summarizes the second cycle results from the single parameter trends. The second cycle is conducted with the narrower ranges of the parameters obtained from the first cycle analysis.

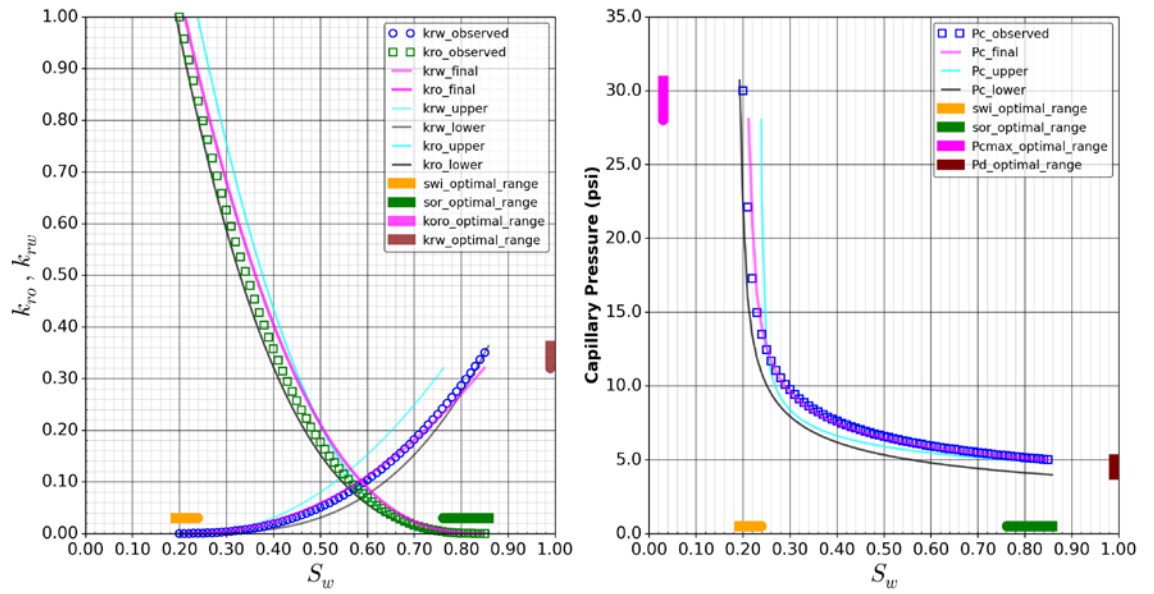


Figure 5.6: Relative permeability curves and capillary pressures are estimated with their optimal ranges from the single parameter trends in the second iteration cycle.

#### 5.5.1.2 Analysis of Objective Function Values

Importance of weighting global objective function (GOF) values is exercised in the following analyses. The entire LHS strategy runs are ordered from the lowest to the highest with respect to GOF values. Partial objective function (POF) values are weighted to obtain GOF values as:  $a \cdot \text{WBHP} + b \cdot \text{WCUT}$ .  $a$  and  $b$  are arbitrary weight factors, and WBHP and WCUT are the partial objective values of bottomhole pressures and water-cuts. Table 5.7 illustrates the lowest five GOF values without altering their weight multipliers; hence,  $a$  and  $b$  are both one. Figure 5.7 and 5.8 show the relative permeability and capillary pressure curves, and the history matches of the runs respectively as listed in Table 5.7.

Table 5.7: LHS forward runs having the lowest five GOF values are listed. WBHP and WCUT are not weighted in this section;  $a$  and  $b$  are both equal to one.

IT*	DS*	swi	sor	korw	nw	no	lmb	pd	SKIN	dynq	dynt	statq	totalt	GLOBAL	WBHP	WCUT
11	1745	0.146	0.151	0.306	1.648	3.033	3.343	4.135	2.013	0.068	0.489	0.014	3.500	19565	4642	14923
11	758	0.150	0.157	0.268	2.077	2.405	2.643	3.764	2.021	0.055	0.445	0.017	3.500	19762	2774	16988
11	1753	0.218	0.239	0.307	1.750	3.099	4.144	4.934	1.877	0.065	0.331	0.014	3.500	23876	4065	19811
11	1706	0.251	0.167	0.332	2.485	1.947	2.901	4.491	2.591	0.062	0.572	0.016	3.500	24398	1407	22990
11	1533	0.153	0.173	0.361	2.306	2.622	3.957	5.273	2.841	0.060	0.452	0.014	3.500	24427	1365	23061

\*IT and DS refer to as iteration and dataset respectively.

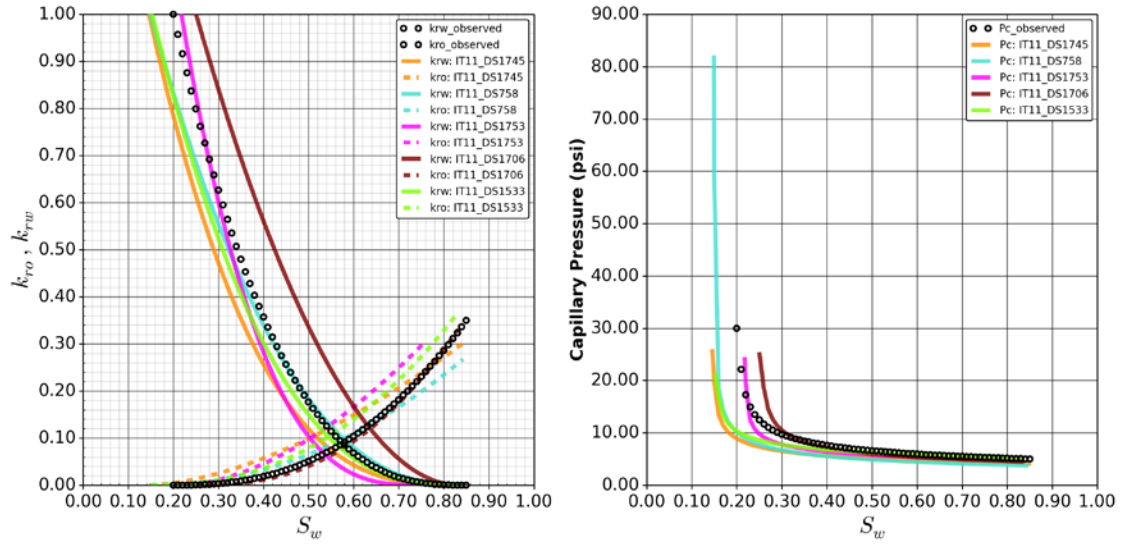


Figure 5.7: Relative permeability and capillary pressure curves from the LHS forward runs having the lowest five GOF values are plotted. The runs are listed in Table 5.7.

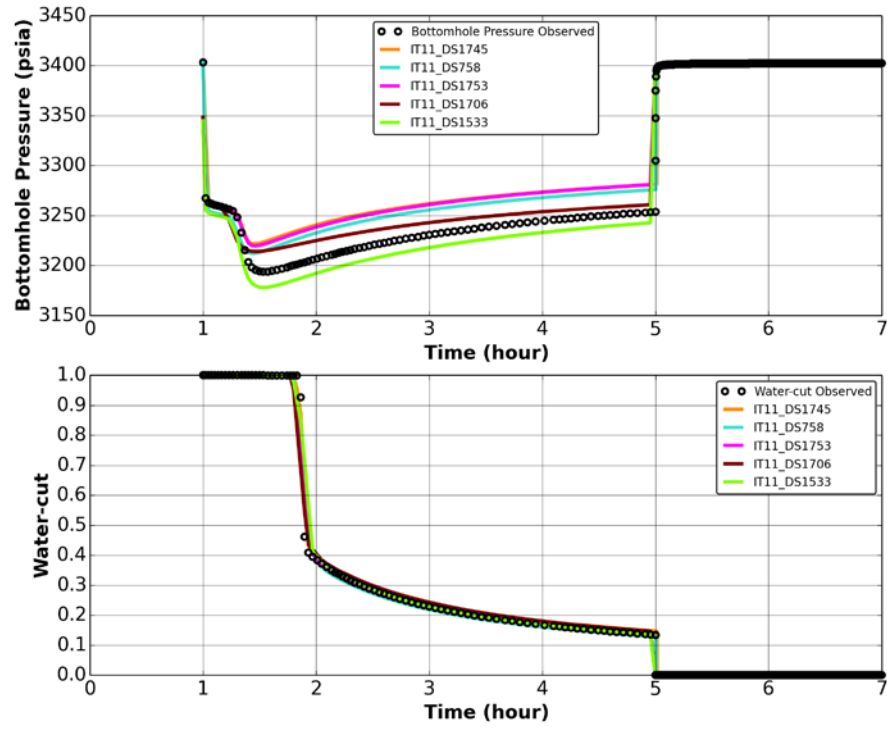


Figure 5.8: History match results from the LHS forward runs having the lowest five GOF values as listed in Table 5.7.

In the next case,  $a$  and  $b$  are set to 1.0 and 0.01 respectively. This gives an extra weightage over WBHP. All GOF values are recalculated from  $a*WBHP + b*WCUT$ . The runs are ordered again from the lowest to the highest with respect to GOF values and listed in Table 5.8. The runs with the lowest five GOF values are plotted for the relative permeabilities and capillary pressures in Figure 5.9 and for the history matches in Figure 5.10.

Table 5.8: POF values of bottomhole pressures (WBHP) and water-cuts (WCUT) are weighted with  $a$  and  $b$ , which are set to 1.0 and 0.01 respectively. The resulting GOF values are listed from the lowest to the highest values.

IT*	DS*	swi	sor	korw	nw	no	lmb	pd	SKIN	dynq	dynt	statq	totalt	GLOBAL	WBHP	WCUT
11	1405	0.253	0.157	0.325	2.006	2.438	3.091	3.882	2.831	0.059	0.316	0.018	3.500	816	559	257
11	1396	0.274	0.215	0.358	1.718	3.601	4.849	6.956	2.243	0.078	0.322	0.014	3.500	957	505	452
11	519	0.134	0.231	0.372	2.309	2.032	4.082	6.720	3.032	0.076	0.533	0.016	3.500	1132	757	375
11	531	0.190	0.147	0.300	3.128	2.004	4.012	5.641	2.226	0.062	0.314	0.015	3.500	1133	520	613
11	145	0.231	0.170	0.304	1.819	2.652	2.437	4.406	2.389	0.078	0.721	0.017	3.500	1193	796	397

\*IT and DS refer to as iteration and dataset respectively.

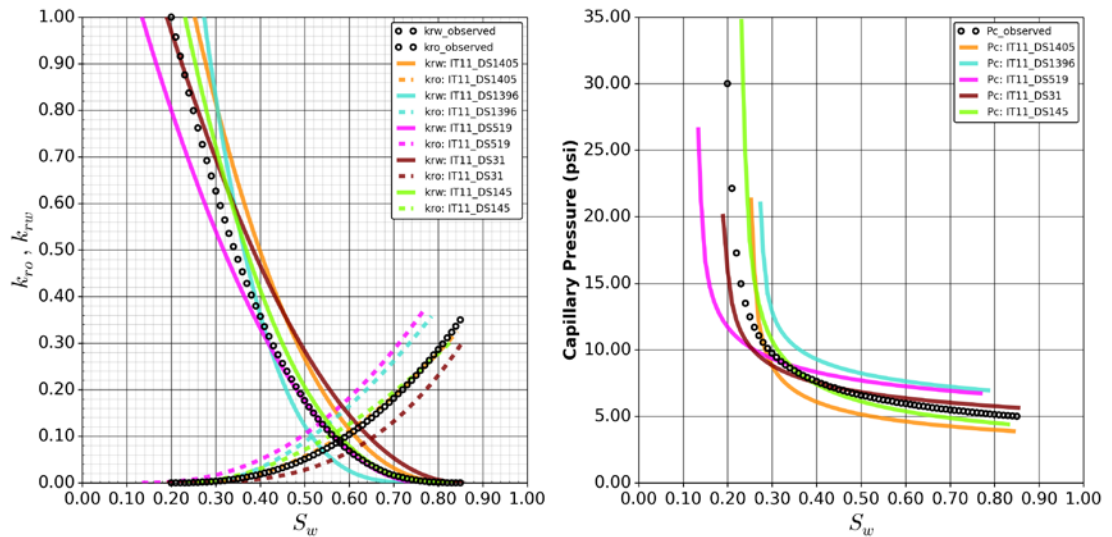


Figure 5.9: Relative permeability and capillary pressure curves from the LHS forward runs having the lowest five GOF values obtained from the calculation of  $1*WBHP + 0.01*WCUT$  are plotted. The runs are listed in Table 5.8.

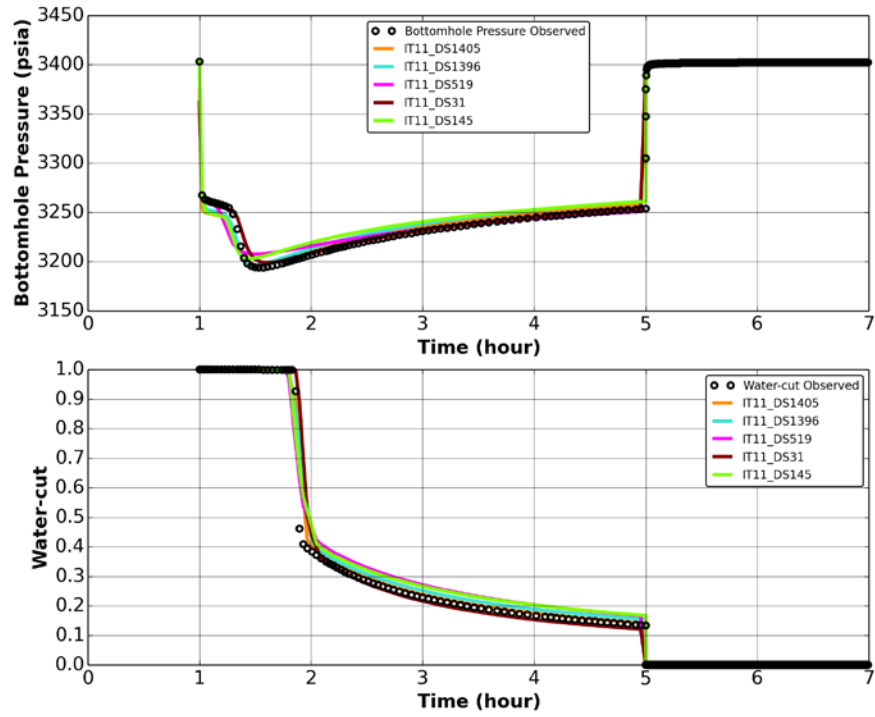


Figure 5.10: History matches from the runs having the lowest five GOF values obtained from the calculation of  $1 \cdot \text{WBHP} + 0.01 \cdot \text{WCUT}$  as listed in Table 5.8.

Although the final results may show some non-uniqueness from the history matches, the resulting relative permeability and capillary pressure curves are within a range, which may be considered as a confidence interval. Known saturation endpoints, if interpreted from openhole logs, can further improve the results obtained in such cases.



## 5.6 Field Examples

Four field examples published in SPE conferences are presented in Appendix C. The field examples employ the stochastic based optimization. The examples show a variety of applications from carbonate to clastic reservoirs, including various flow unit thicknesses, and a transitional zone. The field examples involve all major WFT inlet types, such as 3DRP, DP and SP inlets. The examples are displayed in a chronological order, and they represent the development of our study with additional features introduced in each technical paper. The first field example in Appendix C.1 does not exercise the capillary pressure optimization, but introduces the WFT 3DRP inlet for the first time. The second field example in Appendix C.2 uses the multisegment well model for the DP inlet. The third field example in Appendix C.3 introduces the capillary pressure optimization with a detailed mud-filtrate invasion model. The fourth field example in Appendix C.4 uses a single probe in a clastic reservoir.

The field example in Appendix C.1 uses the WFT 3DRP inlet and the cleanup is conducted in a transition zone of a carbonate reservoir (SPE170648). The LET and the Thomeer parameterization models are used for relative permeabilities and capillary pressures respectively. Resistivity, density and porosity logs are acquired while drilling (LWD), and resistivity micro imaging and dielectric logs are conducted with a wireline operation. An IPTT test is performed after the WFT cleanup. The example does not have a capillary pressure optimization, but rather uses the known capillary pressure curve calculated from the observations of fluid sample water-cuts, fluid densities and formation pressures in the transition zone.

The field example in Appendix C.2 has the WFT DP inlet designed with the multisegment model in an oil bearing carbonate reservoir (SPE171884). The MBC parameterization model is employed for relative permeabilities. The capillary pressure is ignored. Laterolog resistivity, nuclear magnetic resonance, dielectric, and formation imaging logs are acquired in a wireline operation. Permeabilities are analyzed from core plugs and an IPTT test. The match of DOI is achieved from the laterolog. A sensitivity study is performed by varying the final parameters one at a time around their optimum values to observe their influence over the history match. A total of 900 SBO runs are executed in the analysis of this field example.

The field example in Appendix C.3 includes the WFT DP inlet constructed with the multisegment well model in an oil bearing carbonate reservoir having a gas cap (SPE174381). The MBC parameterization model is chosen for relative permeabilities and capillary pressures. Available openhole logs are laterolog resistivity, nuclear magnetic resonance, dielectric, formation imaging. NMR derived permeabilities are combined with an IPTT test. Since the optimization includes the capillary pressure, the analysis focuses DOI and the details of DF and SF mechanisms. A total of 5000 SBO runs are performed in the study of this field example.

The field example in Appendix C.4 contains the WFT large-diameter SP inlet in a clastic reservoir (SPE177451). The MBC parameterization model is used for relative permeabilities and capillary pressures. Induction, laterolog and formation imaging logs are acquired. Saturation endpoints are obtained from the openhole logs and excluded from the optimization process. Extensive WFT pressure profiling, sampling and IPTT tests are also conducted in order to characterize the reservoir. A total of 500 SBO runs are completed in the analysis of this field example.

## **5.7 Summary of Stochastic Based Optimization Examples**

The synthetic example in Chapter 5.5.1 is designed with eleven unknown parameters, and it is very similar to common field cases. It introduces capillary pressures and detailed mud-filtrate invasion parameters. The MBC parameterization is used for relative permeabilities and capillary pressures. The SBO synthetic examples in Appendix B implement the LET parameterization for relative permeabilities. Although the MBC and LET parameterizations are used in the examples, there is no limitation to implement other parameterization methods in our study. The former is applied for water wet systems and the latter is preferred for mixed wet or oil wet systems.

A WFT dataset for a suitable study should have: a cleanup period reducing the water-cut down to, or less than 10%, and preferably a follow-up pressure buildup period for IPTT analyses. Relatively a thinner flow unit without a transitional zone and fractures is ideal for the SBO analyses. The flow unit thickness depends on the formation properties, WFT pumpout rates, the cleanup and the pressure buildup durations. Transitional zones and fractures can be incorporated into the study with detailed IPTT or openhole log analyses.

Carbonate or clastic formations do not affect the outcome of our approach as long as the formations have sufficient openhole data. A longer cleanup duration may occur in a thicker flow unit due to a larger amount of mud-filtrate movement expected vertically.

We suggest that vertical and horizontal permeabilities, and damage skin should be obtained from IPTT analyses. Due to complexity of the multiphase flow, we choose to always invert for the damage skin (see Chapter 2.5). The vertical boundaries of the flow unit should be well defined from openhole logs for IPTT analyses and numerical modeling. Assigning single values of vertical and horizontal permeabilities will underestimate the fluid flow and pressure behavior in the flow unit, and will affect the relative permeability and capillary inversion process. It is strongly suggested that the permeabilities interpreted from IPTT analyses are distributed either with correlations or log measurements in order to represent heterogeneous formations accurately. For example, porosity-permeability correlations or permeability analyses from NMR based logs can be used for this purpose.

The 3DRP probe is an ideal cleanup inlet due to a larger flow area and smaller tool storage. The DP inlet can be used with the multisegment well model with correct tool storage and flow geometry. The DP inlet design without the multisegment well model will present the hydrocarbon breakthrough time erroneously, and a large portion of water-cut data may not be suitable for history matching analyses. If formation permeabilities are relatively high (generally more than 5 md) and drawdown requirements are not strict, single probes can also be used for the cleanup and the further study.

The SBO examples show that it may be difficult to independently estimate all the unknown parameters of the problem from only bottomhole pressure and water-cut observations. Hence, a hierarchical approach for inversion is chosen. Generally DOI of the mud filtrate and the skin factor are inverted in the first cycle. This requires prior knowledge of vertical and horizontal permeabilities of the flow unit. Mud-filtrate invasion volumes from different sources, such as drilling reports or array resistivity logs can help reducing the parameter counts and improve the SBO analyses.

In some cases, final optimization results may show non-uniqueness from history matches. Non-uniqueness here means that there may be several relatively good history matches



achieved with different combinations of parameters. This outcome could be due to many parameters, insufficient amount of runs, or noisy datasets. In such cases, the resulting relative permeability and capillary pressure curves should be checked if they remain within a close range. Then, the results may be considered with a confidence interval as explained in the third method in Chapter 5.4.2. Known saturation endpoints, if interpreted from openhole logs, can further improve the results obtained in such cases.

It is observed from the examples that the curvatures and the relative permeability endpoints, DOI are sensitive to the parameterization, and the saturation endpoints are comparatively less sensitive (see Figures C.10 through C.16 in Appendix C.2). The damage skin is sensitive to bottomhole pressure only with the measured pumpout rate. Chapter 4.6 explains the effects of the reservoir and fluid properties for history matching in detail.

It is possible to include the saturation endpoints in the optimization; however, prior knowledge of the saturation endpoints may eliminate non-uniqueness and reduces forward run counts. For example, the non-uniqueness can be observed in Appendix B.3.2 where Figure B.61 shows acceptable history matches although the saturation endpoints change in a large range (Figure B.60). In the same example, the statistical evaluations assist to identify the best history match in Appendix B.3.3. Figures C.10 and C.11 in the field example in Appendix C.2 show that the history match results are insensitive to changes of the saturation endpoints. This is not a general conclusion for the saturation endpoints; however, if the insensitivity occurs, the saturation endpoints should be obtained from the openhole log interpretations.

Noisy observed datasets and many unknown parameters, for example more than 10 parameters, increase the chance of overfitting where statistical evaluations from multiple forward runs may suggest several good history matches over a large band of noisy observed datasets. In such a case, IPTT and openhole log interpretations become crucial and a hierarchical approach for the inversion, as explained earlier, is suggested. A parameterization model with fewer parameters, if it is appropriate, may be selected to reduce the unknown parameter counts.

The radius of influence of reservoir properties, such as flowing pressures, oil saturations, and horizontal and vertical oil velocities during the WFT cleanup varies depending on the formation properties, duration of the invasion and cleanup, and the WFT pumpout rate and the inlet type. The radius of influence of the flowing pressure is generally tens of feet, while the radius of influence of vertical and horizontal oil velocities is several feet into the reservoir (see Figure C.23 in Appendix C). The additional pressure drop due to the skin factor is effective in the near-wellbore region and in the invaded zone. The invasion profile dynamically changes due to capillary forces and gravitational slumping of the invasion fluid, and DOI may be up to couple of feet if the mud cake is properly established.

A combination of LHS and ES strategies are recommended to accelerate the parameter optimization process. If there is no limitation of computation capacity, the LHS strategy may provide better results since it screens the entire parameter ranges to assemble a plausible collection of parameter values and allows meaningful statistical analyses.

If DOI of the mud-filtrate and the saturation endpoints are obtained reasonably from openhole log interpretations, and the timeline of drilling and logging events are known, based on the complexity of the reservoir unit and available interpretations, such as IPTT, up to 10 parameters may be hierarchically obtained from fewer than 2000 forward runs, which may take 15 to 45 minutes each depending on the WFT inlet type used. Usually 64 to 128 concurrent numerical runs are common, the total forward runs may be completed in 10 to 24 hours. Generally fewer parameters are used, fewer forward model runs are expected. Additional parameters may require extra 50 to 200 SBO runs If DOI and saturation endpoints are not known prior to the study.

## **CHAPTER 6. CONCLUSIONS AND RECOMMENDATIONS FOR FUTURE RESEARCH**

### **6.1 Conclusions**

The study presented here shows that relative permeability and capillary pressure curves can be estimated concurrently from WFT cleanup datasets in a relatively short period of time. An inversion workflow based on the stochastic optimization is the chosen method for our study. The general workflow is validated by applications to synthetic examples with known solutions, which show that the correct relative permeability and capillary pressure curves can be recovered through the inversion of water-cut and pressure measurements. Although basics of hysteresis are explained, the study assumes that a single set of multiphase flow curves effectively represents the invasion and cleanup events.

Our study introduces the stochastic based optimization for the first time in the literature. The SBO method is appropriate due to advances of computer clusters and their computational cost. The method avoids local minima of the parameters and offers a statistical approach to the inversion problem. Additionally, the study develops statistical interpretation techniques for the SBO method, which is not readily available in detail in the literature.

Increasing the number of unknown parameters introduces the inherent problem of non-uniqueness on the resulting relative permeability and capillary pressure curves as explained previously. To avoid this problem, a hierarchical SBO approach is developed in which a prior interpretation of openhole logs and pressure transient data is used to limit the number of unknown parameters to be estimated simultaneously.

The study combines well operational schedules, such as the time of drilling, the duration of wiper trips, and the period of openhole logging. Reservoir and fluid properties are extensively investigated in numerical modeling in order to minimize modeling effects, and to mimic the well operational schedules. In the literature, the well operational schedules are rarely accounted for. This part is very essential to capture the near-wellbore invasion and cleanup dynamics, capillary pressure and gravitational slumping effects.

The complex mud-cake buildup behavior is ignored; instead, a model including dynamic and static filtrations is fully incorporated for the first time in the literature. The mud-filtrate invasion model, a part of the numerical simulation, accurately imitates the mud-filtrate invasion rates and the saturation changes near the wellbore. The realistic invasion model is necessary since time-lapse array resistivity logs are not common currently, and there is no methodology to provide saturation profiling within the invaded zone, and the invasion profile is not static and changes throughout logging periods near the wellbore. Although the mud-filtrate invasion can be optimized without prior knowledge, inputs from drilling reports and openhole logs can be included as well for the accuracy of the invasion volumes.

All commercially available WFT inlet geometries, such as SP, DP and 3DRP are fully integrated into the workflow. Numerical models for different WFT inlet types are developed with their wellbore sealing packers, properly defined tool storage volumes and fluid segregation effects. 2D gridding for the DP inlet and 3D gridding for the SP and 3DRP inlets are adopted due to their complexities and flow path requirements. The 3DRP inlet is introduced for the first time for this kind of study. The detailed DP inlet geometry and its interval fluid segregation is also not studied previously before our study. We believe these are important additions to the literature to properly model the fluid flow in the WFT tool as well as in the near wellbore region.

The parameterization of the damage skin is included in the inversion process, which is not exercised in the previous studies. It is established that the damage skin can be estimated satisfactorily from the inversion process. The damage skin is always inverted in the process since the pressure transient analysis may not solve all skin components correctly in a complex multiphase flow environment. Other components of the skin factor, such as the multiphase flow skin and the partial penetration skin naturally occur in the numerical model computations.

The use of IPTT analysis for horizontal and vertical permeabilities in the flow unit becomes crucial when there is no credible permeability measurements, such as core plugs, well testing, or frequent pretesting. The horizontal and vertical permeabilities obtained should be further distributed with other log trends to capture formation

heterogeneities. Our study shows that introducing the log distributed permeabilities improves the inversion results because of an improved representation of the formation.

The SBO method does not require prior knowledge of saturation endpoints or depth of mud-filtrate invasion from openhole log interpretations; however, we showed in several examples that their knowledge reduces the uncertainties of the interpretations. Although fluid viscosities can be inverted in the process, their prior knowledge is suggested to reduce the parameter count.

The proposed workflow provides an indirect measurement of multiphase flow properties, and it is not a substitute for core analyses. However, the radius of investigation in the field examples shows that WFT cleanup examines further than the invaded zone, and covers a larger scale beyond the size of a core plug (the standard size of a core plug analyzed in a laboratory is 40 mm by 25 mm (Shafer *et al.*, 2013)), and provides effective relative permeabilities and capillary pressures of the particular flow unit.

The study is performed with datasets acquired in an openhole where the mud cake is established and basic openhole logs and the following WFT cleanup are conducted. The study is controlled by the time-dependent invasion dynamics, and accurately measured or interpreted reservoir properties, and the properly modeled WFT cleanup. Screening of datasets are suggested before starting the study. For example, if openhole log interpretations show a very shallow mud-filtrate invasion, such as 1 to 3 in. The dataset should not be selected for the study. This is because the invaded zone generates the multiphase flow properties and the saturation endpoints may not be reached during the short cleanup in such shallow invasion profiles. Also formation heterogeneities should be included as precisely as possible. Ignored reservoir features, such as thin zones, high permeability streaks and conductive fractures may delay the hydrocarbon breakthrough unexpectedly in the model. Additional openhole logs can be run for the this purpose alone if required. In some occasions, transitional zones can complicate the estimation of the multiphase flow properties since the differentiation of mud-filtrate invasion and formation water, and the initial setup of the reservoir model may be challenging due to fluid distribution and capillary forces. The noise levels of WFT water-cut and pressure datasets should be investigated before committing for the study as well. However, there are numerous formations, whose earlier datasets are available and suitable for our study.

Besides basic openhole logs, the workflow requires only the data, which are commonly available from WFT sampling jobs, and it can be conducted in an almost fully automated manner within a short time period. We believe that the study demonstrates an accurate and fast complement to available techniques and a step forward in terms of making better use of already available WFT data.

## **6.2 Recommendations for Future Research**

Extension to relative permeability and capillary pressure along with properly accounting for possible hysteretic behavior during the invasion (imbibition) and cleanup (drainage) processes constitutes interesting directions for future research. The hysteretic approach can be investigated by a 2D array resistivity log inversion providing imbibition curves and WFT cleanup data focusing on drainage curves. In order to decouple the processes, it is also possible to acquire time-lapse openhole logs, for example, earlier LWD logs followed by wireline logs before (if possible also during) the WFT cleanup.

Deviated and horizontal wells should be included in a future study. Although the invasion and cleanup processes will be affected by formation bedding, well deviations and corresponding reservoir and fluid properties, the additional study does not require any advancement over our current study. The readily available methodology with a proper openhole log interpretation and a numerical grid due to deviation and bedding should resolve the challenge.

A joint study is suggested for combining ongoing research projects, such as the 2D inversion of array resistivity logging for the mud-filtrate invasion, and the gradient and the stochastic based optimizations in a common platform.

WFT relative permeability and capillary pressure curves should be compared with the core samples taken from the same reservoir interval. Fullbore or sidewall cores can be used for the study. We know that the depth of investigation of WFT dataset is more extensive than the core plug size due to expected WFT cleanup volumes. We believe that the two methodologies can complement each other, especially focusing on facies types, and scale versus heterogeneity in a flow unit.

Resistivity array tools may be developed to focus on saturation profiling of invaded zones in detail. WFT tools and resistivity logs should be combined to investigate the progression of saturation profiles before and after WFT cleanup events. These measurements can supply additional history matching datasets, and they can enhance the results obtained from the study. In theory, this is possible, but such combination logs are not preferred to run due to either operational reasons or different logging objectives.

Improvements of numerical simulators, such as additional multiplier developments, are suggested in order to use GBO options more efficiently. Endpoint scaling options in black-oil simulators should be improved such that several relative permeability and capillary pressure parameterization models can be implemented. Hysteresis applications, although they are used in black-oil simulators, should follow the same course of action if SBO and GBO methods should adopt them more often.